

STATE ESTIMATION IN COMPLEX BIOLOGICAL SYSTEMS

by

Ravikrishnan Perur Jayakumar

**A dissertation submitted to The Johns Hopkins University
in conformity with the requirements for the degree of
Doctor of Philosophy**

Baltimore, Maryland

October, 2019

© 2019 Ravikrishnan Perur Jayakumar

All rights reserved

Abstract

Estimation of system states in complex biological systems, a precursor to system identification, is complicated due to the high dimensionality of biological systems and the inherently stochastic nature of biological processes. This thesis presents state estimation for two model organisms, the weakly electric fish and the laboratory rat.

Weakly electric fish, *Eigenmannia virescens*: The study of animal behavior has been revolutionized by sophisticated methodologies that identify and track individuals in video recordings. Video recording of behavior, however, is challenging for many species and habitats including fish that live in turbid water. This thesis reports a methodology developed for identifying and localizing weakly electric fishes on the centimeter scale with subsecond temporal resolution based solely on the electric signals generated by each individual. These signals are recorded with a grid of electrodes and analyzed using a two part algorithm that identifies the signals from each individual fish and then estimates the position and orientation of each fish using Bayesian inference.

Laboratory rat, *Rattus norvegicus domestica*: Hippocampal place cells are spatially tuned neurons that serve as elements of a “cognitive map” in the mammalian brain. To encode the animal’s location, place cells are thought

to rely upon two interacting mechanisms: sensing the animal's position relative to familiar landmarks and calculating the distance and direction that the animal has traveled from previously occupied locations. The latter mechanism, known as path integration, requires a finely tuned gain factor that relates the animal's self movement to the updating of position on the internal cognitive map, with external landmarks necessary to correct positional error that accumulates. Path integration based models of hippocampal place cells and entorhinal grid cells treat the path integration gain as a constant, but behavioral evidence in humans suggests that the gain is modifiable. This thesis reports physiological evidence from hippocampal place cells that the path integration gain is indeed a highly plastic variable that can be altered by persistent conflict between self motion cues and feedback from external landmarks. In a novel, augmented reality system, visual landmarks were moved in proportion to the animal's movement on a circular track, creating continuous conflict with path integration. A decoding algorithm was developed to estimate the hippocampal path integrator gain. This algorithm is robust to temporal changes in neuronal firing characteristics and has the versatility to estimate the gain from both pyramidal cells and interneurons.

Primary Reader: Noah J. Cowan

Secondary Readers: James J. Knierim, Eric S. Fortune, and Chen Li

Thesis Committee

Primary Readers

Noah J Cowan (Primary Advisor)
Professor
Department of Mechanical Engineering
Johns Hopkins University School of Engineering

James J Knierim
Professor
Department of Neuroscience
Johns Hopkins University School of Medicine

Eric S. Fortune
Associate Professor
Department of Biological Sciences
New Jersey Institute of Technology

Chen Li
Assistant Professor
Department of Mechanical Engineering
Johns Hopkins University School of Engineering

Acknowledgments

First and foremost, I would like to thank my advisor, Dr. Noah Cowan. When I first joined his lab, I would have never thought that I would be where I am today and Noah, who has worn many hats as my teacher, mentor, colleague, and friend, has played a huge part in that. His brilliant and creative ways of thinking of solutions founded in the fundamentals has inspired me over the years. His door has always been open for whenever I've needed his mentorship and guidance. I thank him again for welcoming me into his lab all those years back.

I would like to thank Dr. James Knierim. Even though I wasn't officially his advisee, I've never had a situation that has made me stop and realize that. I've learned a lot from Jim over the years especially from his scientific rigor and the efficiency with which he's able to cut out the fluff and distill something down to its essence, be it discussing research or writing papers and grants. I thank him for allowing me to be a part of his lab and for his mentorship and support as I spent countless hours transforming from a through and through engineer to a budding neuroscientist.

The bulk of my thesis stems from a collaborative project between Noah and Jim. I would like to thank them both for creating an environment where it's

truly a joy to work on this project. They encouraged creative freedom but also taught me how to judge when to stop getting lost in the novelty of new ideas and to hunker down and get the science done for the ideas in hand. They've worked to make sure that the people on this project never felt like they were serving two people with diverging visions, but rather one scientific goal. I couldn't have asked for a better project to work on.

I thank Dr. Manu Madhav, for being my partner-in-crime in the work that contributed to this thesis and for 15 years of friendship and camaraderie. I've learned much from him personally and professionally over the years. Truly, no amount of words of gratitude will suffice.

I thank Dr. Eric Fortune, Dr. Francesco Savelli, and Dr. Sarah Stamper for their mentorship over the years that we've worked on together.

A special thanks to my dear friends, Alison Morrow, Erin Sutton, Alican Demir, Tammy Tran, and Vyash Puliyadi for inviting me to be a part of their lives over the years. They've truly made me feel at home away from home.

I thank the past and present members of the Locomotion in Mechanical and Biological Systems (LIMBS) laboratory and the Knierim laboratory with whom I've shared my time here at JHU. I treasure the not only helped me improve myself academically, but also has provided me with an amazing group of friends. I would like to thank lab members past and present.

I would also like to thank Dr. Iulian Iordachita and Dr. Dennice Gayme for providing opportunities and their support at a pivotal time that eventually led to me being able to join the graduate program.

This thesis would not have been possible without the guidance and support of this group of friends and colleagues. There are many others – graduate

students, staff, faculty and friends – with whom I've interacted and shared memories with over the years. They are too many to name but I would like to thank them for everything I've learned from them and for making my time at this esteemed institution one that I'll never forget.

Dedication

This thesis is dedicated to my parents, Chandrika and Madhavan Jayakumar, whose boundless love and unwavering support gave me solace and the strength to persevere on over all these years.

I would also like to dedicate this to my brother Unnikrishnan Jayakumar and family, my aunt and uncle, Lathika and Madhavan Sreekumar, my cousins (close enough to be brothers) Harikrishnan and Jayakrishnan Sreekumar for always being there to ease the hardships of the bad times and to celebrate the highs of the good.

Table of Contents

Abstract	ii
Committee	iv
Acknowledgments	v
Dedication	viii
Table of Contents	ix
List of Tables	xv
List of Figures	xvi
1 Thesis synopsis	1
1.1 High resolution behavioral tracking of electric fish, <i>Eigenmannia virescens</i>	2
1.1.1 The weakly electric fish, <i>Eigenmannia virescens</i>	2
1.1.2 Scientific question and approach	3

1.2	Investigation of the role of path integration in the hippocampal spatial map	4
1.2.1	Rat as a model organism for cognitive neuroscience	4
1.2.2	Cognitive map, place cells, and path integration	5
1.2.3	Question and approach	9

I *Eigenmannia virescens*

High resolution behavioral mapping of electric fishes in Amazonian habitats 14

2 Design and validation of electric fish tracking apparatus and algorithm 15

2.1	Methods	18
2.1.1	Electrode design	19
2.1.2	Oscillating dipole model	21
2.1.3	Step 1: Frequency localization of multiple oscillating signals	24
2.1.3.1	1(a): Detect harmonic signatures	24
2.1.3.2	Step 1(b): Cluster into candidates at each time window	27
2.1.3.3	Step 1(c): Associate candidate across time	28
2.1.4	Step 2: Spatial localization of a moving dipole source	29
2.1.4.1	Observations from grid electrodes	29

2.1.4.2	Particle filter approach	32
2.1.4.3	Specifics of filter implementation	33
2.1.5	Laboratory experiments	35
2.1.6	Estimation of electric fish dipole moment	37
2.2	Results	39
2.2.1	Validation of the spatial tracking algorithm	41
2.2.1.1	Laboratory trials.	41
2.2.1.2	Field trials.	47
2.2.2	Dipole moment strength comparison between epigean and hypogean subpopulations of fish.	49
2.3	Contributions	51
3	Discussion	52
II	<i>Rattus norvegicus domestica</i>	
	Investigation of the role of path integration in the hippocam- pal spatial map	60
4	Recalibration of path integration in hippocampal place cells	61
4.1	Results	64
4.2	Methods	73
4.2.1	Subjects	73
4.2.2	Dome apparatus	74

4.2.3	Training	77
4.2.4	Electrode implantation and adjustment	77
4.2.5	Neural recording	78
4.2.6	Experimental control	78
4.2.7	Experimental procedure	80
4.2.8	Experimental gain selection and gain ramp rates	81
4.2.9	Data analysis	82
4.2.10	Behavioral analysis	83
4.2.11	Estimation of hippocampal gain, H	84
4.2.12	Visualizing H	87
4.2.13	Coherence score	88
4.2.14	Landmark control ratio	88
4.2.15	Analysis of drift	88
4.2.16	Analysis of recalibration	89
4.2.17	Histology	89
4.2.18	Statistics	89
4.3	Extended data figures	91
4.4	Contributions	104
5	Further developments to spectral gain estimator	105
5.1	Improvements to the algorithm	106
5.1.1	Adaptive windowing	106

5.1.2	Enhancing gain estimation using place field detection .	108
5.2	New applications of the algorithm	111
5.2.1	Decoding on unsorted spikes	111
5.2.2	Online gain estimation from unsorted spikes	114
5.3	Contributions	118
6	Looking beyond place cells: investigation of the head direction cell network and potential role of gamma oscillations	120
6.1	Investigation of the head direction (HD) cell network	120
6.2	Potential role of gamma oscillations on the asymmetry of neural response to gain manipulation	128
6.3	Contributions	145
7	Discussion	146
7.1	Recalibration of path integration in hippocampal place cells .	146
7.2	Further developments to spectral gain estimator	149
7.2.1	Enhancing gain estimation using place field detection .	149
7.2.2	Decoding on unsorted spikes	150
7.2.3	Online gain estimation from unsorted spikes	151
7.3	Looking beyond place cells: investigation of the head direction cell network and potential role of gamma oscillations	153
7.3.1	Investigation of the head direction cell network	153

7.3.1.1	Possible mechanism for higher frequency of place field remapping in gain manipulation compared to gain of unity condition	156
7.3.2	Potential role of gamma oscillations on the asymmetry of neural response to gain manipulation	161
7.4	Conclusion	166
Appendix A Real time 6DoF pose estimation of animal's head for head direction cell analysis and enabling freely behaving animal		168
Appendix B Evolution of the hyperdrive design		171
Bibliography		176
Vitae		189

List of Tables

2.1	Root-mean-squared-errors (RMSE) of position and orientation estimates in the field. We performed four 100 s recordings in the field (TerraRonca_01 through TerraRonca_04), each of which had three fish restrained in tubes, and estimated their poses. The position RMSE which are not within the length of the tube (20 cm, \approx 1.5 fish body lengths) and angular RMSE which are not within 15° are shaded.	49
4.1	Results of behavioral analyses Two-sided Wilcoxon Signed Rank tests were performed on the differences between values in Epochs 3 and 1 and Epochs 4 and 3 with null hypothesis that the difference = 0. Pauses/lap (n = 37 sessions; p = 0.035); Inter-pause Interval (n = 37 sessions; p = 0.001); Inter-pause Distance (n = 37 sessions; p = 0.003). All other tests for Epochs 3-1 and Epochs 4-3 were not significant	103
6.1	Simultaneous place and head direction cell recalibration experiment: HD cell tuning width and recalibration gain.	127

List of Figures

2.1	Electrode design	19
2.2	Representation of spectrogram data and extracted frequency tracks.	25
2.3	Visual representation of frequency localization algorithm.	26
2.4	Dipole with two electrodes and ground.	29
2.5	The laboratory grid setup.	40
2.6	Results of tracking.	42
2.7	Shuffled error test of tracking.	43
2.8	Analysis of a sample dataset recorded using a grid of 8 electrodes was deployed at a field site in Brazil	48
2.9	Population distribution of fish dipole strengths at cave and surface sites	50
4.1	Dome apparatus, experimental procedure, and sample data.	66
4.2	Control of place fields by landmarks.	69
4.3	Recalibration of place fields by landmarks	72

4.4	Illustration of the steps of the spectral gain estimator. Actual data recorded in an experiment session was used for the generation of the figures.	85
4.5	Representative histology.	91
4.6	Examples of failure of landmark control.	92
4.7	Gain dynamics during each experiment.	93
4.8	Summary of dataset.	95
4.9	Slow drift of place fields against landmarks.	97
4.10	Dynamics of recalibration.	99
4.11	Path integration gain recalibration is also demonstrated by hippocampal interneurons.	101
4.12	Illustration of spectral decoding scheme.	102
5.1	Place field detection with multiple place fields and remapping	111
5.2	Unsorted decoding.	113
5.3	Online implementation of the spectral gain estimator	117
6.1	Preliminary data from simultaneously recorded place cells and head direction cells in a gain manipulation experiment.	122
6.2	Simultaneous place and head direction cell recalibration experiment: Place cell spike plot	125
6.3	Simultaneous place and head direction cell recalibration experiment: HD cell tuning.	126
6.4	Gain modulation of average theta precession of place cells. . .	128

6.5	Gain modulation of theta cycles skipped by spikes in place fields.	130
6.6	Gain modulation of inter-spike interval (ISI) histogram of place cells.	131
6.7	Gain modulation of theta oscillations in the local field potential (LFP)	133
6.8	Gain modulation of ISI versus theta phase within place fields.	134
6.9	Gain modulation of LFP power at slow and medium gamma.	137
6.10	Relationship between peak gamma frequency and velocity in lab and landmark frames.	139
6.11	Gain modulation of number of cells recruited in sharp-wave ripples (SWRs).	140
6.12	Examples of theta precession: stereotypical and during breakdown.	143
7.1	Open loop and closed loop optic flow experiment.	153
7.2	Simulation of remapping mechanism.	158
A.1	6DoF head tracking.	170
B.1	Unibody hyperdrive.	173

Chapter 1

Thesis synopsis

Biological data are seldom simple being the nonlinear superposition of the output of multiple complex nonlinear biological processes. Proper experiment apparatus and estimator design principles, guided by the scientific question at hand, help manage this complexity. This thesis consists of two studies exemplifying two types of studies on biological systems. Part I describes the design of an apparatus and estimator created with the purpose of studying unconstrained behavior of the weakly electric fish, *Eigenmannia virescens*, in its natural environment, the rivers of the Amazonian rainforest. Part II details the study of a much more controlled behavior, specifically the study of the path integration system in the hippocampal formation in the brain of a laboratory rat.

1.1 High resolution behavioral tracking of electric fish, *Eigenmannia virescens*

1.1.1 The weakly electric fish, *Eigenmannia virescens*

There are species of fish such as the sharks which can detect electric fields and are said to be electroreceptive. An electric fish is specifically one that is electrogenic, i.e it can generate electric fields (Nelson, 2011). Electric fish produce this electric field via a specialized structure called an electric organ, usually located in the tail of the fish. It is made up of muscle or nerve cells evolved to produce electric fields. The output of the organ is called the electric organ discharge (EOD). While some electric fish have EOD strengths of sufficient amplitude to stun prey, weakly electric fish generate an EOD that is too weak to stun prey. This EOD instead radiates out from the fish as its source and interacts with whatever might be present in the fish's immediate environment – plantlife, rocks, predators, prey, and other objects. Depending on these objects' relative impedance with respect to water, the electric field line density can change – lower impedance areas have a higher field density whereas higher impedance areas have lower field density. The local potentials of this modulated field are sensed by electroreceptors distributed over the surface of the fish's body, creating a two-dimensional projection, called the electric image, of the surrounding three-dimensional field. The fish is able to decipher this image to estimate the size, shape and distance of objects in range of their electric field. Given that these fish are also generally electroreceptive, this means that they can detect the electric field generated by their conspecifics allowing for a medium of social communication between conspecifics (Hopkins, 1974; S. A. Stamper

et al., 2012).

Weakly electric fish can be classified broadly by the spatiotemporal properties of their electric signal. Pulse-type fish emit discrete pulses followed by a silent period until the next pulse. In contrast, wave-type fish emit a continuously modulating periodic signal. Species differences can be reflected in frequency, harmonic content, and the spatial distribution of EOD. I will be focusing on wave-type fish, specifically *Eigenmannia virescens*. Their EOD frequencies span a wide range, from $\approx 200 - 600$ Hz and each individual's discharge frequency is subject to change in response to internal and external factors (Hopkins, 1974; Bullock, Hamstra, and Scheich, 1972).

1.1.2 Scientific question and approach

The study of animal behavior has been revolutionized by sophisticated methodologies that identify and track individuals in video recordings (Robie et al., 2017; Egnor and Branson, 2016). Video recording of behavior, however, is challenging for many species and habitats including fishes that live in turbid water. Analyzing the EODs of weakly electric fish obtained from recordings of natural populations is challenging. These groups of fish can contain more than 15 individuals and are often composed of multiple species within a single site (Tan et al., 2005a). Moreover, our field observations suggest that fish are commonly near conspecifics both in terms spatial position and EOD frequency, both of which can change rapidly. The recordings contain all fish EOD signals in addition to environmental noise and equipment artifacts. There is also limited visibility in the environment which complicates visual verification of

the fish positions at most recording sites.

In Part I, I present a method for identifying and localizing weakly electric fishes on the centimeter scale with subsecond temporal resolution based solely on the electric signals generated by each individual. These signals are recorded with a grid of electrodes and analyzed using a two-part algorithm that identifies the signals from each individual fish and then estimates the position and orientation of each fish using Bayesian inference. This also includes a method to use the estimates of the tracked frequency and spatial pose of the fish to backtrack its electric dipole moment strength. Because this system involves eavesdropping on electrocommunication signals, it permits monitoring of complex social and physical interactions in the wild. This approach has potential for largescale non-invasive monitoring of aquatic habitats in the Amazon basin and other tropical freshwater systems (Thomas, Floion, and Chretien, 1998; Geller, 1984).

1.2 Investigation of the role of path integration in the hippocampal spatial map

1.2.1 Rat as a model organism for cognitive neuroscience

For the study of cognition and memory, the laboratory rat (*Rattus norvegicus domestica*) is a useful model for multiple reasons. First, there are many similar neuroanatomical and functional structures in the rat and human brains, specifically in the hippocampus and related structures. The rat is also intelligent enough to perform fairly complicated and varied cognitive tasks, allowing for the design of a wide range of experiments. As a result, the physiological

systems involved in learning and memory have been extensively studied in this animal for many decades.

1.2.2 Cognitive map, place cells, and path integration

Cognitive map. The cognitive map is a mental representation which serves an individual to acquire, code, store, recall, and decode information about the relative locations and attributes of phenomena in their everyday spatial environment. The concept of a cognitive map derives from Kant's lectures and writings on geography (Richards, 1974). Kant believed that humans and animals have innate perceptual schemes for processing sensory information and that a geometrical-spatial framework is one of them. In Kant's words (Richards, 1974, page 7):

“Whoever wants to build a house, for example, first of all conceives of the whole from which all the parts will afterwards be derived. Therefore our present preparation is an idea [Idee] of knowledge of the world. We are creating indeed just such an architectonic concept [Begriff], which is a concept in which the manifold will be derived from the whole. Here the whole is the world, the stage on which we shall present all experience. Travels, and intercourse with people, broaden the extent of our knowledge. Each contact teaches us to know mankind but demands much time if this goal is to be reached. If we are already prepared by instruction we already have a whole, a framework of knowledge which teaches us to know mankind. Now we are in a position to classify each experience and to give it its place in this framework.”

Hippocampal formation and place cells. Extending this notion, Edward C. Tolman, in 1948, proposed that rats and other animals had cognitive maps

that permitted flexible and efficient navigation (Tolman, 1948). O'Keefe and Nadel, in the landmark book *The Hippocampus as a Cognitive Map* (1978) (O'Keefe and Nadel, 1978), proposed the hippocampus as the neural substrate of this cognitive map. Their work and many subsequent studies have shown additional evidence that supports this conclusion with the discovery of place cells, head direction cells, boundary cells, grid cells, time cells, and much more (O'Keefe and Nadel, 1978, Taube, Muller, and Ranck, 1990, Hafting et al., 2005, Manns, Howard, and Eichenbaum, 2007). A commonly held view was that the hippocampus receives spatial information from postrhinal cortex and the medial entorhinal cortex and non-spatial information from perirhinal cortex and lateral entorhinal cortex. By this viewpoint, the integration of this information in the hippocampus would make it a practical location for cognitive mapping, which would necessarily involve combining information about an objects' location and its other features. Recent studies have inspired a rethinking of this viewpoint with evidence pointing more towards a more mixed representation in these two pathways feeding into the hippocampus (Keene et al., 2016; Lisman, 2007; Knierim, Neunuebel, and Deshmukh, 2014; Furtak, Ahmed, and Burwell, 2012; Sereno and Lehky, 2011; Connor and Knierim, 2017). This makes the role of the hippocampus in the instantiation of the cognitive map much more nuanced and the story is likely to get more complicated over the coming years, befitting the complexity of neural connectivity.

The hippocampus is thought to play a crucial role in episodic memory by

binding the items and events of an experience within a spatiotemporal framework instantiated by place cells and grid cells (OKeefe and Nadel, 1978; Manns and Eichenbaum, 2006; Davachi, Mitchell, and Wagner, 2003; Suzuki, Miller, and Desimone, 1997; Knierim, I. Lee, and Hargreaves, 2006; Eichenbaum, Yonelinas, and Ranganath, 2007). These cells are influenced by both self-motion (idiothetic) signals and by external sensory landmarks. Self-motion signals provide the basis for a path integration computation, in which the hippocampal system tracks the animal's location by integrating its movement vector (speed and direction) over time to continuously update a position signal on the internal, cognitive map

Path integration. With knowledge of its initial position, path integration is the process by which an entity's movement signals are integrated over time to determine its current position. The degree/order of integration needed depends on the class of movement signal being integrated. For example, with knowledge of the initial position, to get the current position, a continuous velocity signal is to be integrated once and an acceleration signal twice.

For an entity, be it an animal or a robot, path integration is needed for the following processes essential to navigation:

- Mapping: Upon initial exposure to a new environment, an internal map needs to be generated for use in navigation, a process known as mapping. If all objects or landmarks of interest are within perceptual reach, there are methods, using a learned internal model of one's body, that enable determination of distances between them without locomotion. For example: distance estimation by stereovision works on this principle

— the difference in the image projected at the eyes by an object combined with the knowledge of the distance between the eyes can be used to estimate the spatial depth of the object. Similarly the difference between the amplitude and time-of-arrival of sound from a point source to a pair of ears combined with an estimate of the distance between the ears can be used to spatially localize the sound source in azimuth. However, a set of landmarks can be out of perceptual reach of another. In this case, as the entity explores the environment, path integration can be used to estimate and establish spatial relationships between landmarks. This map can be egocentric (i.e. where are the objects in the world with reference to the entity) or allocentric (i.e. where is the entity with reference to the world). The self motion signals can also be perceived in an egocentric or allocentric frame of reference.

- Localization: When an environment is familiar and an internal map is available, an entity is able to determine its location within this environment, a process known as localization, in ways similar to that discussed in mapping: the techniques usable when landmarks are within perceptual reach are still applicable. When landmarks are unavailable, path integration can be used in conjunction with the internal model to continue localization. However, given that measurement of motion signals are prone to noise in the real world, integration inevitably leads to accumulation of error which manifests itself as an estimate of one's location that is gradually drifting with respect to the actual location. The error can be corrected once the landmarks come back into perceptual reach.

1.2.3 Question and approach

There is strong evidence supporting the role of path integration inputs to place cells, grid cells, and head direction (HD) cells (Knierim, Kudrimoti, and McNaughton, 1998a; Hargreaves, Yoganarasimha, and Knierim, 2007; Save et al., 1998; Stackman, A. S. Clark, and Taube, 2002; Taube, Muller, and Ranck, 1990; Sargolini et al., 2006; Vanderwolf, 1969; McNaughton, Barnes, and O'Keefe, 1983; McNaughton, Barnes, Gerrard, et al., 1996; OKeefe and Nadel, 1978). For example, (a) the spatial firing of these cells can, under certain conditions, drift relative to all external landmarks, but they maintain an internal coherence relative to each other, suggesting an internally consistent map updated by self-motion cues (Knierim, Kudrimoti, and McNaughton, 1998a; Hargreaves, Yoganarasimha, and Knierim, 2007); (b) lesions to the vestibular system can cause dramatic loss of spatial/directional firing (Stackman, A. S. Clark, and Taube, 2002; Stackman and Taube, 1997); and (c) speed-, motion- and direction related information – predicted by path integration models and necessary components of the model's function - is prevalent throughout the system (Sargolini et al., 2006; Vanderwolf, 1969; McNaughton, Barnes, and O'Keefe, 1983; Kropff et al., 2015a). In the absence of stable, external landmarks, however, these spatial correlates of neuronal activity can quickly accumulate error and cause the internal representation of position or direction to drift relative to the external environment. Thus, it is crucial that endogenous spatial representations be anchored by stable, external sensory cues, such as individual landmarks and environmental boundaries. In support of the strong influence of such external cues, (a) rotation of both salient local and global landmarks

can cause the rotation of the firing fields of place cells, grid cells, and HD cells (O'Keefe and Nadel, 1978; Muller and Kubie, 1987; Hafting et al., 2005; Knierim, 2002; Knierim and Hamilton, 2011), (b) deforming the geometry of an environment reliably distorts the firing fields of place cells and grid cells (O'Keefe and Burgess, 1996; Barry et al., 2007; Krupic et al., 2015), (c) an encounter with a boundary can correct the error accumulated since the last boundary contact (Hardcastle, Ganguli, and Giocomo, 2015a); and (d) neural correlates of boundaries and discrete landmarks are found in the hippocampal formation (e.g., boundary/border cells, landmark vector cells (Savelli, Yoganarasimha, and Knierim, 2008; Solstad et al., 2008; Lever et al., 2009; Deshmukh and Knierim, 2013)). Vestibular signals, optic-flow, proprioception, and motor efference copy are idiothetic cues most often proposed to provide the self-motion signals that update hippocampal spatial representations in a continuous manner as the animal explores an environment.

Studying this interaction between path integration and landmark-based corrections requires three capabilities that are not possible using standard experimental manipulations: (a) to make flexible, controlled adjustments of landmark cues in real time; (b) to adjust self-motion inputs such as optic flow in a controlled manner that allows explicit control over the place fields by these cues, analogous to the control by external landmarks; and (c) to introduce errors between the landmarks and the path integrator under carefully controlled conditions to reveal the dynamics of the interaction, the constraints on the system, and the limits to which it can be pushed.

With this in mind, we have constructed an experimental system that allows

an unprecedented level of dynamic control of visual input to place cells and grid cells during naturalistic locomotion. We have created a novel augmented reality (AR) system that is quite different from (and complementary to) other virtual reality (VR) systems that have successfully investigated spatial cells of the hippocampal formation (Ravassard et al., 2013a; Saleem et al., 2013; Aronov and Tank, 2014; Aghajan et al., 2015; Chen, King, Burgess, and O'Keefe, 2013). In typical VR systems, the animal runs on a ball or treadmill and the visual landscape is updated as a function of the distance run. These systems demonstrate an impressive ability to drive the cells to fire in a spatially selective manner in virtual space, and they allow imaging and intracellular recording studies impossible with most freely moving animal studies. One major drawback, however, is that the vestibular input and the motor patterns that the animals learn to move the track ball can conflict with the animal's virtual locomotion, possibly explaining observed phenomenological anomalies such as the expansion of representations (Terrazas et al., 2005a; Aronov and Tank, 2014), or the conversion of place cell's response from encoding position to encoding distance (Ravassard et al., 2013a; Chen, King, Burgess, and O'Keefe, 2013). In our apparatus, the rat moves through real space, with normal vestibular, proprioceptive, and motor activity patterns, with real-time manipulation of visual inputs as a function of the rat's locomotion. The apparatus offers opportunities complementary to standard VR systems for the investigation of the interplay of landmark control and path integration of self-motion cues.

In Part II, I detail the experiments conducted using this augmented-reality

system where visual landmarks were moved in proportion to the movement of a rat on a circular track, creating continuous conflict with path integration. Physiological evidence from rat hippocampal place cells in these experiments show that the path-integration gain (the relationship between the displacement in the physical world to the update of position representation in the internal cognitive map) is a highly plastic variable that can be altered by persistent conflict between self-motion cues and feedback from external landmarks. Sustained exposure to cue conflict resulted in predictable and prolonged recalibration of the path-integration gain, as estimated from the place cells after the landmarks were turned off.

The estimation algorithm developed for this analysis was subsequently shown to be able to reliably estimate the gain from unsorted neural data. Unsorted gain decoding facilitated the development of an implementation that decodes the gain in real-time on incoming unsorted neural data, opening up previously infeasible experiments. The estimation algorithm itself was also significantly improved.

I conclude Part II of the thesis with preliminary results from ongoing research exploring two facets of the neural response to gain manipulation and path integration recalibration. (1) The first facet looks at the response of head direction cells to the same continuous conflict experiments. Head direction cells are a vital input to the hippocampal spatial map, feeding in information about the animal's allocentric head direction. The circular nature of the running trajectory of the animal means that the inputs have a significant directional component. (2) The second facet presents evidence of modulation

of the gamma oscillation component of the local field potential with gain manipulation. The CA1 region of the hippocampus is thought to be the hub of information transfer between the regions of the hippocampal formation and it is believed that this information transfer is mediated by gamma oscillations. The phenomenon of path integration recalibration, and in more general terms, the formation and maintenance of the hippocampal spatial map, is the result of the coordinated dynamics of multiple brain regions. Characterizing how the communication between these regions is affected by gain manipulation will be essential to understand the neurophysiological phenomenon observed in these experiments.

Part I

Eigenmannia virescens

High resolution behavioral mapping of electric fishes in Amazonian habitats

Chapter 2

Design and validation of electric fish tracking apparatus and algorithm

The text in this chapter is reproduced largely verbatim from Madhav et al., 2018 of which I was co-first author. The results of dipole strength estimation to a epigeal and hypogean population of fish was published as a part of E. Fortune et al., 2019. The associated text is my own.

The study of animal behavior often requires identification and localization, and characterization of individuals as they move through the environment. In the laboratory and in certain field conditions, this information can be extracted from video recordings of individual organisms during complex interactions (Robie et al., 2017; Egnor and Branson, 2016). Numerous methodologies have been developed that allow automated and semi-automated video tracking of individuals over a large range of spatial scales, ranging on the order of millimeters (e.g. *C. elegans*), to tens of meters (e.g. bats) (Cheng, Deng, and

Hedrick, 2011; Noldus, Spink, and Tegelenbosch, 2001; Chaumont et al., 2012; Kohlhoff et al., 2011; Branson et al., 2009; Dankert et al., 2009; Fontaine et al., 2009; Gomez-Marin et al., 2012; Kabra et al., 2013; Pérez-Escudero et al., 2014). Tracking over larger scales, e.g. kilometers, has been accomplished using devices attached to organisms (Weimerskirch et al., 2002; Tsoar et al., 2011; Tomkiewicz et al., 2010). There are, however, many species and environments in which these tracking techniques are infeasible, including certain aquatic environments and dense forests, as well as for species in which attaching tracking devices to each individual is not possible.

Many species that are difficult to track using video, however, may betray their locations via the production of signals, such as sound or electricity, that can be localized using computational techniques. Audio systems that monitor autogenous acoustic signals, such as whale songs or bat calls, using grids of microphones have been used to track some terrestrial and aquatic species (Ghose et al., 2001; Blumstein et al., 2011; Ali et al., 2009; Giraudet and Glotin, 2006; Watkins and Schevill, 1972).

We developed a sensor array and analytic tools for measuring the positions, electrical strengths and behaviors of weakly electric fishes. These fish species are widespread throughout the Amazon basin and in certain river systems in Africa. Measuring and monitoring the numbers of individuals, spatial movements and electric strength distributions, and social interactions of these fish will provide insights that can be used in the context of ecology and conservation of sensitive Amazonian habitats. These measurements are also critical for interpreting data from neurophysiological studies of electrosensory

control circuits in this important neuroethological model system (Heiligenberg, 1991; E. S. Fortune, 2006; Middleton et al., 2007; Chacron et al., 2003).

Weakly electric fish use a specialized electric organ to continuously produce electric fields that are detectable at distances of up to 2 m (Heiligenberg, 1991; Tan et al., 2005b). For many species (so-called wave-type fishes) this electric organ discharge (EOD) is pseudosinusoidal with fundamental frequencies that range from below 50 Hz to above 1500 Hz. These nocturnal fish commonly live in turbid water and in complex root and littoral habitats, where video tracking is generally not possible. We have developed a recording system and computational approach to track multiple wave-type electric fish that relies solely on their EOD signals. Using this system, we tracked *Eigenmannia virescens*, a species of Gymnotiform fish, in both laboratory and field settings. Our method is designed to make long-term behavioral recordings of these animals in the wild.

We capture the electric signals using a grid of amplified electrodes that are deployed in the fish's habitat. Our analytic approach is composed of two steps. In the first step, the algorithm identifies a set of signal features (e.g. frequency, harmonic amplitude ratio), that are unique to each individual fish. In the second step, the algorithm estimates the location of each fish by solving an inverse problem based on the sensor geometry and an electrostatic dipole model. In theory, each fish's location could be estimated analytically by inverting the signal propagation. However, even if the fish were a perfect dipole in an infinite placid lake, the transformation from fish position to the array of sensor measurements is highly nonlinear, rendering the inverse problem challenging.

Moreover, unpredictable sources of physical and biological variability (e.g. turbulent clouds of silt, fish and other objects through the grid, body bending) dynamically alter electric fields that add "noise". As a result, we believe the inverse problem is best addressed using statistical estimation techniques.

Our statistical approach is to estimate each fish's position and orientation using a particle filter. In a nutshell, the particle filter simulates thousands of signal sources (particles) in the environment, and compares the simulated readings at the sensors from these sources to the actual measured values. The particles with the closest readings to the actual measurements are assigned higher "weight", and the location estimate is the weighted mean of particle locations.

Once an estimate of the fish position has been obtained, the electric dipole strength of the fish can be subsequently estimated. This enables further richness of behavioral analysis enabling characterization of the relative strengths of the fish involved in a social behavior, with the best case scenario being the estimation of the age and sex of the individual.

2.1 Methods

Adult *Eigenmannia virescens* (10–15 cm in length, EODs between 346–452 Hz) were obtained from commercial vendors. The fish were housed in group aquarium tanks that had a water temperature of approximately 27°C and a conductivity in the range of 150 – 500 $\mu\text{S}/\text{cm}$ (Hitschfeld et al., 2009). All experimental procedures were approved by the Johns Hopkins Animal Care

and Use Committee and the Rutgers Institutional Animal Care and Use Committee, and followed guidelines established by the National Research Council and the Society for Neuroscience. Permits to conduct this research in Brazil were granted to Dr. Maria Elina Bichuette.

2.1.1 Electrode design

We designed and built custom amplifiers to record the specific electric signals produced by *Eigenmannia*. These fish produce an EOD in the frequency range 200 to 750 Hz with measured amplitude on the order of mV. Correspondingly, the amplifier circuitry (Fig. 2.1A) consists of a passive band-pass filter (≈ 25 – 20000 Hz) at the input, an instrumentation amplifier with a gain of ≈ 50 , and an op-amp buffer at the reference which acts as an high-pass filter (≈ 1.6 Hz) to mitigate the AC-coupling.

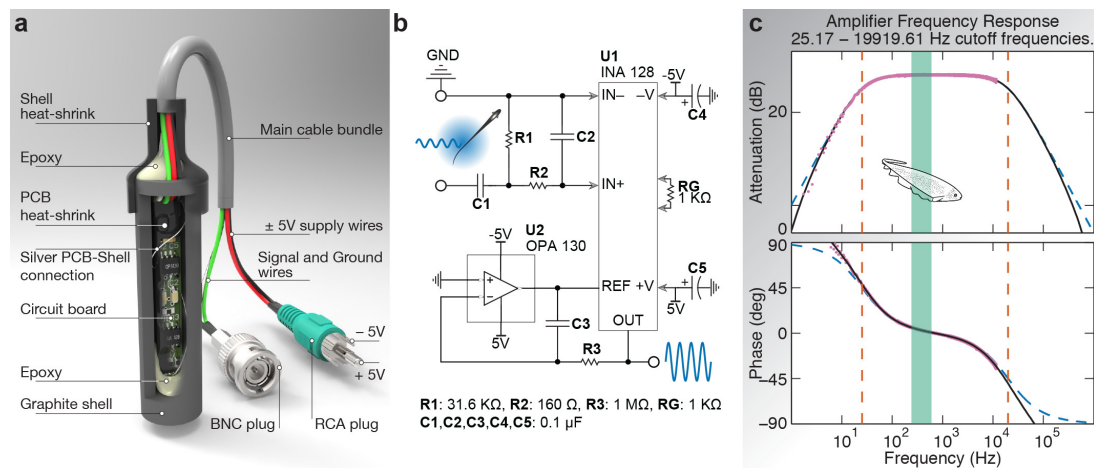


Figure 2.1: (a) Mechanical design of the electrode (b) Schematic of the individual amplifier with band-pass input. (c) Bode plot of the whole amplifier. The dashed blue lines represent the theoretical response given an ideal op-amp. The solid black line represents the theoretical response incorporating the manufacturer's models for both the instrumentation amplifier (INA128) and the reference buffer (OPA130). The magenta dots represent experimental data.

The input band-pass filter reduces low- and high-frequency noise signals that contaminate the fish's electric field signal. The filter cutoff frequencies (≈ 25 -20000 Hz) are chosen to be well outside of the *Eigenmannia virescens* frequency range so that relevant data are not affected.

The mechanical design of an electrode assembly is presented in Fig. 2.1a. We wrapped the amplifier circuitry in a heat-shrink tube and applied epoxy at both ends after placing it into a cylindrical graphite shell in order to waterproof it. Once submerged in the water, the graphite shell acts as the electrode and conducts the signal to the amplifier board via a 27-gauge silver wire. Power for the amplifier, ground, and the output signals are carried in a four-channel cable bundle whose length depends on the location of the electrode in the grid. Finally, the open cap of the graphite shell and the main cable interconnection is sealed with an outer heat-shrink tube. Standard BNC and RCA plugs are used to connect the amplifier to the data acquisition device and power supply respectively.

We tested our electrodes by recording their responses to a range of frequencies 0.5 Hz-15 KHz at 0.1 V. This was accomplished by generating frequency sweeps (chirps) from a function generator. We sampled both the input and output responses at 25 KHz using a data acquisition device. The theoretical cutoff frequencies of our band-pass filter are 25.2 Hz and 19.9 KHz. The theoretical frequency response curve is plotted in Fig. 2.1C, along with the matching response from the chirp test. The *Eigenmannia virescens* frequency range is depicted in the green shaded area where the attenuation is 0.50 (-6 dB) and phase is 2.4° .

Once electrodes were constructed, we assembled them into an array which could be easily deployed at field sites. Our field recording sites were shoreline edges, grass beds, and tree root systems that were reached by canoe. The grid array facilitated rapid assembly, transport, and deployment at these types of sites.

Electrodes were attached to a 1.5 m PVC grid with electrode spacing of 50 cm. Each electrode was held ~ 10 cm below the surface using a perpendicular PVC tube. The entire grid was suspended along the water surface using floatation fixtures in the corners and along the PVC piping. The electrode-amplifiers were powered by a common ± 1.5 V power supply and grounded via a carbon rod at least 1 m away from both the grid and from the water's edge.

Data were recorded with a Micro1401 DAQ with 12-channel expansion using Spike2 software (CED, Cambridge, U.K.).

For laboratory experiments a smaller 9 electrode grid (with the same electrode spacing) was constructed due to space constraints of the tank. All data recording methodology was identical.

2.1.2 Oscillating dipole model

To analyze the data obtained with the electrode grid, we need a model of the electric field generated by the fish. For our algorithms, we modeled *Eigenmannia* approximately as an oscillating current dipole. This is consistent with models constructed from spatial measurements of the electric field of *Eigenmannia* (Assad, Rasnow, P. Stoddard, et al., 1998; Assad, Rasnow, and

P. K. Stoddard, 1999). We made the following assumptions in approximating the fish to be a dipole:

1. *The dipole length is small relative to the grid spacing.* If a dipole is sufficiently close to an electrode such that $r \gg d$ does not hold true, we can safely assume that for a grid of electrodes with spacing larger than d , the dipole is sufficiently far away from almost all other electrodes such that $r \gg d$ holds true for them. We observed that with the number and spacing of electrodes present in our grid, a distortion on any one electrode has an insignificant influence on the spatial tracking error.
2. *The dipole is horizontal* We observed that *Eigenmannia* in laboratory tanks almost always oriented themselves horizontally, i.e. their anterior-posterior axis is held parallel to the water surface. We have also seen this anecdotally at our field sites. Thus, we specify the fish's spatial location using four coordinates: the spatial position and the orientation in the $x - y$ plane.

Consider an ideal current dipole, a source-sink pair of equal, but time-varying strength $I(t)$, separated by a small distance d at the origin, oriented along the x axis. Using the assumption that $r \gg d$, the potential due to this dipole at a point with polar co-ordinates (r, θ) in the plane defined by the dipole line and the point can be approximated by

$$\Phi = \frac{I(t) d \cos\theta}{4\pi\sigma r^2} = KI(t) \frac{\cos\theta}{r^2} \quad (2.1)$$

where σ is the conductivity of the medium. In *Eigenmannia*, we observed that

contributions to the electric field oscillation can be well approximated by the first two harmonics, i.e.

$$I(t) = A \cos(2\pi ft + \psi) + \gamma A \cos(4\pi ft + \xi) \quad (2.2)$$

where f is the fundamental frequency, A is the amplitude of the fundamental harmonic, γ is the ratio of the amplitude of the second harmonic to the fundamental, ψ is the phase of the fundamental, and ξ is the phase of the second harmonic. Equations (2.1) and (2.2) make the quasi-static assumption that, for a given time window, the location (r, θ) and frequency f of each dipole source is stationary.

Each fish, $j = 1, 2, \dots, n_{\text{fish}}$, induces a potential Φ_i^j at each electrode, $i = 1, 2, \dots, n_{\text{elec}}$. This potential can be calculated by replacing (r, θ) with the pairwise configuration of the j^{th} fish to the i^{th} electrode (r_i^j, θ_i^j) , as well as substituting fish-specific current waveform parameters $(A^j, \gamma^j, \psi^j, \xi^j, f^j)$. Thus, for a given time window, we have:

$$\begin{aligned} \Phi_i^j(t) &= K^j \frac{\cos \theta_i^j(t)}{r_i^j(t)^2} \left[A^j \cos(2\pi f^j t + \psi^j) + \gamma^j A^j \cos(4\pi f^j t + \xi^j) \right] \quad (2.3) \\ &= a_i^j \cos(2\pi f^j t + \psi^j) + \gamma^j a_i^j \cos(4\pi f^j t + \xi^j) \end{aligned}$$

The amplitude ratio γ^j is invariant for each dipole. The spatial location of dipole j with respect to electrode i is contained in the term a_i^j . The potentials from all the dipoles sum to form the total potential at electrode i :

$$\Phi_i(t) = \sum_{j=1}^{n_{\text{fish}}} \Phi_i^j(t). \quad (2.4)$$

If the different dipoles are oscillating at different frequencies f^j , these frequencies as well as their amplitudes at each electrode a_i^j can be estimated using Fourier analysis of the measured signals Φ_i . These amplitudes can then be analyzed over all the electrodes i to estimate spatial position at time t . By sliding the quasi-static time window, this analysis can be extended to the entire period of measurement.

Here we present a two-step algorithm to estimate the time-varying absolute position in three dimensions, $(x(t)^j, y(t)^j, z(t)^j)$, planar orientation, $\theta^j(t)$, and oscillation frequency, $f(t)^j$ of each of the dipole sources indexed by j , given the set of potential measurements, $\{\Phi_i(t)\}_{i=1}^{n_{\text{elec}}}$. Note that the electrodes are deployed at known locations on a rigid (PVC) grid. For example, see Fig. 2.5.

2.1.3 Step 1: Frequency localization of multiple oscillating signals

This step identifies the time-varying EOD signal parameters of each individual fish given measurements from a shoal of unknown size. The resultant “frequency tracks” represent the electric output of each individual (Fig. 2.2); together these tracks constitute the electrosocial milieu each animal experiences.

2.1.3.1 1(a): Detect harmonic signatures

For electrode i and for a window centered around time t , we compute the short-time Fourier transform (STFT) of $\Phi_i(t)$ using the `spectrogram()` function in Matlab. The result (Fig. 2.2) is a three-dimensional array of complex numbers, indexed across frequency, time, and electrode. At time t and for electrode i , we

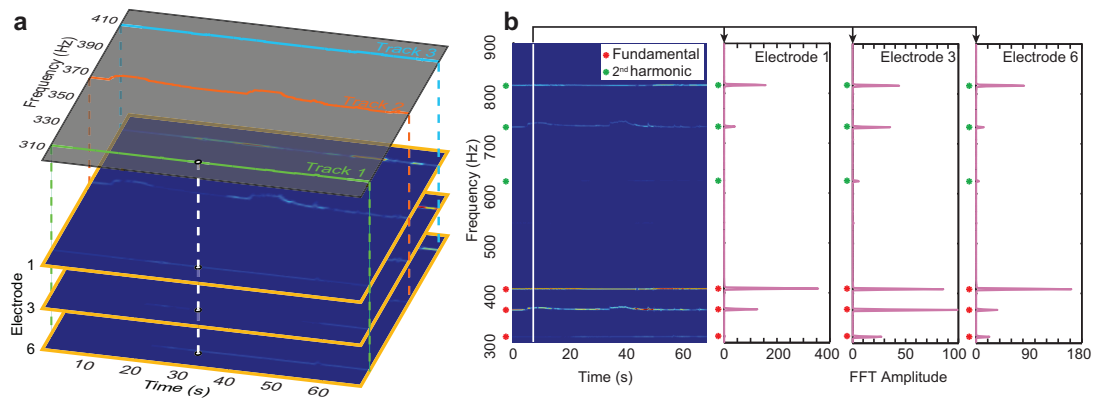


Figure 2.2: Representation of spectrogram data and extracted frequency tracks. (a) In the plots for each channel (electrode), the color denotes the amplitude of the signal at each frequency and at each time. This data over all channels is used to extract frequency "tracks", which are continuous traces of frequencies identified over time. Three tracks are extracted from this dataset. **(b)** Spectrogram amplitudes and harmonics. At each time instant (solid white line), the amplitudes from three representative electrodes are shown. In the presence of multiple frequency components with harmonics, these electrode amplitudes will typically show a peak at the fundamental frequency, and another (often smaller) peak at the second harmonic. In this data, fundamental peaks (red asterisks) and second harmonic peaks (green asterisks) from three fish are indicated in all three electrode amplitude traces. Higher harmonic peaks also exist, but are typically weaker and are not used in the analysis and therefore not shown.

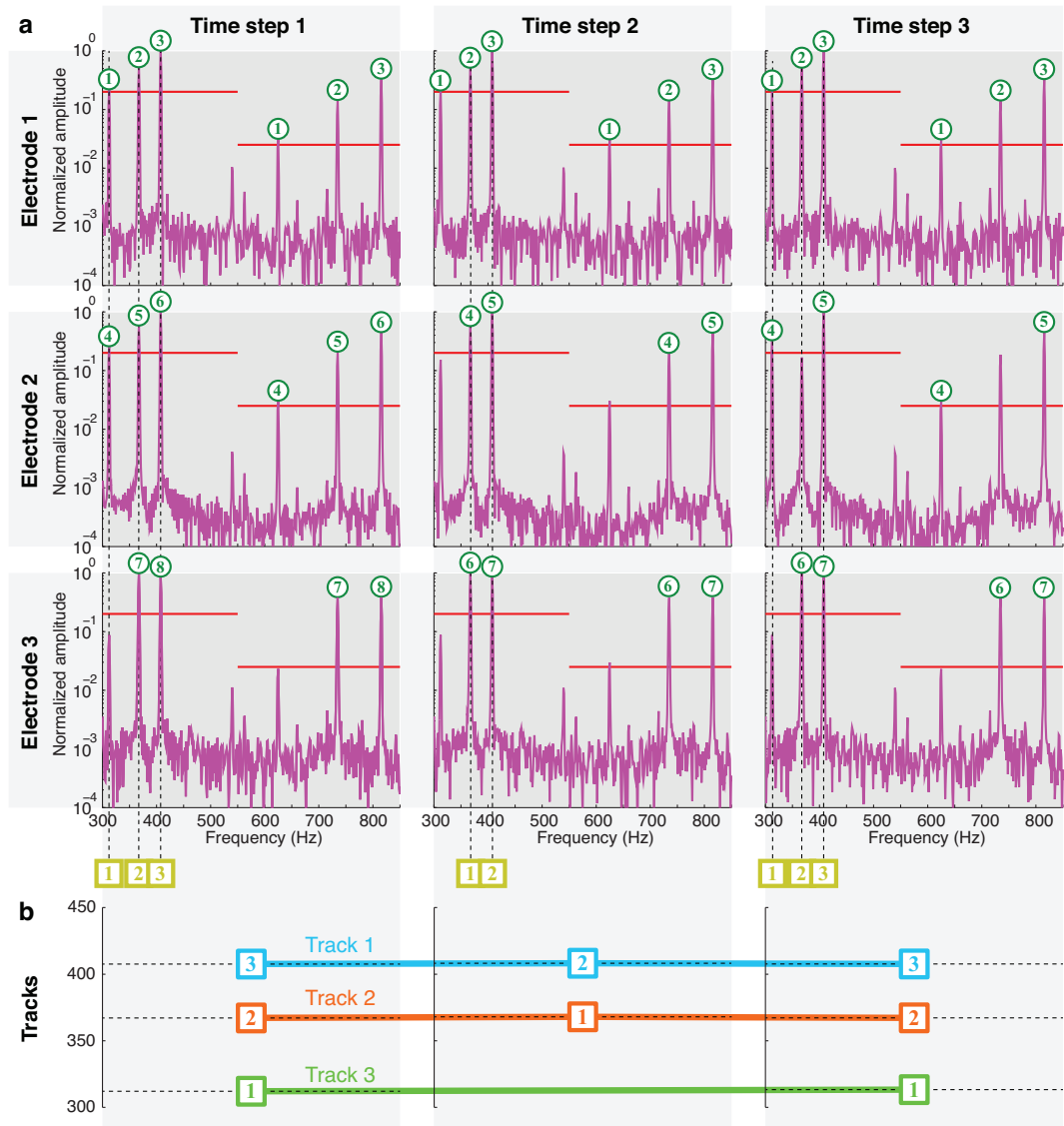


Figure 2.3: Visual representation of frequency localization algorithm. (a) The columns represent three contiguous time windows and the rows represent data measured at three electrodes. Each axis shows normalized (0—1) STFT magnitude vs. frequency (magenta traces). For simplicity, the algorithm is explained using three electrodes. At each time window, for each electrode, the signals whose fundamentals and first harmonics exceed the respective thresholds (red lines) are designated signatures (green circled numbers). At each time window, frequencies at which more than a certain number (in this example, 2) signatures are present, are grouped into candidates (yellow squared numbers). (b) Candidates are matched across time windows using the frequency and amplitudes of their fundamental to form tracks (colored lines). These steps are carried out across all time windows, and tracks are created or pruned using confidence criteria.

define a harmonic "signature" as a peak of the Fourier magnitude, which falls within a specified frequency range and above a specified threshold, τ_1 . Each signature should also have peaks at the second harmonic above a threshold, τ_2 . The ratio $\tau_2 : \tau_1$ is chosen heuristically based on typical amplitude ratios, γ^j , we have seen in laboratory experiments; see equation (2.3). For finding signals corresponding to the weakly electric fish *Eigenmannia*, we assume the fundamental frequency lies between 200—700 Hz and set the amplitude ratio to $\tau_2/\tau_1 = 1/8$. The threshold τ_1 was selected manually depending on the noise level of the data, and the strength of the fish EOD signal at the electrodes. For each signature, the fundamental frequency as well as amplitude and phases of the first two harmonics were recorded.

2.1.3.2 Step 1(b): Cluster into candidates at each time window

At each time window, several harmonic signatures may be identified at each electrode in the previous step. This step of the algorithm clusters the signatures by their fundamental frequency and forms "candidates"; each candidate comprises signatures with the same fundamental frequency, occurring at the same time instant at more than one electrode. Spurious signatures, e.g. due to local noise at an electrode, can be eliminated by this voting method. For tracking *Eigenmannia*, we assume that each candidate corresponds to the measured signal from an individual fish at multiple electrodes at the same time.

2.1.3.3 Step 1(c): Associate candidate across time

In the third and final step, candidates are associated across time to form 'tracks'. This association is made using the Hungarian algorithm, a combinatorial optimization algorithm that pairs measurements according to proximity under a distance metric (Kuhn, 1955). For our implementation, we used as our metric the Euclidean distance in the combined space of the candidates' fundamental and second harmonic amplitudes. Candidates in neighboring time instances are associated first. Because of possible frequency crossing and temporal gaps caused during spectral analysis, any remaining candidates two time intervals apart are associated next, and so on, up to a maximum gap of 5 s and a maximum difference in fundamental frequencies of 1 Hz. These thresholds in time and frequency were selected heuristically. The final tracks consist of continuous segments of frequencies, amplitudes, and phases of each putative fish.

We implemented the frequency tracking algorithm in MATLAB, with a GUI that displays the spectrogram from each electrode and the autonomously tracked frequency trajectories. The GUI allows manual edits to the frequency tracks: the user can split, join, or delete tracks. This, along with the ability to set the threshold τ_1 and the range of signature frequencies, provides user input and customization in frequency tracking, and makes sure that the tracked frequencies correspond to the patterns that humans can detect readily when visualizing the spectrogram amplitudes; see Fig. 2.2.

2.1.4 Step 2: Spatial localization of a moving dipole source

2.1.4.1 Observations from grid electrodes

The frequency localization algorithm outputs tracks, each of which represents the signal trajectory of a single dipole source. This allows each dipole to be spatially localized independent of other sources. In other words, we spatially track each fish separately, allowing us to omit the superscript j (putative fish number) in the derivations that follow.

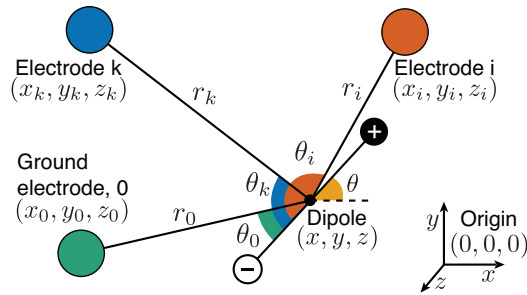


Figure 2.4: Dipole with two electrodes and ground. The dipole consists of two equal and opposite charges along an axis. The variables used in equations (2.18) and (2.21) are illustrated here. r_i , r_k and r_0 are the distances from the dipole axis midpoint, and θ_i , θ_k and θ_0 are the angles from the dipole axis, to electrodes a , b and g respectively.

Fig. 2.4 shows a dipole and three electrodes: i and k are grid electrodes, and 0 is the ground electrode with respect to which all electric potential measurements are made. The vector from the dipole center and each electrodes have lengths r_i , r_k and r_0 respectively, and the angles of these vectors from the dipole axis are θ_i , θ_k and θ_0 respectively. Note that the dipole and electrodes need not be coplanar; however, as stated earlier, the dipole and the electrode plane is assumed to be parallel.

We obtain amplitudes, phases, and frequencies of the fundamental and

second harmonic at each time window from the frequency localization algorithm. As per equation (2.3), the amplitude is a function of the polar position and orientation $(r(t), \theta(t))$ of the fish and other fish specific constants. The fundamental phase at an individual electrode by itself does not contain any spatial information as it can vary depending on the phase of the electric field oscillation at the start of the time window. However, if an electrode closer to the positive pole of the dipole has a phase value ψ , all other electrodes which are closer to the positive pole will have the same phase. The electrodes which are closer to the negative pole will have the opposite phase, i.e. $\psi \pm \pi$. This binary grouping of the electrodes results from the fact that the dipole midline splits the electrode plane into two. Thus, knowledge about this grouping yields information about the orientation of the dipole. In order to leverage this binary (signed) phase information, we define the signed potential amplitude at electrode i as:

$$\lambda_i = a_i \text{sign}(\cos \psi_i) \quad (2.5)$$

Using the grid, we can only measure the potential difference with respect to the ground electrode:

$$\lambda_{i,0} = \lambda_i - \lambda_0 = a_i \text{sign}(\cos \psi_i) - a_0 \text{sign}(\cos \psi_0) \quad (2.6)$$

The difference between the voltages at two electrodes i and k eliminates the effect of the unknown but constant location of the ground electrode:

$$\lambda_{i,k} = \lambda_{i,0} - \lambda_{k,0} = a_i \text{sign}(\cos \psi_i) - a_k \text{sign}(\cos \psi_k) \quad (2.7)$$

For n such electrodes, the voltage measured from the n^{th} electrode is subtracted from the other $(n - 1)$ electrodes and the resulting $(n - 1)$ vector is normalized to eliminate fish-specific constants:

$$\Lambda_{\text{ideal}}(t) = \frac{(\lambda_{1,n} \dots \lambda_{n-1,n})^T}{\|(\lambda_{1,n} \dots \lambda_{n-1,n})\|} = h(X(t)) \quad (2.8)$$

This *ideal observation vector* does not depend on the fish-specific constants K , A or γ , but is a function $h(\cdot)$ of the unknown *state* $X(t)$ of the dipole (see Fig. 2.4). This state vector comprises the position of the dipole source with respect to a fixed origin, and angle $\theta(t)$ of the dipole in the horizontal (x - y) plane:

$$X(t) = (x(t), y(t), z(t), \theta(t))^T. \quad (2.9)$$

We assume that the actual observations are contaminated with independent, zero-mean observation noise, v_{obs} :

$$\Lambda(t) = \Lambda_{\text{ideal}}(t) + v_{\text{obs}} = h(X(t)) + v_{\text{obs}} \quad (2.10)$$

If $f_{\text{obs}}(\cdot)$ is the probability density of v_{obs} , this also means that the likelihood of a particular observation given the state of the fish is

$$p(\Lambda(t)|X(t)) = f_{\text{obs}}(\Lambda(t) - h(X(t))). \quad (2.11)$$

Our goal is to find an estimate, $\hat{X}(t)$, for the 4-dimensional state of each dipole, given the $(n - 1)$ -dimensional measurement vector $\Lambda(t)$. Since the relationship between the state and the measurements is through a transcendental equation, this is a highly nonlinear problem, which typically has no closed-form inverse. Even if such an inverse exists, it is still necessary to

combine redundant noisy data. To do so, we resort to a particle filter, a statistical estimation technique analogous to other (approximate) Bayesian schemes such as extended or unscented Kalman filters. We chose to use the particle filter because of its ability to handle non-unimodal data.

2.1.4.2 Particle filter approach

A particle filter is a statistical estimation technique that can be applied to nonlinear problems with multimodal noise distributions. The state vector of the fish $X(t)$ evolves in time. We make observations $\Lambda(t)$ of the system, as described in the previous section. The particle filter uses a set of N particles $\{X_k(t)\}_{k=1}^N$, each of which has the same state variables as $X(t)$, in addition to a weight $w_k(t)$. Our current knowledge of $X(t)$ is the posterior distribution given all previous observations, $p(X(t)|\Lambda(1:t))$. The assumption is that, given large enough N , the set of particles and their respective weights approximates the posterior distribution. That is, each particle is a sample from this posterior distribution and its weight is the probability of drawing that sample.

At time t , we compute observation vectors for each of the particles:

$$\Lambda_k(t) = h(X_k(t)). \quad (2.12)$$

We also compute the actual observation vector $\Lambda(t)$ from the grid electrode data. From equation (2.11), the likelihood of observing the vector $\Lambda(t)$ given the current state of the particle $X_k(t)$ is computed as:

$$p(\Lambda(t)|X_k(t)) = f_{obs}(\Lambda(t) - h(X_k(t))). \quad (2.13)$$

We assume f_{obs} to be a zero-mean normal whose covariance grid is σ_{obs}^2 times an $(n - 1) \times (n - 1)$ identity grid. The variance σ_{obs}^2 was selected heuristically to give good tracking performance in preliminary lab data.

This likelihood is used to update and re-normalize the weights of the particles from the previous time step:

$$w_k(t) \leftarrow w_k(t - 1)p(\Lambda(t)|X_k(t)),$$

$$w_k(t) \leftarrow \frac{w_k(t)}{\sum_{k=1}^N w_k(t)}.$$
(2.14)

The state estimate at time t , $\hat{X}(t)$, is the weighted mean of the particles:

$$\hat{X}(t) = \sum_{k=1}^N w_k(t)X_k(t).$$
(2.15)

The particles at time t evolve via a simple random motion model:

$$X_k(t + 1) = X_k(t) + v_{mot},$$
(2.16)

where v_{mot} is drawn from a 4-dimensional normal distribution with zero mean and variances which were tuned heuristically to ensure good tracking performance in laboratory data. We found that the results were not sensitive to this value, and we were able to change v_{mot} by an order of magnitude without substantive change to tracking performance.

2.1.4.3 Specifics of filter implementation

We implemented the particle filter algorithm as described in Arulampalam et al. (Arulampalam et al., 2002), with the parameters and modifications as described below.

We used $N = 2.5 \times 10^5$ particles. At the first time step, the initial states of the particles were sampled from a non-informative (uniform) prior distribution in the state space. The weights of the particles, w_k , are set to $\frac{1}{N}$ at the first time step. To achieve reasonable particle density, we constrained the state space. For x and y , the limits are the tank boundaries in lab data, and twice the dimensions of the grid for field data. The z state can take values between 0 – 3 meters from the plane of the grid of electrodes for both the lab data and field data. Note that this restriction in state is relaxed for subsequent time steps: particles are permitted to cross the constrain threshold if that is what the motion model dictates.

One common problem that arises during particle filter implementation is sample impoverishment, where most particles end up having (near) zero weights after a few iterations. In order to counter this, we compute the effective number of particles (Arulampalam et al., 2002):

$$N_{\text{eff}} = \frac{1}{\sum_{k=1}^N w_k(t)^2} \quad (2.17)$$

When N_{eff} falls below a threshold, which we set to $\frac{N}{2}$, we trigger a resampling operation. 50% of the particles are resampled from the existing distribution, as represented by the particles and their weights. 45% of the particles are "locally sampled", i.e. they are normally distributed around the current estimate, $\hat{X}(t)$. 5% of the particles are "globally sampled" from the same non-informative uniform prior distribution in the state space used at the first time step.

During tracking, the particles often converge to a small region of state space

around the fish as desired, and consequently, the density of particles becomes sparse in most of the state space. *Eigenmannia* sometimes perform rapid “darting” movements, swimming to high velocities with high acceleration for a short period of time. Such movements are not readily captured by the motion model which is tuned to capture smooth, not ballistic, motion. If the fish moves rapidly in this way into a region where there are few particles, the distribution of particles will not keep pace, and the estimate will diverge. The obvious way to counter this would be to obtain spatial estimates at a temporal rate fast enough to capture these darting movements. However, the hardware EOD sampling rate, combined with the length of the time window needed to encompass sufficient number of cycles of the EOD for obtaining a discernible spectrum, limits the temporal rate of frequency and spatial tracking. Instead, we deploy the locally and globally sampled particles to maintain a sufficient particle density in the state space to capture these quick movements.

2.1.5 Laboratory experiments

In order to validate our tracking algorithm, we performed experiments of fish swimming in a large laboratory tank. We used a 3×3 electrode grid with an inter-electrode spacing of 30 cm in an acrylic tank of dimensions 1.5 m \times 1.2 m \times 0.3 m (Fig.2.5). The tank was filled to a depth of 28 cm with water, whose conductivity was maintained between 100—250 $\mu\text{S}/\text{cm}$. The PVC support of the grid was at the water surface, and the electrodes were lowered to a depth of ~ 10 cm below the surface. Fish were released into the tank and acclimatized for several hours prior to recording data.

A camera (Logitech C920) with a ring illuminator captured an overhead view of the tank at 30 frames per second. Retroreflective markers were placed on the top surfaces of the electrodes as well as the four corners of the tank. These markers were isolated and identified post-hoc through image processing to detect the position and orientation of the tank and electrodes in the camera frame. Electric potential measurements from the electrodes were digitized at 20 kHz. and recorded using a Spike2 data acquisition device (CED, Cambridge, U.K.). The acquisition device also triggered a blinking LED in the field of view of the camera, the timing of which was used to synchronize between the electrode recordings and camera frames. We performed two types of laboratory experiments: TUBE and FREE.

In the TUBE condition, each fish was confined to a tube of length 20 cm with plastic mesh sides and ends. The tubes were placed horizontally at a depth of 10–15 cm at different locations and orientations relative to the electrode grid. Two retroreflective markers were placed on either end of each tube, which enabled us to track the position and orientation of the tubes in the camera frame. We performed 15 trials with a single fish in a tube, with the tube at different positions and orientations across the tank both within the grid perimeter and outside the grid. We also performed 40 trials with three fish in three separate tubes (e.g. Fig. 2.6(a)), arranged from being immediately adjacent to each other to being across the tank from each other, across a variety of relative orientations. The position and orientation of the tubes tracked from a single frame of the overhead video is considered the *video-tracked pose*, and the mean of the estimates from our algorithm is considered the *electrode-tracked*

pose. (See supplementary figures for more examples. All TUBE data are made available as part of this publication.)

In the FREE condition, fish were released into the tank and allowed to swim freely. When the lights were on, fish preferred to remain at the edge of the tank, outside the grid. To maintain movement, the experimenter used a clear acrylic rod to induce the fish to swim. For our analysis, we chose epochs where the fish were moving for a majority of the epoch. We performed trials with a single fish in the tank (e.g. Fig. 2.6 (b)), and with groups of three fishes. The head and tail of each fish were manually clicked every 10th video frame. The clicked points are used to compute the position and orientation of the fish, and form the *video-tracked poses*. The estimates from our algorithm at the same time instances as the clicked video frames are the *electrode-tracked poses*. (See supplementary videos for more examples. All FREE data are made available as part of this publication.)

2.1.6 Estimation of electric fish dipole moment

For a single fish, the frequency tracking algorithm takes the spectrogram of the oscillating potential signal, tracks the fundamental frequency and outputs its amplitude, $\phi(t)$ at each electrode i with respect to the ground electrode 0 at each time window.

$$\phi_{i,0} = \phi_i - \phi_0 \tag{2.18}$$

where

$$\begin{aligned}\phi_i &= \frac{A d \cos\theta_i}{4\pi\sigma r_i^2} \\ &= \frac{p \cos\theta_i}{4\pi\sigma r_i^2}\end{aligned}\tag{2.19}$$

where $p = Ad$ is the time-invariant dipole moment of the fish. The location of the ground electrode with respect to the dipole is unknown. Taking the difference between the voltages at any two electrodes 1 and 2 eliminates the effect of the unknown potential ϕ^0 of the ground electrode:

$$\begin{aligned}\phi_{1,2} &= \phi_{1,0} - \phi_{2,0} \\ &= \frac{p \cos\theta_1}{4\pi\sigma r_1^2} - \frac{p \cos\theta_2}{4\pi\sigma r_2^2} \\ &= \frac{p}{4\pi\sigma} \left(\frac{\cos\theta_1}{r_1^2} - \frac{\cos\theta_2}{r_2^2} \right)\end{aligned}\tag{2.20}$$

Rearranging to get an expression for the dipole moment p , we get

$$p = \frac{4\pi\sigma\phi_{1,2}}{\left(\frac{\cos\theta_1}{r_1^2} - \frac{\cos\theta_2}{r_2^2} \right)}\tag{2.21}$$

Therefore, at each time window, for n electrodes, we get $\binom{n}{2}$ estimates of the dipole moment. The dipole moment estimate for that time window is the median of these estimates. To calculate the estimated dipole moment of an individual fish, a subset of the time windows are selected in which the area of the convex hull (outer bounds) of 90% of the highest-weight particles (from the particle filter used in the spatial tracking algorithm) is less than 0.16 sq.m.

This is a proxy for the spread of the particles which represents the uncertainty of the estimate. The dipole moment of the fish is estimated as the median of dipole moment estimates across the selected subset of time windows.

2.2 Results

We validated the approach, which relies on recordings made with an electrode grid system (Fig. 2.5) and a two-step algorithm to extract the identities and positions of individuals in a laboratory tank in which the positions of the fish were also tracked via video recordings. We subsequently validated the system at a field site in Brazil, in which fish were restrained in mesh tubes at known locations within the grid.

The tracking system involves three steps: (1) capturing the data using an array of electrodes placed in the habitat of the animals, (2) extracting the parameters of the electric signals (e.g. fundamental frequencies and harmonics) of each individual fish, and (3) tracking the spatial position and orientation (pose) of each fish with respect to the grid geometry.

The frequency tracking algorithm is semi-automated. The computer extracts potential frequency tracks produced by individual fish by identifying peaks in amplitudes of Fourier transforms of the electrode data. These frequency tracks are then superimposed on the spectrogram of the recorded data. The user then selects those tracks that match the frequency bands in the spectrogram - each band corresponds to the EOD of an individual fish.

Frequency tracking of signals recorded in the laboratory required little human intervention, because of the high signal-to-noise ratio, and due to the

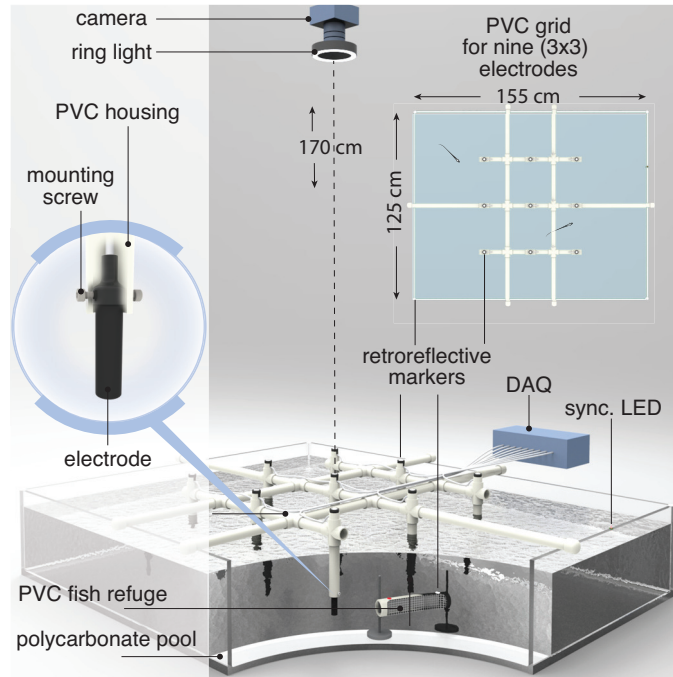


Figure 2.5: The laboratory grid setup. A 3×3 grid of electrodes (50 cm inter-electrode spacing) are mounted to a PVC support structure, and mounted to the edges of an acrylic tank. In the TUBE condition, fish are enclosed in tubular refuges and placed near the bottom of the tank. In the FREE condition, fish can swim freely throughout the tank. A ring light around the camera mounted above the tank illuminates retroreflective markers on the electrodes. The electrical signals are captured and subsequently recorded by the DAQ.

reduced electrosocial behaviors that *Eigenmannia* and other species exhibit in large laboratory tanks. *Eigenmannia* maintained almost constant EOD frequencies that were typically separated by more than 5 Hz from other fish in the tank.

In contrast, we observed more complex electrosocial behaviors and increased interference, including 60-cycle noise, at our field sites. Fish routinely changed their frequencies over a range of more than 20 Hz, and routinely crossed or shared EOD frequencies for periods of up to tens of seconds. The algorithm is robust to such crossings, and the interface allows the user to

reassign frequency tracks as needed. For fish that shared the same frequency for 10s of seconds, we were able to use both small independent deviations in EOD frequencies of each fish and differences in amplitude across the electrode array to identify individuals.

The output of the frequency tracking algorithm was manually checked against the raw spectrogram for both lab and field data and corrections, if needed, were made via the GUI. We extensively and explicitly validate the spatial tracking in the next section, which also implicitly validates the frequency tracking.

2.2.1 Validation of the spatial tracking algorithm

The second component of the algorithm, spatial tracking, is fully automated. We validated the pose of each fish estimated by the tracking algorithm by comparing against the pose measured through image processing of overhead video. We performed two types of experiments in the acrylic laboratory tank. In TUBE trials, one or three fish were enclosed in PVC tubes which were stationary during the course of one trial. In FREE trials, one or three fish swam freely in the tank, and we chose epochs where one or more fish were swimming through the grid. A detailed description of the experimental setup and data collection is provided in the methods section.

2.2.1.1 Laboratory trials.

When the output of the tracking algorithm, i.e. the electrode-tracked pose was compared to the camera-tracked pose, we observed that the estimate of fish

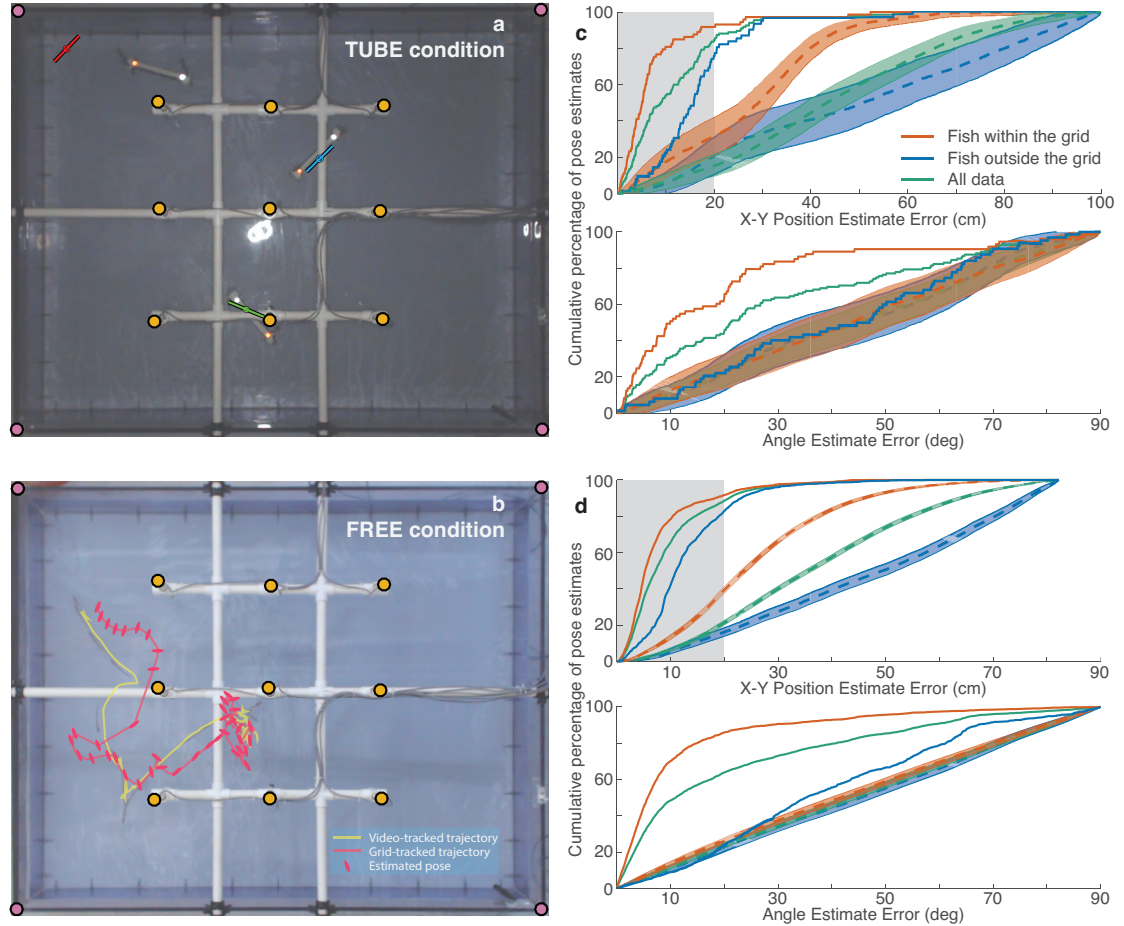


Figure 2.6: Results of tracking. (a) Overhead view of one three-fish TUBE trial. The mean position from tracking is shown using the circle markers with orientation indicated by the lines. The radius of the circle corresponds to two standard deviations of the X-Y position estimate. (b) Overhead view of one single-fish FREE trial, constructed by superimposing multiple keyframes from the video. Trajectory of the fish tracked from the video along with the trajectory and orientations of the fish estimated by the electric tracking system. (c) Cumulative error plots (solid curves) of position (top) and angle (bottom) for all TUBE trials. For position plots, the length of the tube (20 cm, ≈ 1.5 fish body lengths) is shaded in grey. Errors are divided into instances when the fish was within the grid, outside the grid, and all data taken together. The dashed curves show the mean of the shuffled cumulative error distributions and the shaded areas indicate the the 0.001 and 0.999 quantiles of the shuffled data, equivalent to 99.8% CI (see Statistical Methods) (d) The same curves for FREE trials.

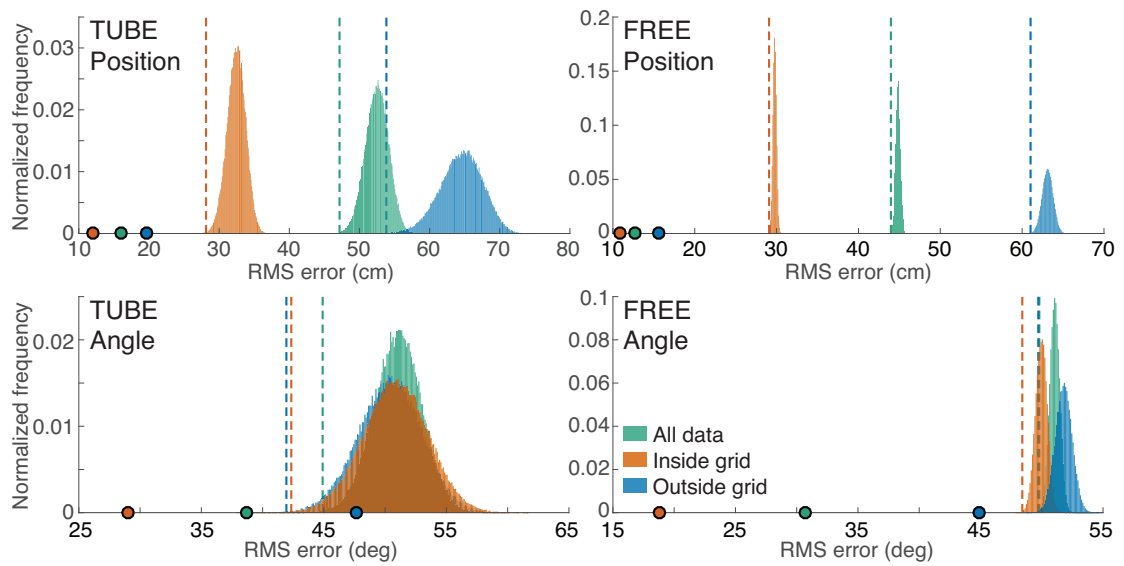


Figure 2.7: Shuffled error test of spatial tracking. Position (top) and Orientation (bottom) errors are shown for TUBE (left) and FREE (right). The normalized histograms of the shuffled RMS error distributions (see Statistical Methods) of all data are shown, as well as the subsets of data within and outside the grid. The dotted vertical lines indicate the 0.001 quantile lines (equivalent to 99% CI) of the distributions of the corresponding colors. The points on the x-axis represent the RMS errors of the true (unshuffled) data of the corresponding colors.

pose deteriorated (i.e. the error increased) when the fish were close to the tank boundary. We attribute this to the insulating acrylic walls of the tank, which distort the signals from any sources close to it. Because of these boundary effects, we partitioned the data into two sections based on the actual position of the fish: within the grid and outside the grid. Fish are considered to be within the grid if their video-tracked position is within the square defined by the outermost electrodes.

In the TUBE condition, for fish within the grid, a majority of positions and orientations estimated by our method fall remarkably close to the actual pose of the fish. Specifically, within the grid, more than 90% of the tracked positions were within 20 cm (\approx length of the tube, \approx 1.5 fish body lengths) of the video-tracked positions. More than 80% of the tracked orientations were within 30° of the video-tracked orientations (Fig. 2.6(c)). Data within the grid have better (lower) cumulative error curves than data outside the grid, and the combined data have a cumulative error curve in between the two.

In the FREE condition, the tracking error is nearly identical to that seen for the restrained fish; more than 90% of the position errors were within 20 cm and more than 90% of the tracked orientations were within 30° of the video-tracked orientations (Fig. 2.6(d)). The cumulative error curves also have the same performance relationships.

We compared the tracking errors to two different test statistics on a dataset where the video-tracked poses were randomly shuffled against the electrode-tracked poses (see Statistical methods for details).

We used a shuffling (Monte-Carlo permutation) procedure in order to

analyze the performance of our tracking algorithm. For the TUBE and FREE trial types, we compiled all pairs of poses (X-Y positions and orientations) of all fish tracked through overhead video and our electrode-based tracking method. Each pose pair consisted of one video-tracked pose of one fish for one frame of the overhead video, and its corresponding electrode-tracked pose. There were 135 pose pairs for the TUBE dataset (using a single video frame per trial for each fish) and 3222 pose pairs for the FREE dataset (using every tenth video frame from each trial for each fish). In each shuffling iteration, the video-tracked poses were randomly permuted, and position and orientation errors to their corresponding electrode-tracked poses were computed. These iterations were repeated 100,000 times. The set of cumulative errors from the iterations form the *shuffled cumulative error distribution*. The set of root-mean-square (RMS) errors from each iteration form the *shuffled RMS error distribution*. The data were also divided into instances where the video-tracked positions are within the grid (TUBE: 73, FREE: 2081) or outside the grid (TUBE: 62, FREE: 1141). The shuffling procedure was also repeated for these subsets, creating three cumulative error and three RMS error distributions.

We compared the true (non-shuffled) cumulative error to the shuffled cumulative error distribution (Fig. 2.6 c,d). We also compared the true (non-shuffled) RMS error to the shuffled RMS error distribution (Fig. 2.7). This was to test the null hypothesis that the tracking error of the actual data was statistically no different from a random permutation of the locations of the fish.

The shuffled cumulative error distributions for data within the grid, data

outside the grid, and all data, along with their 0.1% and 99.9% quantiles are plotted in Fig. 2.6(c) and (d). The shuffled distributions appear to have the same relative relationships as the true error curves. The cumulative error curves of the true data are lower than the shuffled distributions in all cases except the orientation error for data outside the grid. This indicates that our algorithm cannot determine orientation of the fish accurately when the fish are restrained outside the grid boundaries. This is in fact confirmed and quantified by the second statistic, the root-mean-square (RMS) error between the set of video-tracked and electrode-tracked position and orientation estimates. Fig. 2.7 plots the shuffled RMS error distributions for positions and orientations in the TUBE and FREE conditions, along with their 0.1% quantile, and the RMS errors of the true data. In all cases except TUBE orientation outside the grid, the true data have significantly lower RMS errors than the distributions. For these cases, we can reject the null hypothesis that the tracking error of the actual data was statistically no different from a random permutation of the locations of the fish. However, in most cases, especially when the fish are freely swimming and within the grid, our algorithm performs orders of magnitude better than chance.

2.2.1.2 Field trials.

An 8-electrode grid with a 50 cm.inter-electrode spacing was deployed in the Lapa river within 200 m of the entrance of the Terra Ronca I cave ($13^{\circ}44'06.8''S$ $46^{\circ}21'29.3''W$, Goiás, Brazil). A characteristic of this field site was crystal-clear water, which allowed us to video the grid from above and under the water. The depth of the water under the grid ranged from 5 cm to 40 cm. The conductivity of the water has been reported to range between 15 and 34 $\mu S/cm$ (Bichuette and Trajano, 2015). We performed four 100s recordings from the field site (Fig. 2.8). In each recording, three fish with known EOD frequencies were restrained in tubes at known locations and orientations within the grid. However, other *Eigenmannia* freely swam in and around the grid. Interestingly, the fish in tubes maintained nearly constant EOD frequencies, whereas the free fish produced complex excursions in EOD frequency (Fig. 2.8).

We spatially tracked fish in the wild using the same parameters as those used for tracking fish in the lab. A site photo with overlaid spatial estimates is shown in Fig. 2.8. The spatial estimates varied over the 100 s long trials and we characterized the distribution of the estimates across time. The distribution of each fish's estimate for each data set was non-normal (Royston's Multivariate Normality Test, 5% significance level). To quantify the error in the estimate over time, we computed the root-mean-squared-error (RMSE) for each fish in each dataset (see Table 2.1). Errors were typically within 1.5 body lengths (10/12 estimates) and 15° (8/12 estimates), and never worse than 3 body lengths. As with the tracking in the lab, the positions and orientations estimated by our method fall close to the actual pose of the fish.

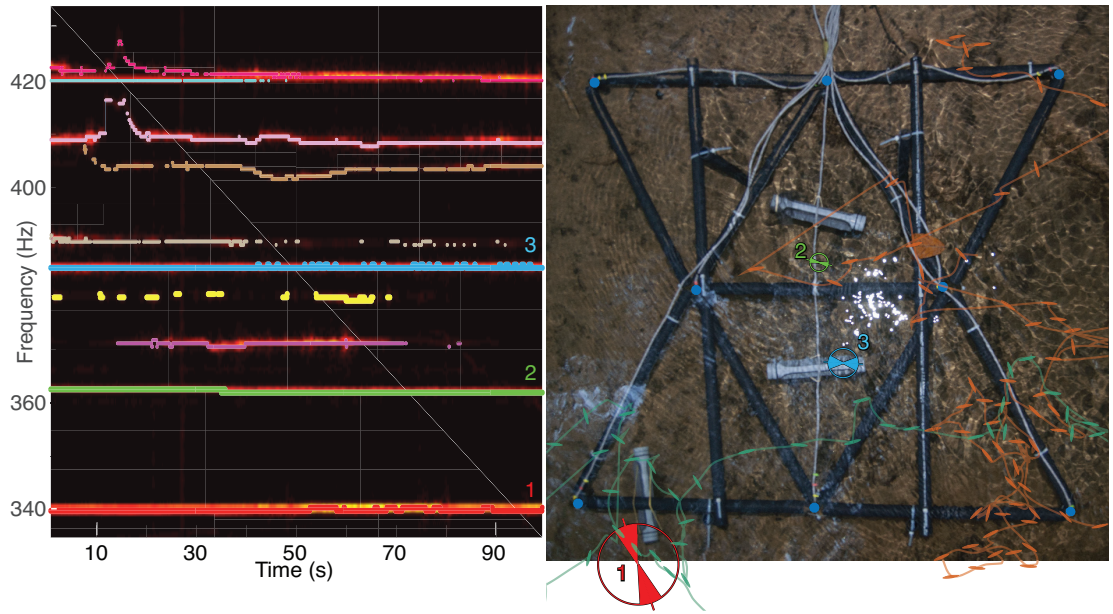


Figure 2.8: A grid of 8 electrodes was deployed at a field site in Brazil (right). Three fish were captured, their baseline EOD frequencies recorded, and placed in tubes. Signals were recorded from the grid electrodes, while other free electric fish swam within the grid. The spectrogram of the recorded data (left) reveals several tracks, including those belonging to the restrained fish (marked as 1-3). We traced the locations of all the *Eigenmannia* that entered the grid area during the trial. The trajectories of two freely swimming fish are shown as examples on the right, with their orientations indicated at several locations. For the restrained fish, the mean and two standard deviations of the position estimate is marked using circles, and the mean and two standard deviations of the orientation estimate is marked using wedges within the circles.

Dataset		Position RMSE (cm)	Orientation RMSE (deg)
TerraRonca_01	Fish 1	6.6	9.9
	Fish 2	10.6	3.1
	Fish 3	16.5	12.6
TerraRonca_02	Fish 1	33.8	57.9
	Fish 2	43.9	50.1
	Fish 3	15.6	6.1
TerraRonca_03	Fish 1	13.1	22.9
	Fish 2	8.6	5.6
	Fish 3	7.6	4.5
TerraRonca_04	Fish 1	13.1	6.6
	Fish 2	19.3	28.5
	Fish 3	17.3	4.7

Table 2.1: Root-mean-squared-errors (RMSE) of position and orientation estimates in the field. We performed four 100 s recordings in the field (TerraRonca_01 through TerraRonca_04), each of which had three fish restrained in tubes, and estimated their poses. The position RMSE which are not within the length of the tube (20 cm, ≈ 1.5 fish body lengths) and angular RMSE which are not within 15° are shaded.

2.2.2 Dipole moment strength comparison between epigean and hypogean subpopulations of fish.

Recently, a species of troglobitic *Eigenmannia*, which are either eyeless or have vestigial eyes, was discovered in a cave in Brazil (San Vincente II) within the Terra Ronca State Park ($13^\circ 30' - 13^\circ 50' S$, $46^\circ 0' - 46^\circ 30' W$). To compare between these cave fish with their epigean relatives from a nearby river (Rio da Lapa), electrosocial and swimming behaviors were recorded at these field sites using a 16-electrode grid with 0.5 meter spacing placed into the streams. Dipole strength estimation shows that the electric field strength of the hypogean fish were dramatically increased relative to their epigean relatives (2.9, E. Fortune et al., 2019).

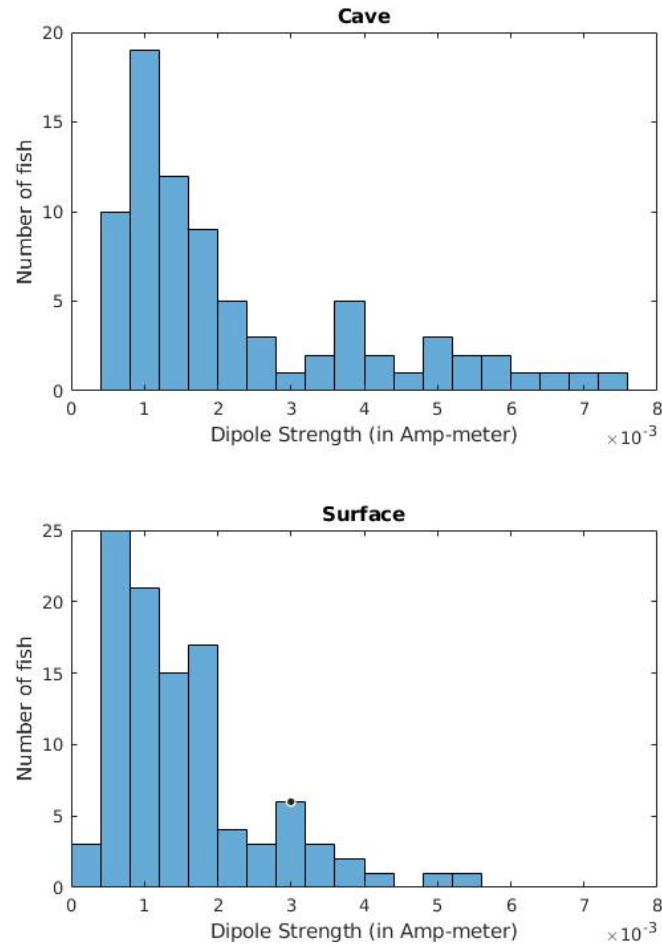


Figure 2.9: Population distribution of fish dipole strengths at cave and surface sites. Top panel shows the distribution of estimated dipole moments of the hypogean subpopulation discovered in a cave in Brazil (San Vincente II) within the Terra Ronca State Park. Bottom panel shows the distribution of estimated dipole moments of the epigeal population from a nearby surface site. Dipole moment in Amp-meter is shown on the x-axis. The y-axis shows the number of fish. The hypogean population distribution has a peak at a higher dipole moment value and a longer tail as compared to the epigeal population.

2.3 Contributions

The contributors to this work were Ravikrishnan P. Jayakumar(R.P.J.), Manu S. Madhav (M.S.M.), Alican Demir(A.D.), Sarah A. Stamper(S.A.S.), Maria Elina Bichuette (M.E.B.), Daphne Soares (D.S), Eric S. Fortune(E.S.F.), and Noah J. Cowan(N.J.C.). R.P.J. developed and implemented the spatial tracking and dipole moment estimation algorithm and associated GUI. M.S.M. developed and implemented the frequency tracking algorithm and associated GUI. A.D. designed the electrode assembly and circuit, and performed the calibration tests on the electrode amplifier circuit. S.A.S., M.S.M. and R.P.J. performed the laboratory experiments and analyzed the data. S.A.S. and E.S.F. collected preliminary field data used to develop the algorithm and E.S.F., M.E.B., and D.S. collected the final field data from the Terra Ronca site. R.P.J. generated the final spatial trajectories from laboratory and field data and performed the dipole moment estimation contributions, and M.S.M. performed the statistical shuffling tests. N.J.C. and E.S.F. guided the development of the spatio-spectral tracking algorithms, and oversaw the testing and analysis of the electrode array and laboratory experiments.

Chapter 3

Discussion

The material from the discussion section of Madhav et al., 2018, of which I am the co-first author, has been used largely verbatim to form parts of this Chapter

Weakly electric fish are nocturnal and commonly live in silty, complex habitats, making video tracking generally impossible. Fortunately, these fish betray their position by continuously generating autogenous electric signals for communication and for detecting and characterizing nearby objects. We eavesdropped on these signals using a grid of custom electrodes as the fish swam in their natural Amazonian habitats. We tracked each individual's electric field frequency and used the relative distribution of amplitudes and phases across the electrodes to estimate the 3D position and orientation of each fish. In a sense, we tackled a similar inverse problem as the electrosensory system of the fish—finding the location and orientation of objects in the environment using spatially distributed measurements of electric fields, an idea that has also been explored in bio-robotic electric navigation (Snyder et al., 2012; Boyer et al., 2012).

In order to reliably record EODs in the wild, we designed and custom-built electrodes with a built-in active amplifier and filter. The amplifier helps minimize recording noise, and the filter retains frequencies from our species of interest, *Eigenmannia*. The electrodes are arranged in a spatially distributed grid. The electrode grid needs to be constructed and repaired with material easily sourced in the country of recording and deployed by boat in remote locations. The electrodes are independently powered from a central power supply which is situated in a boat or on land near the grid. This ensures that the failure of one electrode would not disrupt the experiment. Due to convenience (cost, sturdiness, etc.) of construction and deployment restrictions, we restricted the design of the grids to two-dimensional arrangements that can be constructed using locally-available PVC pipe fittings. We designed the laboratory grid to simulate the field grid as much as possible. We used the same electrodes that were used in the field, as well as a PVC support structure which was at the water surface.

Frequency analysis over time inherently involves a trade-off between spectral and temporal resolutions. The complex numbers obtained as the spectrogram of the raw electrode potential signals are sensitive to the size of the each temporal window, the windowing (weight) function used, and the size of overlap between windows. Moreover, a practical implementation also has to trade-off and optimize computational time. We chose the spectrogram parameters through trial and error, but verified these parameters on both laboratory and field data. It is often possible to spot frequency traces

in the spectrogram amplitudes; thus when the frequency tracking is implemented on field data, it goes through manual scrutiny where we verify that the algorithmically generated frequency tracks do "line up" with observed spectrogram tracks. We developed a GUI which allows the person doing the analysis to manually intervene, and add, delete or re-assign whole or parts of frequency tracks. Of course, these edits are also recorded so that during spatial localization, frequency tracks can be used with or without manual intervention.

Each of the tracks generated by the frequency tracking algorithm correspond to the electric signal of individual fish. The spatial localization algorithm uses the amplitudes and phases measured at each of the tracked frequencies over time, in order to estimate the position and orientation of each fish. Spatial localization is thus made independent of the number of fish, since in effect, spatial tracking is performed on each fish independently. We were able to calibrate our algorithms using data collected in the laboratory when we had known fish positions and also at a field site in Brazil where restraining the fish and position visibility was attainable.

The spatial tracking algorithm is a particle filter that relies on simulating large number of "fish" at initially random locations, and having these populations converge to the true position and orientation of the fish. A large number of particles approximate the true posterior probability distribution of the fish, however it is computationally expensive to simulate large particle groups and to compute their statistics. The particles are assumed to be ideal electric dipoles. Even though this is true for *Eigenmannia* in general, individual

fish can vary in their electric field structure. Fish also bend their bodies and thus can distort their electric field temporarily. Also, the ideal dipole model assumption breaks down close to the dipole source. Since fish within the grid sometimes swim right next to an electrode, the reading at that electrode is less reliable. The model used for simulating electrode readings also assumes that the environment around the dipole source and measurement electrode is homogeneous. The environment around the grid in the field is clearly not homogeneous, since the fish generally live in littoral environments, and sometimes in shallow water of varying depth. In the laboratory, the insulating walls of the acrylic tank produce a non-homogeneous boundary conditions. As we describe in the results, the accuracy of spatial tracking under these conditions can be compromised.

Previous work demonstrated the feasibility of using a multi-electrode array to spatially localize pulse-type weakly electric fishes (Jun, Longtin, and Maler, 2013). This approach, designed for behavioral observation in a laboratory setting, is similar to ours in that simulated electrode readings based on a dipole model are compared with actual readings from the fish. They take advantage of the known geometry of the tank and water surface boundaries to account for boundary effects in the simulated readings. A shallow water depth also allowed them to use a planar dipole model.

Field recordings, by contrast, occur under much more uncontrolled conditions, such as environmental noise sources corrupting the signal, unknown boundary conditions and variable water depth. Since the electrode grid is constructed on site under less than ideal conditions, there can also be small

uncertainties about the geometry of the grid of electrodes. We use a Bayesian approach, specifically the particle filter, to deal with such noisy recordings. This allows us to construct the posterior probability density function of the fish's state based on all available information. This distribution would, in principle, yield an optimal estimate of the state as well as a measure of confidence (Arulampalam et al., 2002).

These methods were developed to study the social and locomotor dynamics of weakly electric fish that live in habitats where video tracking is generally not possible. This is due to the fact that these nocturnal fish commonly live in turbid water and in complex root and littoral habitats. There have been previous efforts to localize these fish using spatially distributed electrode recordings; however, these approaches have been limited to a laboratory setting on a single fish (Jun, Longtin, and Maler, 2013), or on a fish analog (Snyder et al., 2012). We tracked *Eigenmannia virescens*, a species of Gymnotiform fish, in both laboratory and field settings, and our method is specifically aimed at chronic behavioral recordings of these animals in the wild.

Weakly electric fish, *Eigenmannia virescens* exhibit indications of a complex electrosocial behavior in their natural habitats. The results in Chapter describe the estimation of the frequency and spatial trajectory of the individuals comprising the recorded population of fishes. This enables us to determine if two fish are within biologically salient distances of each other and consequently, to start to discern the nature of specific behaviors exhibited by a fish and what sort of responses this elicits from its neighboring conspecifics. In addition to the spatial distances, given that the electric field generated by the fish can be

approximated by a dipole model, the relative orientation between the fish may also have particular significance in behavioral epochs such matching of EOD frequencies, particularly if the fish are parallel to each other. Two candidate cases are:

- The dipole oscillation of the two fish are in phase
 - If the fish are close enough, the two fish may act as a single dipole of a higher strength. This may serve a cooperative strategy to enhance the sensing abilities of both fish.
- The dipole oscillation of the two fish are antiphase
 - This may occur due to the natural interaction of charges in a dipole. Specifically, if the two fish are close to and parallel to each other, a charge of one polarity at one end of the dipole on a fish may make it more probable for a charge of the opposite polarity to be at the proximal end of the dipole on the other fish.

The ability to estimate a fishes' dipole moment strength is of high biological significance. The results showing higher dipole moment strengths of hypogean fish relative to their epigean relatives exemplifies how troglobitic animals often exhibit dramatic differences in behavior and in the size and structure of sensory organs when compared to their epigean relatives. These differences can include the loss of eyes and the emergence or elaboration of other sensory organs.

Weakly electric fish have been a valuable model system for furthering our understanding of social communication. In the laboratory, it is known that fish

modulate their frequency in very short timescales for social communication signal. Frequency behaviors such as Jamming Avoidance Response (JAR) and Social Envelope Response (SER) have never been observed in the wild context. Spatial behaviors are interesting in terms of understanding social dynamics, but also to see if JAR, SER etc. have motion correlates. The knowledge of baseline frequency and dipole moment strength as an indicator of gender and social dominance, combined with frequency transitions and spatial motion as indicators of aggressiveness, sexual selection or cooperation, can significantly enrich social behavior analysis.

The spatiotemporal resolution and accuracy of the grid system permits the observation of currently unknown parameters of locomotor-related behaviors, particularly social behavior. The system can resolve the numbers and movements of fish in groups, which is known to vary between species (S. Stamper et al., 2010; Oestreich and Zakon, 2005; Tan et al., 2005b). We will, for the first time, be able to identify the transit of individuals across territories and through groups, providing insight into the parameters that govern these differences in behavior (see Henninger et al., 2017). However, close interactions (less than one body length distance), which can include body contacts, biting, and complex poses (Hupé and Lewis, 2008), cannot be determined using this system. These important social behaviors are of interest to biologists but are unlikely to be resolvable using the current technology.

Weakly electric fish are distributed through much of the Amazon basin and are known to be sensitive to environmental perturbations (Thomas, Floiron,

and Chretien, 1998; Geller, 1984) making them a bellwether for changes to critical Amazonian habitats. The technology presented in this paper, which takes advantage of the continuous electrical signals produced by these animals, can be scaled for widespread monitoring of these fish and therefore of environmental impacts of human activity: the custom amplifiers are composed of a simple, low-power, inexpensive circuits, readily integrated into autonomous systems that automatically capture and upload data. These data can be analyzed to assess behavioral activity, species distributions and diversity.

The application for these analysis techniques is promising for data collected in natural habitats. Researchers measure as many parameters as possible including conductivity, location of visible objects (tree roots, etc.), water depth, at each site to facilitate the use of the frequency tracking and spatial localization algorithms. The data is monitored in real-time to allow the adjustment of electrodes and grid placement. However, there is much in the environment that can not be controlled including noise sources, weather disturbance of site by other animals, etc. Thus, estimating fish position in the wild will likely be more variable. However, based on the analysis to date, we are confident that our methods will be applicable under such conditions. This data will give insights into the sensory milieu of the fish and inspire future neurophysiological and behavioral experiments in the laboratory to gain a more controlled understanding of the mechanisms underlying processing electrosensory signals.

Part II

Rattus norvegicus domestica

Investigation of the role of path integration in the hippocampal spatial map

Chapter 4

Recalibration of path integration in hippocampal place cells

Aside from Figure 4.4, the rest of this chapter is reproduced verbatim from Jayakumar et al., 2019 of which I was the co-first author.

Hippocampal place cells are spatially tuned neurons that serve as elements of a "cognitive map" in the mammalian brain (O'Keefe and Nadel, 1978). To detect the animal's location, place cells are thought to rely upon two interacting mechanisms: sensing the animal's position relative to familiar landmarks (Acharya et al., 2016, Chen, King, Burgess, and O'Keefe, 2013) and measuring the distance and direction that the animal has traveled from previously occupied locations (Etienne and Jeffery, 2004, Wehner and Menzel, 1990, Wittlinger, Wehner, and Wolf, 2006, M. .-L. Mittelstaedt and H. Mittelstaedt, 1980). The latter mechanism, known as path integration, requires a finely tuned gain factor that relates the animal's self-movement to the updating of position on

the internal cognitive map, with external landmarks necessary to correct positional error that accumulates (Gallistel, 1990, Samsonovich and McNaughton, 1997). Path-integration-based models of hippocampal place cells and entorhinal grid cells treat the path integration gain as a constant (Samsonovich and McNaughton, 1997, Fuhs and Touretzky, 2006, McNaughton, Battaglia, et al., 2006, Hasselmo, Giocomo, and Zilli, 2007, Blair, Gupta, and Zhang, 2008, Burgess, Barry, and O'Keefe, 2007), but behavioral evidence in humans suggests that the gain is modifiable (Tcheang, Bulthoff, and Burgess, 2011a). Here we show physiological evidence from hippocampal place cells that the path integration gain is indeed a highly plastic variable that can be altered by persistent conflict between self-motion cues and feedback from external landmarks. In a novel, augmented reality system, visual landmarks were moved in proportion to the animal's movement on a circular track, creating continuous conflict with path integration. Sustained exposure to this cue conflict resulted in predictable and prolonged recalibration of the path integration gain, as estimated from the place cells after the landmarks were extinguished. We propose that this rapid plasticity keeps the positional update in register with the animal's movement in the external world over behavioral timescales. These results also demonstrate that visual landmarks not only provide a signal to correct cumulative error in the path integration system (Etienne and Jeffery, 2004, Gallistel, 1990, Knierim, Kudrimoti, and McNaughton, 1998b, Zugaro et al., 2003, Hardcastle, Ganguli, and Giocomo, 2015b, Etienne, R. Maurer, and Séguinot, 1996), but also rapidly fine-tune the integration computation itself.

Path integration is an evolutionarily conserved strategy that allows an

organism to maintain an internal representation of its current location by integrating over time a movement vector representing distance and direction traveled (Etienne and Jeffery, 2004, Wehner and Menzel, 1990, Wittlinger, Wehner, and Wolf, 2006, M. .-L. Mittelstaedt and H. Mittelstaedt, 1980). Place cells and entorhinal grid cells have been implicated as key components of a path integration system in the mammalian brain (E. I. Moser, M.-B. Moser, and McNaughton, 2017, Gil et al., 2018, Tennant et al., 2018). We recorded place cells from area CA1 (Extended Data Fig. 4.5) in 5 rats as they ran laps on a 1.5 m diameter circular track. The track was enclosed within a planetarium-style dome where an array of three visual landmarks was projected onto the interior surface to create an augmented reality environment (Fig. 4.1 a,b). In contemporary virtual reality systems (Chen, King, Burgess, and O'Keefe, 2013, Hölscher et al., 2005, Harvey et al., 2009, Ravassard et al., 2013b), head- or body-fixed rats fictively locomote on a stationary air-cushioned ball or treadmill. Notwithstanding the flexibility of these systems to manipulate the visual experience of the animal, we built the dome apparatus to instead more completely preserve natural self-motion cues, such as vestibular, proprioceptive, and motor efference copy. This system enabled us to test the a priori hypothesis that manipulating the animal's perceived movement speed relative to the landmarks results in a predictable recalibration of the path integration gain.

To create the visual illusion that the animal was running faster or slower, the array of landmarks was rotated coherently as a function of the animal's

movement speed. Movement of the landmarks was controlled by an experimental gain, G , which set the ratio between the rat's travel distance with respect to the landmarks (landmark reference frame) and its travel distance along the stationary circular track (laboratory reference frame) (Fig. 4.1c). Recording sessions began with $G = 1$ (Epoch 1), a control condition with landmarks held stationary, so that the rat traveled the same distance in both the landmark and lab frames (Fig. 4.1d). The gain was then ramped over the course of multiple laps (Epoch 2) to values less than or greater than one. For $G < 1$, the landmarks moved at a speed proportional to (but slower than) the rat in the same direction; hence, the rat ran a shorter distance in the landmark frame than in the lab frame. For $G > 1$, the landmarks moved in the opposite direction; hence, the rat ran a greater distance in the landmark frame than in the lab frame. In Epoch 3, G was held at a steady-state target value (G_{final}). In some sessions, the landmarks were then extinguished (Epoch 4) to assess whether the effects of gain adjustment persisted in the absence of the landmarks.

4.1 Results

Under gain-adjusted conditions, CA1 units (mean 7.2 ± 5.8 S.D. units/session) tended to fire in normal, spatially specific place fields when the firing was plotted in the landmark frame, but not when plotted in the lab frame (Fig. 4.1e). The strength and continuity of visual cue control over the place fields is highlighted by special cases of G (Fig. 4.2). As G was ramped down to 0, the place fields became increasingly large in the lab frame, eventually spanning

multiple laps (Fig. 4.2a), but they maintained normal spatial selectivity in the landmark frame (Fig. 4.2b). At $G = 0$, the animal's position became locked to the landmark frame, as the landmarks moved in precise register with the rat. Consequently, a unit that was active at that moment would typically remain active throughout Epoch 3, (e.g. yellow unit, Fig. 4.2a); in contrast, a unit that was inactive at that moment would typically remain silent throughout Epoch 3 (e.g. red unit, Fig. 4.2 a). When G was clamped at integer ratios such as 3/1 (Fig. 4.2c) or 1/2 (Fig. 4.2e), the units maintained the typical pattern of one field/lap in the landmark frame, while firing at the expected periodicity such as 3 times per lap (Fig. 4.2d) or every other lap (Fig. 4.2f) in the lab frame. Remapping events sometimes caused different populations of place cells to be active at different times. For example, place cells active during the initial part of the session sometimes went silent (loss of field; Fig. 4.2e, yellow unit), and place cells silent during the initial part of the session sometimes began firing at a preferred location (gain of field; Fig. 4.2e, red unit). The remapped cells exhibited normal place fields only in the landmark frame. These examples illustrate that the landmark array exercised robust control over the place fields, outweighing any subtle, local cues on the apparatus as well as nonvisual path integration cues, such as vestibular or proprioceptive cues.

To quantify the degree of landmark control over the population of recorded place cells, we developed a novel decoding algorithm that was robust to the remapping events described above. We estimated the gain, H_i , for each individual unit, i , by measuring its spatial frequency (i.e., the frequency of repetition of its spatially periodic firing pattern). The median value of H_i over

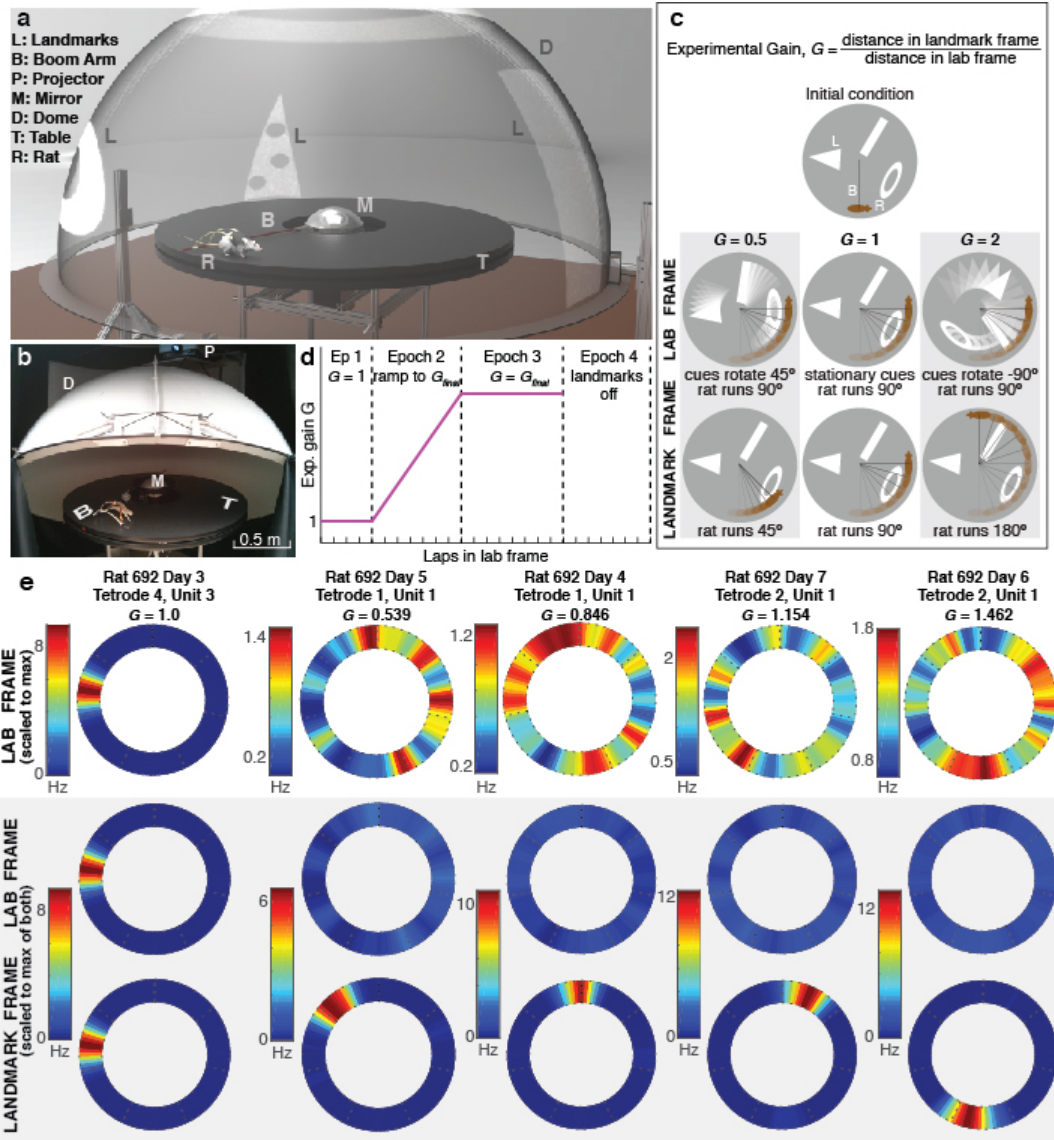


Figure 4.1

Figure 4.1 (previous page): Dome apparatus, experimental procedure, and sample data. (a) Semi-transparent illustration of the dome apparatus. (b), Photo of the apparatus. The dome is raised to allow visualization of the interior, but it is lowered as in (a) for the experiment. (c) Illustration of experimental gain G . From the same initial positions of the landmarks and rat, three gain conditions are shown, in both lab (top) and landmark (bottom) frames of reference. In each case, the rat runs 90° in the lab frame. (d), Profile of gain change and epochs during a typical session. An annular ring is always projected at the top of the dome (as shown in (a)) for illumination purposes, and is not turned off even in Epoch 4. (e) Representative firing rate maps for five different units from five separate gain manipulation sessions, shown in the lab frame (top, middle rows) and landmark frame (bottom row) during Epoch 3 (constant experimental gain). Plots in the top row are color scaled to their own individual maximum firing rates; middle and bottom row plots are color scaled to the maximum firing rate of the bottom plot of each pair.

all simultaneously recorded active units during a given set of laps was taken as a population estimate of the hippocampal gain, H , for those laps. Just as G quantifies the ratio between the rat's travel distance in the landmark frame versus lab frame, H quantifies the ratio between the rat's travel distance in the internal hippocampal "cognitive map" frame (OKeefe and Nadel, 1978) versus the lab frame. An ensemble coherence score for each unit was computed as the mean value over the session of $|1 - H_i/H|$, measuring the deviation of H_i from H . The distribution of coherence scores (Fig. 4.2g) shows that H_i was within 2% of H for 80% (399/500) of individual units, and deviations greater than 5% were rare. Even when individual cells remapped, they still exhibited spatial periodicity at gain factors H_i that were close to H (see red and yellow units in Fig. 4.2c). Hence, the population of place cells acted as a rigidly coordinated ensemble from which a precise estimate of H could reliably be computed, despite occasional remapping by some place cells.

The degree of cue control in each session was quantified by the mean ratio

H/G for Epochs 1-3 of a session; a ratio close to 1 indicates that the cognitive map was anchored to the landmark frame (i.e., $G = H$). The majority of sessions (83.33%) exhibited H/G near 1, but the rest showed substantially larger ratios ($H/G > 1.1$) indicating loss of landmark control (Fig. 4.2h; Extended Data Fig. 4.6). For sessions with $H/G < 1.1$, the spatial information per spike in the landmark frame far exceeded that in the lab frame (Fig. 4.2i). Further quantitative analyses was restricted to these sessions demonstrating 'landmark control'. These results indicate that the augmented reality dome was successful in producing the desired illusion by strongly controlling the spatial firing patterns of the hippocampal cells in the majority of sessions (Extended Data Figs. 4.7 4.8).

Despite strong cue control in the majority of sessions, place fields nonetheless tended to drift systematically by a small amount against the landmark frame on each successive lap (Extended Data Fig. 4.9; also visible in Figs. 2a,c,e and 3a,b) leading to total drifts of up to $\sim 80^\circ$ over the course of a session. The direction of this bias was consistent with a continuous conflict between the dynamic landmark reference frame and a path-integration-based estimate of position (although we cannot rule out the possible contribution of subtle uncontrolled external cues on the track or in the laboratory). That is, when path integration presumably undershot the landmark-defined location systematically ($G < 1$), the place fields shifted slightly backwards in the landmark frame; conversely, when path integration overshot the landmarks ($G > 1$), the place fields shifted forward. The shift may reflect a conflict resolution that is weighted heavily, but not completely, in the direction predicted by the

landmark frame.

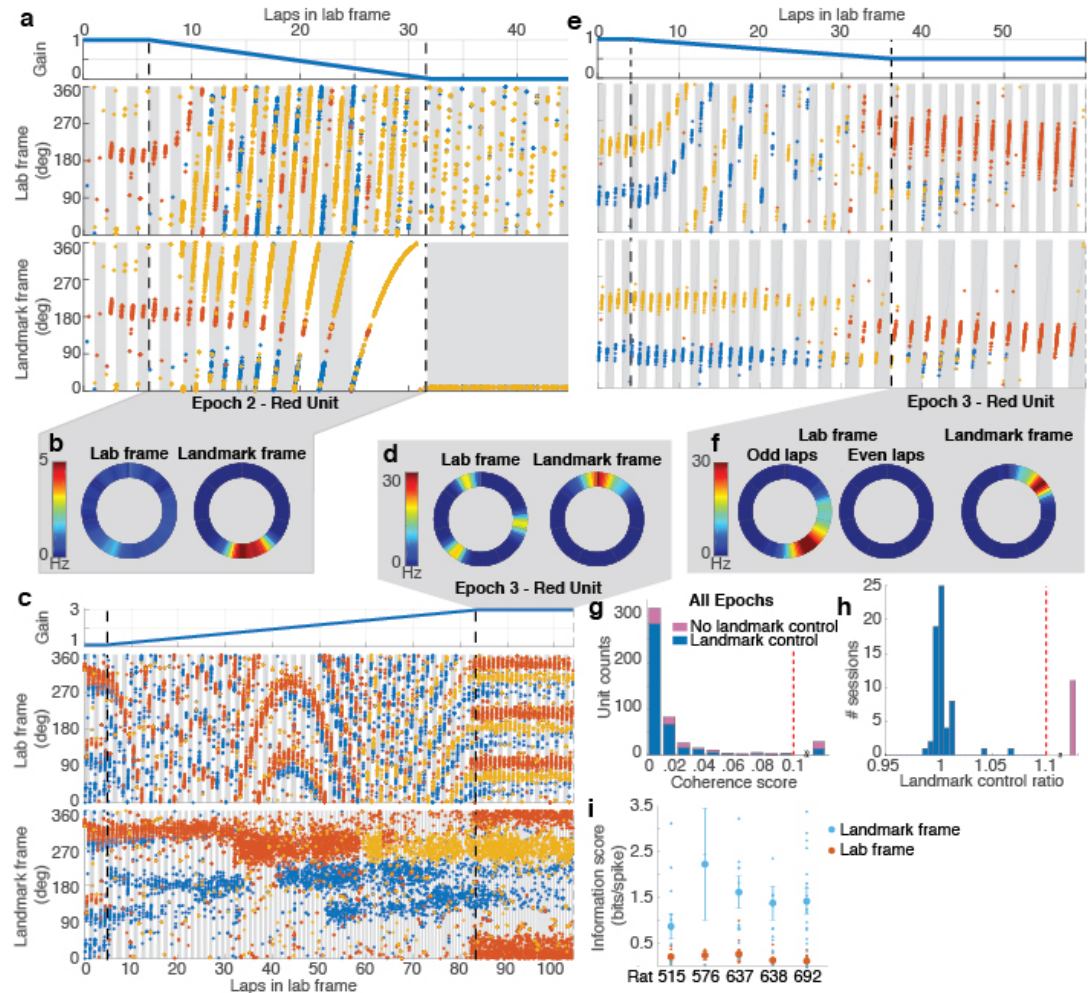


Figure 4.2 (previous page): Control of place fields by landmarks. (a) (top) Profile of experimental gain, G , for Epochs 1-3 of a session where G_{final} was 0. (middle) Colored dots show the location of the rat in the lab frame (y axis) as a function of cumulative distance traveled on the track (x axis) when spikes from 3 units (red, blue, yellow) were recorded. Alternate gray and white bars indicate laps in this frame. (bottom) The same spikes in the landmark frame. Alternate gray and white bars indicate laps in this frame. The yellow unit fired weakly during the first 8 laps, became stronger on laps 9-10, and maintained the strong field in the landmark frame throughout the remainder of the session. During the last landmark-frame lap, the unit fired in a field that spanned $\sim 1080^\circ$ (3 laps) in the lab frame (middle). (b) Rate maps of the red unit in lab and landmark frames for Epoch 2 of the trial shown in (a). The firing rate is low and diffusely distributed (on average) in the lab frame, whereas there is a well-defined place field in the landmark frame. (c) Epochs 1-3 of a session where the G_{final} was 2 (same format as (a)). In Epoch 3, all three units maintain normal spatial firing in the landmark reference frame, but they have 3 fields/lap, separated by 120° , in the lab frame. (d) Rate maps of the red unit for Epoch 3 of the trial shown in (c). (e) Epochs 1-3 of a session where the G_{final} was 0.5. Remapping occurred near the transition between Epoch 2 and Epoch 3, as the previously silent red unit became active and maintained a stable place field in the landmark frame. In the lab frame, however, the unit fired every other lap, (i.e., it was active on the gray laps and silent on the intervening white laps). (f) Rate maps for the red unit for Epoch 3 of the trial shown in (e). Separate rate maps are shown for the odd- and even-numbered laps in the lab frame. (g) Coherence of the population response. The $n = 500$ units acted as a coherent population in sessions with (blue, 411/500) and without (pink, 89/500) landmark control (see panel h). Units with coherence score above 0.1 (range 0.12 - 0.47) were combined in a single bin (29/500 units). These cells generally displayed poor spatial tuning and therefore did not admit a reliable estimate of hippocampal gain. (h) Landmark control ratio. In most sessions (blue, 60/72), the landmark control ratio was ~ 1 . Sessions with gain ratio above 1.1 (range 1.16 - 4.02) were combined in a single bin (pink, 12/72). (i) Spatial information scores in the lab and landmark frames for each rat (sessions with $n = 12, 3, 17, 15, 29$ units) are significantly different (two-sided paired t-test, $n = 5$ rats, $t_4 = 6.213$, $p = 0.0034$). Small dots represent scores from individual units. Mean (large dots) \pm s.e.m. are shown.

Given the apparent influence of path integration on place cells, revealed by systematic place-field drift despite strong landmark control, we tested whether anchoring of the cognitive map to the gain-altered landmark frame induced a recalibration of the path integrator that persisted in the absence of landmarks. Such recalibration would be evidenced by a predictable change in

the hippocampal gain H when visual landmarks were extinguished (Fig. 4.1d, Epoch 4). The baseline hippocampal gain H was measured for each animal after extinguishing landmarks in sessions where the rat ran ~ 30 laps with stationary landmarks ($G = 1$). As expected, the baseline value of H was close to 1 (range 0.997 - 1.036). In subsequent gain manipulation sessions, if the path integrator circuit were unaltered, one would expect the place fields to revert to the lab frame ($H \approx 1$) when landmarks were extinguished, as in the baseline sessions. Alternatively, if the path integrator gain were recalibrated perfectly, one would expect that the place fields would continue to fire as if the landmarks were still present and rotating at the final experimental gain (i.e., $H \approx G_{final}$). We found that the hippocampal representation during Epoch 4 was intermediate between these extremes (Fig. 4.3): there was a clear, linear relationship between G_{final} and the hippocampal gain H estimated during the first 12 laps after the landmarks were turned off (Fig. 4.3c). Moreover, this linear relationship was maintained when H was estimated during the next 12 laps (Extended Data Fig. 4.10). The values of H for the first and second 12 laps were highly correlated (Fig. 4.3d) with a slope near 1 (1.03). Thus, H was stable over at least 18 laps (i.e., the middle of the second estimation window). Despite this overall stability, there were still fluctuations in H in the absence of landmarks (Fig. 4.3e, Extended Data Fig. 4.10). We tested whether changes in behavior could account for the hippocampal gain recalibration by computing several behavioral measures for each epoch (Extended Data, Behavioral Analysis). Multiple regression analysis showed that G_{final} strongly predicted H , whereas the behavioral variables had negligible influences on H (Extended Data Table 4.1).

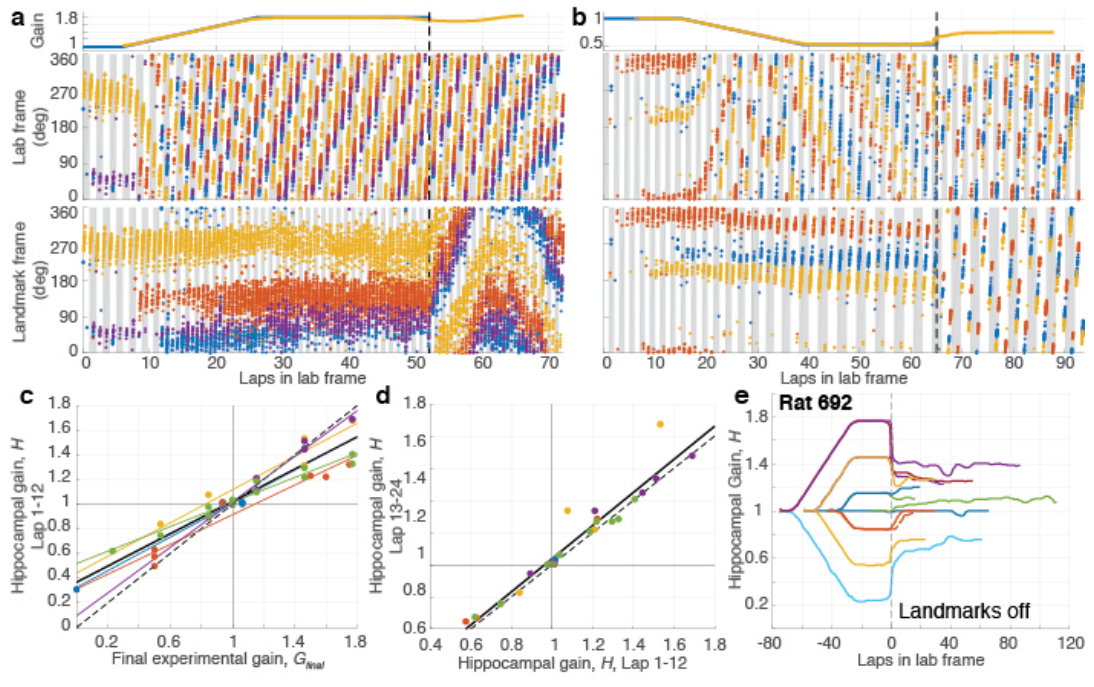


Figure 4.3

Figure 4.3 (previous page): Recalibration of place fields by landmarks (a) Example of positive recalibration. (top) Experimental gain, G (blue) and hippocampal gain, H (yellow) for Epochs 1-3 of a session in which the G_{final} was 1.769. (middle) Spikes from three putative pyramidal cells (blue, red and yellow dots) in the lab frame. (bottom) The same spikes in the landmark frame. When the landmarks were turned off (dashed line, Epoch 4), H remained close to G_{final} , shown by the slower drift of the place fields in the landmark frame compared to the lab frame. (During Epoch 4, the landmark frame was defined assuming the gain was G_{final} even though landmarks were off.). Note that the traces of H (yellow) deviate from G (blue) prior to the landmarks turning off; this is an artifact of the sliding window used in the spectrogram and does not affect the conclusions (see Methods, Visualizing H). (b) Example of negative recalibration. The G_{final} was 0.539. (c) Recalibration of place fields. The x-axis is G_{final} and the y-axis is H computed using the first 12 laps (i.e., the value of H at lap 6) after the landmarks were turned off. Linear fits for each animal (color) and for the whole data set (black) are shown ($n = 45$ sessions, Pearson's $r_{43} = 0.94$, $p = 3.4 \times 10^{-21}$), along with the perfect recalibration line (dashed line, black). Note that the linear fit passes close to the origin, showing that $H \approx 1$ when the landmarks were extinguished after baseline control experiments. (d) Stability of recalibration. Comparison of H during laps 1-12 vs. H during laps 13-24. The linear fit is shown in black. ($n = 27$ sessions, Pearson's $r_{25} = 0.96$, $p = 1.16 \times 10^{-15}$) (e) Complete gain dynamics for one animal. For all sessions from one rat, H is plotted as a function of laps run in the lab frame. All the sessions are aligned to the instant when the landmarks were turned off (lap 0). The recalibrated H was maintained for as many as 50 laps or more.

4.2 Methods

4.2.1 Subjects

Five male Long-Evans rats (supplier Envigo Harlan) were housed individually on a 12:12 hour light-dark cycle. All training and experiments were conducted during the dark portion of the cycle. The rats were 5-8 months old and weighed 300-450 g at the time of surgery. All animal care and housing procedures complied with National Institutes of Health guidelines and followed protocols approved by the Institutional Animal Care and Use Committee at Johns Hopkins University.

4.2.2 Dome apparatus

The virtual reality dome apparatus that we designed for this experiment is similar to a planetarium. The hemispherical dome was constructed from fiber glass (Immersive Display UK, Ltd, Essex, UK). The inside surface was uniformly coated with a 50% reflective paint (RAL7040 grey). A hole (15 cm diam.) at the top of the dome allowed light from a video projector (Sony VPL-FH30) with a long-throw lens (Navitar ZM 70-125 mm) to enter. Visual cues were projected onto the inside surface of the dome (Fig. 4.1). An annular ring of light was projected onto the top, interior surface of the dome; when the spatial landmarks were turned off in Epoch 4, this ring remained on to provide nondirectional illumination.

An annular table (152.4 cm outer diam, 45.7 cm inner diam.) was centered within the dome. The support legs of the dome and the legs of the table were not visible to the rat during the experiment. A commutator (PSR-36, Neuralynx Inc.) was mounted in the center of, but slightly below, the tabletop. The commutator drum was upward, inverted from the typical, ceiling-mounted installation. A hemispherical first-surface mirror (25 cm diam.; JR Cumberland, Inc, Marlow Heights, MD, USA) was mounted to the commutator drum. The image from the projector was reflected off of the mirror and onto the interior surface of the dome. A radial arm (6 mm carbon fiber rod) extending almost to the edge of the table was attached to the central commutator through a smooth bearing. The angle of rotation between the arm and the commutator drum was monitored by a built-in optical encoder. A microcontroller actuated a stepper motor attached to the commutator drum to maintain this angle close

to zero, effectively rotating the drum of the commutator along with the radial arm. The rate of rotation of the motor, and correspondingly its auditory noise frequency, was proportional (up to a saturation point) to the speed of the rat in the lab frame. The noise could thus potentially serve as an artificial (learned) self-motion cue. If so, the results indicate either that this cue is inconsequential for path integration updating or it is recalibrated along with the natural self-motion cues (i.e., vestibular, motor copy, proprioception, etc.).

Two 3D-printed 'chariot' arms for harnessing the rat were attached to the radial arm near the edge of the table. Other lightweight 3D printed components were sometimes attached to the radial boom arm to affix infrared lights, feeding tubes, recording tether supports, etc. The rat wore a body harness (Coulbourn Instruments, Whitehall, PA, USA), onto which Velcro strips and a magnetic attachment pad were sewn. The magnets helped align the harness to paired magnets attached to the chariot arms and the Velcro strip held the rat in that position relative to the arms. During the experiment, the rat pulled along the arm and the components attached to it. Due to the long lever provided by the radial arm and the smooth bearing attachment to the commutator, the load borne by the rat was minimal.

A liquid reward vial and pump and a battery to power the pump and IR lights were mounted to the commutator drum. The commutator drum was connected to a second optical encoder (Hohner Corp., Beamsville, Ontario, Canada) that measured its angular displacement relative to the table. Hence the angle of the rat in the lab frame was the sum of the angle measurement from the two encoders (i.e., the angle of the commutator relative to the table

and the angle of the radial arm relative to the commutator). A Hall effect sensor (55100-3H-02-D, Littelfuse Inc., Chicago, IL, USA) mounted to the table, and a corresponding magnet mounted to the commutator drum, were used for post-hoc detection and correction of any spurious jumps in rat angle. To mask auditory cues emanating from outside the dome during the experiments, white noise was played by a speaker placed centrally underneath the table.

A camera was mounted next to the hole at the top of the dome and was hidden from the animal using an annular, concentrically mounted one-way mirror that encircled the hole, occluding the camera from view. The camera provided an overhead view of each experiment, which allowed observation of the experiments and experimenter intervention when necessary (e.g., if the rat broke free from the harness). During the experiments, synchronized video of the rat's behavior was recorded. To verify our ability to track rat angle, we tracked the location of the boom arm post-hoc using the video recording. We implemented a template-based tracking algorithm using standard subroutines in the freely available OpenCV library (opencv.org, V 3.2.0). Based on the camera resolution (1024 x 768 for the first two animals and 2048 x 2048 for the last three animals), each pixel was calculated to correspond to $<1^\circ$ of the track. The mean absolute error between the video-based tracking and the encoder-based rat angle was small (mean: $3.60^\circ \pm 3.86^\circ$ S.D.) across all 72 sessions.

4.2.3 Training

Over 2-3 days, we familiarized the rats to human contact and to wear the body harness. The rats were placed on a controlled feeding schedule to reduce their weights to ~80% of their ad libitum weight, whereupon they were trained to run for food reward (either Yoo-hoo[®] or 50% diluted Ensure[®]) on a training table in a different room from the experimental room. Reward droplets were manually placed at arbitrary locations on the track in the path of the running rat, and the experimenter attempted to lengthen the average interval between rewards to maintain behavior while prolonging satiation. The rats were then transitioned to automatic feeding, where liquid reward was dropped at intervals that varied over time as the rats' behavior was shaped to maximize forward movement with minimal pauses. The training setup had a similar radial arm and chariot as the main apparatus, but without the surrounding virtual environment. Once the rats were consistently running 30-40 laps without human intervention on the training table, we moved them into the dome and trained them until they ran 30-40 laps in the presence of stationary visual cues. Training usually took 2-3 weeks.

4.2.4 Electrode implantation and adjustment

After training, rats were implanted with hyperdrives containing 6 (2 rats) or 12 (3 rats) independently movable tetrodes. Following surgery, 30 mg of tetracycline and 0.15 ml of a 22.7% solution of enrofloxacin antibiotic were administered orally to the animals each day. After at least 4 days of recovery, we began slowly advancing the tetrodes and resumed food restriction and

training within 7 days of surgery. Once the tetrodes were close to CA1 they were advanced less than 40 μm per day. Once the tetrodes were judged to be in CA1, as confirmed by sharp wave/ripples in EEG signals and the presence of isolatable units, and the animal was again running at least 30 laps inside the dome, the experimental sessions began.

4.2.5 Neural recording

During sessions, the rat was attached to the chariot arms and a unity-gain headstage was attached to its implanted hyperdrive. The neural signals passed through the commutator and were filtered (600-6000 Hz), digitized at 32 kHz, and recorded on a computer running the Cheetah 5 recording software (Neuralynx Inc., Bozeman, MT). Simultaneously, EEG data from each tetrode was filtered (1-475 Hz), digitized at 33 kHz, and stored on the computer. Pulses sent from the experiment-control computer (see below) were time-stamped and recorded as events on the neural recording computer to allow the post-hoc synchronization of the data streams recorded on the two computers.

4.2.6 Experimental control

The NI PCIe-6259 data acquisition system (National Instruments Inc., Austin, TX USA) was used to communicate with the dome apparatus. The experiment control was executed by a custom software system coordinated by the software development framework called Robot Operating System (Quigley et al., 2009) (ROS, Open Source Robotics Foundation, distributed under the BSD-3-Clause

License) on a computer running the Linux Operating System (Ubuntu 12.04, 14.04). The custom ROS-based system received information about the rat's angular position from the two optical encoders and generated the visual scene using standard open-source OpenGL C++ libraries. The visual scene was deformed to match the optics of the projection system and displayed on the projector mounted above the dome. The experimentally measured time lag between movement of the vehicle and movement of the landmark array was 97 ± 24 S.D. ms. The time lag was due to processing time delays as well as to the frame rate of the video projector (17 ms/frame); the jitter was due to occasional frame drops and inconsistencies in update rate due to momentary computational demands (data not shown). We also computed where the landmarks should have been projected if we had instantaneous control. There was no detectable slippage (drift) between the intended location of landmarks and where they were actually projected. The mean absolute error between these values was small for all sessions in which the landmarks were moving (i.e., non-control sessions) (54/72 sessions; mean: $0.59^\circ \pm 0.43^\circ$ S.D.; max: 1.69°).

Rats were rewarded by automatically dropping liquid reward at pseudo-random spatial intervals in the lab frame. These intervals were picked from a uniform distribution with means (typically $40\text{-}80^\circ$) specified at the beginning of each session. The mean feeding interval was increased gradually during training to delay satiation and maintain running performance, and was generally constant during each experimental session. The experimenter could also dispense reward manually to encourage running behavior when

necessary. All the data, including position of the rat, position of the visual stimuli, reward locations, and the overhead video, were saved during the course of the session.

4.2.7 Experimental procedure

On each experimental day, baseline data were recorded from the rat for 20 minutes before and after the session while it slept or rested quietly in a towel-lined dish on a pedestal. These sleep data were used post-hoc to confirm recording stability of single units during the trials. During the sessions, the experimenter went into the dome with the rat and always attached the rat to the harness at the same starting location relative to the landmarks (which always were located at the same locations relative to the lab frame). After ensuring that the rat was running with a natural gait, the experimenter left the dome. The progress of the session was monitored using the overhead camera, and the experimenter only interfered in cases when the rat partially broke free of the harness, stopped running for long periods, or was running with an unnatural gait.

The session duration varied depending on the running speed of the rat and on how many laps were planned for that session (e.g., ramps to smaller gain values required fewer laps to run the experiment). On days with short sessions, a second session was sometimes run after a short rest duration. The rat was taken out and placed on the pedestal between sessions, to keep the initial conditions consistent. Except on some days where landmarks were kept stationary for the whole duration of the experiment, we took the rat out of the

dome only during Epoch 4 (no landmarks inside dome).

4.2.8 Experimental gain selection and gain ramp rates

Each rat initially ran 1-3 sessions in which the landmarks were stationary. In most of these sessions, rats first ran 30 laps with stable landmarks ($G = 1$), and then they ran 30 laps with the landmarks extinguished, to mimic the number of laps in Epoch 3 for our regular recalibration sessions. After these initial days, subsequent days of recording varied the value of G away from 1. For the first rat (515), we chose values of G close to 1 (1.0625, 0.9375), in addition to one session with a gain of 0. For the second rat (576) we typically used gains 0.25, 0.5 and 0.75, which resulted in periodic repetitions of place fields in the lab frame. For the remaining three animals, in order to reduce ambiguity of firing patterns in the lab and landmark frames of reference, gains were selected in the form of $\frac{1}{n}$, resulting in gains of 0.231, 0.539, 0.846, 1.154, 1.462, and 1.769. These values ensured that during Epoch 3 the animal's position relative to the lab and landmark frames of reference only aligned once every 13 laps. We used gain ramp rates during Epoch 2 ranging from $\frac{1}{128}$ to $\frac{1}{26}$ (gain change per lap). The number of laps in Epoch 1 was different for each rat (4 laps for 515 and 576, 6 laps for 637 and 638, and 15 laps for 692). However, the number of laps in Epoch 1 had no apparent relationship to the degree of cue control when the landmarks started to move (proportion of sessions with landmark control failure: 515: 0/15; 576: 1/9; 637: 4/17; 638: 3/14; 692: 3/17).

4.2.9 Data analysis

Data from the two experiment computers were synchronized using the paired pulses, and all data were transformed into the same set of timestamps. For each triggered spike waveform, features such as peak, valley, and energy were used to sort spikes using a custom software program (WinClust; J. Knierim). Cluster boundaries were drawn manually on 2-dimensional projections of these features from two different electrodes of a tetrode. We mostly used maximum peak and energy as features of choice; however other features were used when they were required to isolate clusters from one another. Clusters were assigned isolation quality scores ranging from 1 (very well isolated) to 5 (poorly isolated) agnostic to their spatial firing properties. Only clusters rated 1-3 were used for all quantitative analyses in the main text.

To be included in the quantitative analyses, sessions were required to meet the following criteria: (1) sessions with landmark manipulation were completed and the rat was removed in the absence of landmarks, and (2) there were no major behavioral issues / long manual interventions during the session. For the 72/88 sessions meeting these criteria, spikes that occurred when the rat's movement speed was less than $5^\circ s^{-1}$ (about 5 cm/s) were removed. For each unit, the number of spikes fired when the rat occupied a 5° bin was divided by the time the rat spent in the bin to compute the firing rate. The firing rate was further smoothed with a Gaussian filter of standard deviation 4° . Single units were classified into putative pyramidal cells and putative interneurons by separating them based on firing rate, spike duration, and the autocorrelation function (Csicsvari, Hirase, et al., 1999). Only the

putative pyramidal cells were used for the main analyses, and the putative interneurons are described in Extended Data Fig. 4.11.

Spatial information scores were computed by binning and determining firing rates of spikes in both the lab and the landmark frames of reference, as described above. If the occupancy-corrected firing rate in bin i is λ_i , then information score is computed as:

$$\frac{1}{N} \sum_{i=0}^N \lambda_i \log_2 \frac{\lambda_i}{\lambda} \quad (4.1)$$

where N is the total number of bins, and λ is the mean firing rate (Skaggs et al., 1993)

4.2.10 Behavioral analysis

For each of the 4 epochs, the mean running speed (cm/s), the rate of pauses in running (defined as continuous epochs of 3 seconds or more where the velocity drops below 5 cm/s) (number/lap), the mean duration of each pause(s), the mean interpause temporal interval (s), and the mean interpause spatial interval (cm) were calculated. Interpause intervals were spatial or temporal differences between pause events, where the beginning and end of an epoch were also considered pauses. We first tested whether there were significant changes in these variables between Epochs 1 and 3 (i.e., before and after the gain ramp) and between Epochs 3 and 4 (i.e., before and after the landmarks were extinguished). Next, to address whether changes in behavior predicted the hippocampal gain change in Epoch 4, we ran 2 multiple regression analyses. First, we subtracted the values of each of the behavioral variables in

Epoch 1 from the values in Epoch 3. A multiple regression was run with the hippocampal gain (H) in Epoch 4 as the dependent variable and the five Epoch 3 - Epoch 1 behavioral measures, as well as the experimental gain (G) of Epoch 3, as the regressors. Second, we ran a multiple regression (similar to that above) with Epoch 4-Epoch 3 behavioral measures, as well as the experimental gain (G) of Epoch 3, as the regressors.

4.2.11 Estimation of hippocampal gain, H

A rat's position can be decoded from a population of simultaneously recorded place cells using established techniques (Zhang et al., 1998, Kloosterman et al., 2014, Brown et al., 1998). However, these techniques use an independent dataset to train an estimator and require that the spatial coding be unchanged during the testing phase. In our experiments, there were often remapping events during the gain manipulation epochs, as some units lost their firing fields and other units, which were previously silent, gain place fields on the track. This remapping was typically not all-or-none; rather, different place fields would appear or disappear at different times in the experiments (e.g. Figs. 4.2 c,e, 4.3 a,b). Although the new place fields changed their firing locations coherently with the existing place fields during the experimental manipulations, extensive remapping causes classic population decoding methods to become less accurate or to fail entirely. To solve this problem, we took advantage of the periodicity of firing of the place fields as the rats ran laps on the circular track to measure the spatial frequency of the population representation. This spatial frequency is insensitive to the specific place cells

that are active at any given moment and it thus forms the core of a spectral decoding technique robust to remapping (Extended Data Fig. ??).

The frequency estimate is termed the 'hippocampal gain', H . A typical place cell with a single field on a circular track exhibits one field/lap, and hence H should be $1/\text{lap}$ (Fig. 4.1e). As the visual landmarks are moved at an experimental gain G , the rat encounters each landmark every $1/G$ laps. If the place fields are controlled by landmarks, i.e., they fire every lap at the same location in the landmark reference frame, the value that we estimate for H should be similar to the value of G . For example, when $G = 1/2$, there should be one field every two laps, and thus $H = 1/2$ (Fig. 4.2 c,d), and for $G = 3$, there should be 3 firing fields per lap, and thus $H = 3$ (Fig. 4.2 e,f).

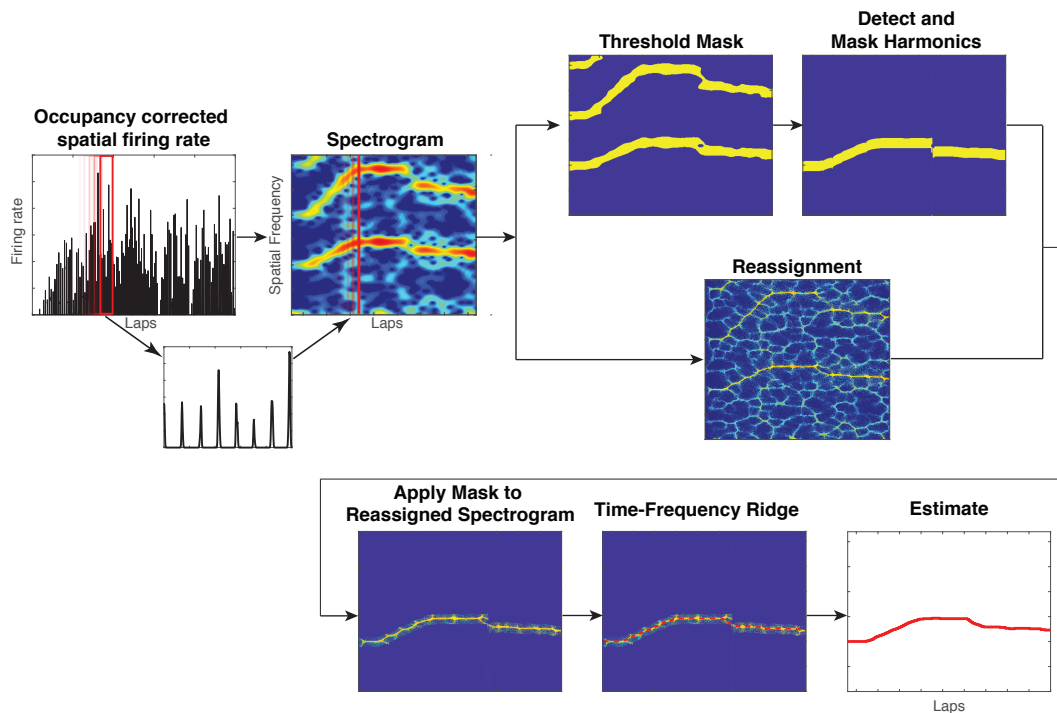


Figure 4.4: Flowchart showing the steps of the spectral gain estimator.

Hippocampal gain is first estimated independently for all well-isolated units (H_i for the i^{th} unit) that fire at least 50 spikes per session while the rat is running faster than $5^\circ s^{-1}$. The method of gain estimation is illustrated in Figure. 4.4 and is described in the following. The spatial spectrogram of the firing rate of each unit was computed at spatial frequencies (i.e., the frequency of repetition of its spatial firing pattern per physical lap) between 0.16/lap and 6/lap, using a sliding window of size 12 laps applied at increments of 5° . The spectrogram was further sharpened using the method of reassignment, which can be used when the input signal contains sparse periodic signal sources (Flandrin, Francois, and Chassande-Mottin, 2002). The original spectrogram was also thresholded to the mean + K times standard deviation (K between 1.1 and 2 based on visual inspection of the raw spectrogram) of its power at each spatial window; this thresholding was then applied to the sharpened spectrogram to improve the signal-to-noise ratio of the spatial frequency content.

The spectrogram can have substantial power in the harmonics of the fundamental frequency, requiring a method to reliably find the fundamental. The gain estimation algorithm identified peaks in the autocorrelation of the spectrogram at each spatial window. Since these peaks typically lie at the fundamental frequency and its harmonics, the fundamental frequency should be both the lowest peak and the difference between peaks. If the median of the difference between peaks was an integer multiple of the lowest peak, the lowest peak was considered the fundamental frequency, and all the power in the reassigned spectrogram further than 0.1 Hz from the fundamental

was set to zero (if not, the spectrogram was used as-is). This process was repeated for each spatial window. Finally, the maximum-energy trajectory from the reassigned spectrogram was extracted, and this trajectory formed the time-varying gain estimate for that particular unit.

In some cases a particular unit did not produce sufficient spiking activity to generate an estimate for a given window; entries for which there was no estimate were set to NaN in MATLAB for computational convenience. The hippocampal gain estimate for each window for the population (H) was calculated as the median H_i from all units under consideration. If there were no active units during a given window (all NaNs) then the value for H was set to NaN for that window.

4.2.12 Visualizing H

For each experimental session, H can be plotted as a function of angular displacement of the rat (e.g., Fig. 4.3 a,b, Extended Data Fig. 4.9 a,b). It is important to note that each estimate is correlated with neighboring estimates due to the 12-lap sliding window. Estimates that are 12 laps apart are calculated from independent data. The estimate at any given angular position is "non-causal" in the sense that it uses neural data from ± 6 laps centered around that angular position. This creates the illusion that H "anticipates" the extinguishing of landmarks (Fig. 4.3 a,b,f, Extended Data Fig. 4.10 a-e, Extended Data Fig. 4.11 a,b). Inspection of the raw spikes readily verifies that this is an artifact, but this artifact does not affect any of the interpretations in this paper.

4.2.13 Coherence score

In a session, if a unit, i , is part of a coherent population, its gain should equal the hippocampal gain, namely $H_i \approx H$. Thus for each 12-lap window we computed a coherence error $|1 - H_i/H|$ and defined the coherence score as the mean of this quantity over an entire session.

4.2.14 Landmark control ratio

In a session, if the hippocampal gain follows the experimental gain, we expect $H/G = 1$. Thus, H/G was computed at each overlapping 12-lap window for Epochs 1-3 and the landmark control ratio was defined as the average of this quantity over a session.

4.2.15 Analysis of drift

From each session with landmark control, we identified units which had a single, non-remapped firing field in the landmark frame during Epochs 1 - 3. The average landmark-relative firing rate maps of the unit were calculated separately for the duration of Epoch 1 (start of experiment, $G = 1$) and for the last 12 laps before the landmarks were turned off. The cross-correlation between these two firing rate maps was computed as the rate maps were rotated relative to each other. The landmark-relative angle lag corresponding to maximum correlation was considered to be the drift of the unit. For trials with multiple units with firing fields that did not remap during Epochs 1- 3, we took the mean drift over all units to be the drift for that session. In all, this analysis utilized 136 units from 55 days.

4.2.16 Analysis of recalibration

We chose sessions with landmark control and at least 12 laps run after the landmarks were turned off (Epoch 4). The recalibrated gain was selected as the value of H six laps after the landmarks were extinguished (lap 6 was the midpoint of the first 12-lap window that includes only data from Epoch 4). To examine the decay rate of recalibration, we chose sessions with landmark control and at least 24 laps run in Epoch 4. We compared the recalibrated gain at lap 6 with the value of H at lap 18 (the first point at which the 12-lap spectrogram windows do not overlap).

4.2.17 Histology

Once experimental sessions were complete, rats were transcardially perfused with 3.7% formalin. The brain was extracted and stored in 30% sucrose formalin solution until fully submerged, and sectioned coronally at 40 μ m intervals. The sections were mounted and stained with 0.1% cresyl violet, and each section was photographed. These images were used to identify tetrode tracks, based on the known tetrode bundle configuration. A depth reconstruction of the tetrode track was carried out for each recording session to identify the specific areas where the units were recorded.

4.2.18 Statistics

Parametric tests were used to determine statistical significance. Pearson product-moment correlations were used to test the linear relationship between variables. Paired, 2-sided t-tests were used to compare information scores in

the lab and landmark frames of reference, which assumes normality. Wilcoxon rank-sum tests were used to test differences in behavioral variables. To prevent sampling the same cells across days for this analysis, the experimental session with the greatest number of units was chosen for each rat and for each tetrode.

4.3 Extended data figures

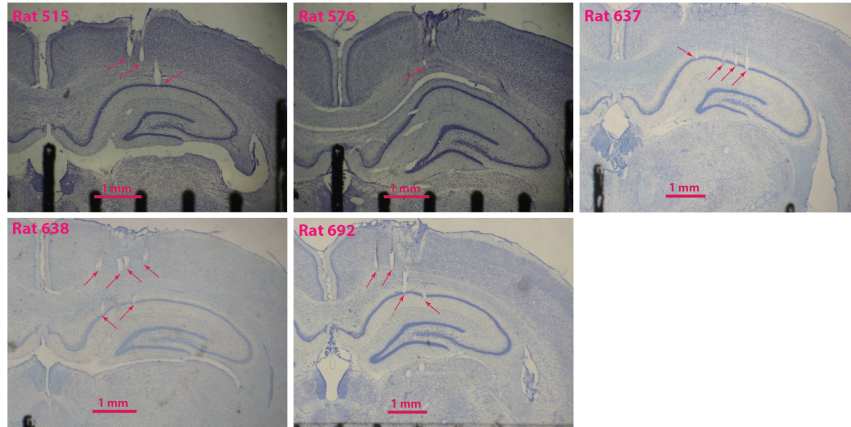


Figure 4.5: Representative histology. Coronal slices from the five rats used in this study. Arrows point to tetraode tracks in different stages of advancement towards CA1. Note that these are not always the termination of these tetrodes, simply one section along their tracks. In one animal (Rat 576), the histology was inconclusive due to poor fixation and slice quality; however, we determined that the tetrodes were correctly placed in CA1 by the medio-lateral placement of the bundle, tracks in the few sections that we could analyze, and features in the EEG signals observed during recording (e.g., sharp wave/ripples). In one animal, (Rat 638), two of the most medial tetrodes (not shown) appeared to record from the fasciola cinereum, rather than CA1.

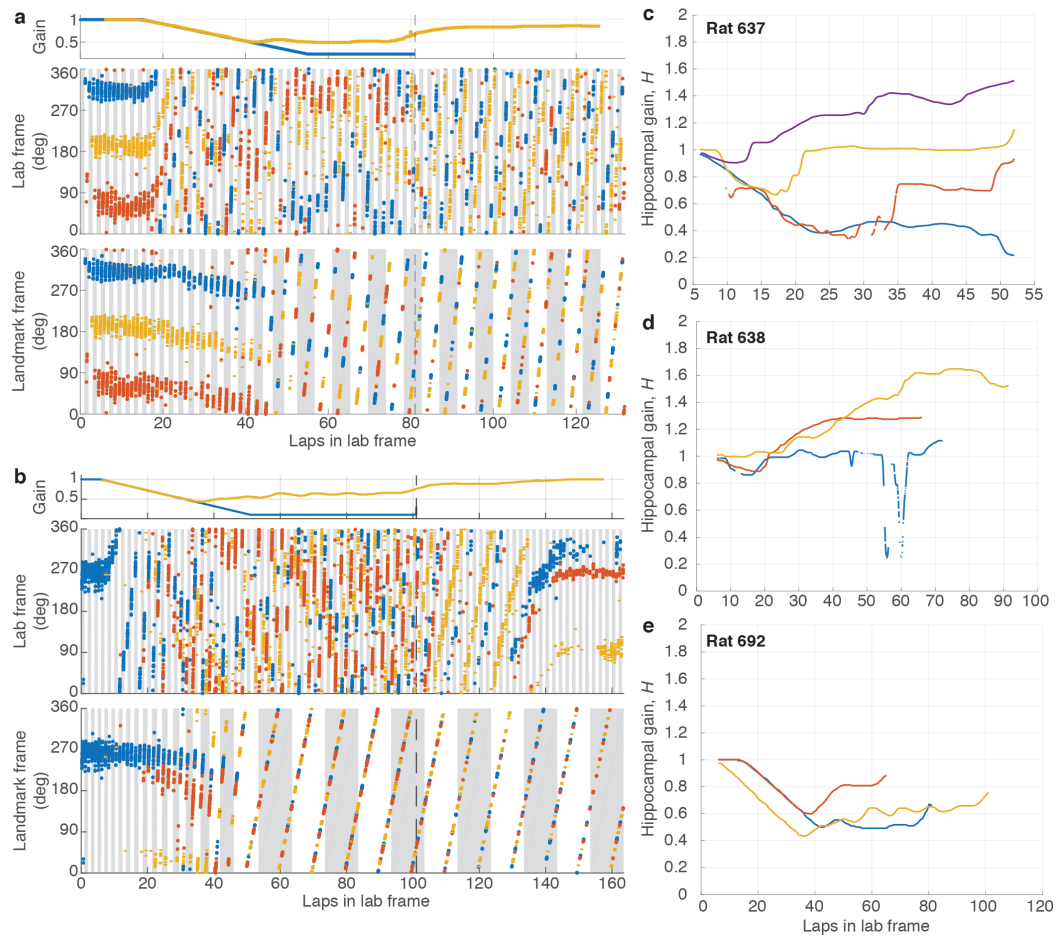


Figure 4.6: Examples of failure of landmark control. (a) (top) Experimental gain, G (blue), and hippocampal gain, H (yellow), for Epochs 1-3 of a session where G_{final} was 0.231. Note that the two curves overlap until \sim lap 40, when they start to diverge. (middle) Spikes from three putative pyramidal cells (colored dots) in the lab frame. Alternate gray and white bars indicate laps in the lab frame. (bottom) The same spikes in the landmark frame. At the point of landmark control failure, the place cells stop firing at a particular location in the landmark frame, and instead start drifting in both lab and landmark frames. Alternating gray and white bars indicate laps in the landmark frame. (b) Second example, from a different animal, for a session where G_{final} was 0.1 (same format as (a)). (c-e) Trajectory of hippocampal gain, H , for three rats for all sessions where landmark control failed. The hippocampal gain generally starts near 1 and then diverges from the experimental gain trajectory (not shown) during the session.



Figure 4.7

Figure 4.7 (previous page): Gain dynamics during each experiment. Each plot represents data from a single experiment. The x-axis is the laps that the rat ran in the lab frame (on the table) and the y-axis is gain. The black scale bar in each plot indicates 10 laps. The applied experimental gain (blue) is plotted with the hippocampal gain estimate (red). The ramp rate, length of epochs and final experimental gain for each session can be observed from the curves. An asterisk indicates experiments with loss of landmark control (gain ratio greater than 1.1; see Fig. 4.2 h). In the other plots, the blue and red curves overlap indicating control of landmarks over the place fields. Number of units that passed acceptance criteria (Methods) in each session is indicated in the bottom right hand corner of each plot.

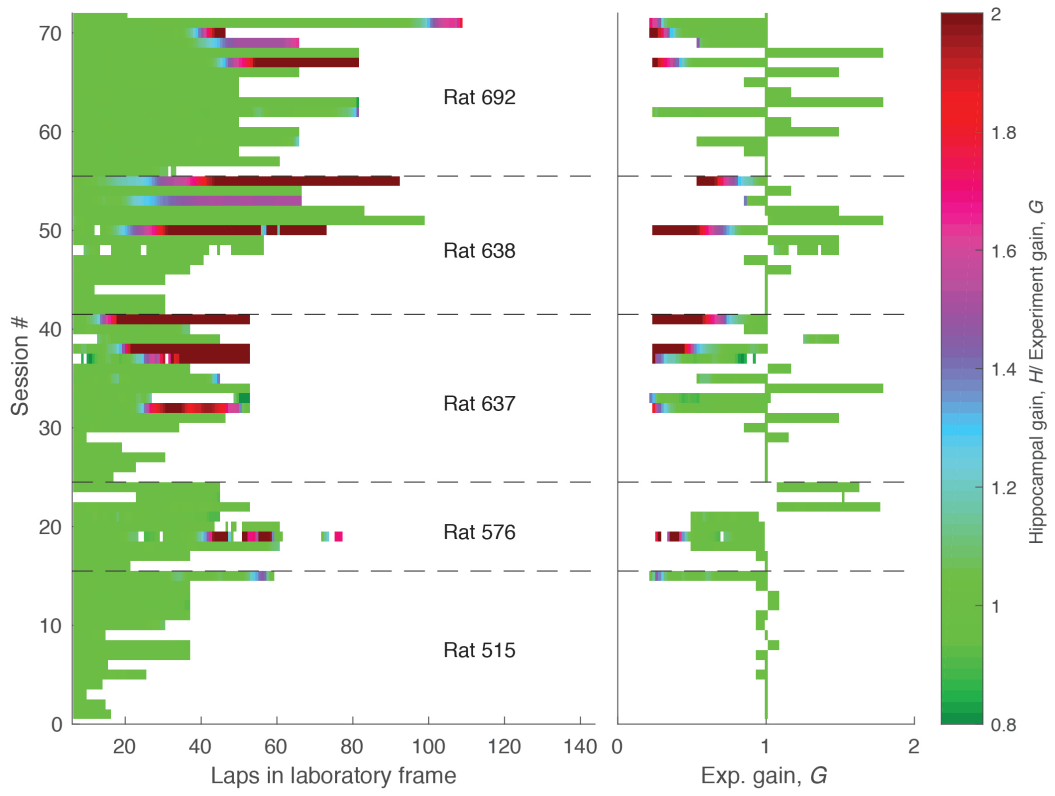


Figure 4.8

Figure 4.8 (previous page): Summary of dataset. Each row indicates one of the 72 sessions composing the dataset during the period when the landmarks were on. In the left plot, the x-axis is laps in the lab frame. In the right plot the x-axis is experimental gain, G . The sessions are chronologically ordered (bottom to top). Sessions from different animals are separated by dashed lines. In all rats, we typically performed smaller manipulations in G first, since initial landmark failure tended to occur at larger manipulations of G . Once landmark control failed, it tended to fail more frequently. The color represents the ratio between hippocampal and experimental gains (H/G , color bar, right). Green ($H/G = 1$) indicates landmark control. Four of the rats (576, 637, 638, 692) experienced landmark failure (red portions of trials). Failures only happened when the G was less than one (i.e., the landmarks moved in the same direction as the rat) and generally occurred at low values of G (less than 0.5) and after rats had experienced multiple gain manipulation sessions over days. The asymmetry in landmark control between $G < 1$ and $G > 1$ is similar to a study of medial entorhinal cortex by Campbell and colleagues (Campbell et al., 2018). In this study, mice ran on a VR linear track controlled by a stationary treadmill, and the authors manipulated the gain factor between distance traveled on the treadmill versus the VR track. Grid cells showed asymmetric responses to increases versus decreases of the gain. Gain increases (i.e., $G > 1$) caused phase shifts in the spatial firing patterns but gain decreases (i.e., $G < 1$) caused changes in the spatial scales. These results were elegantly explained by a model of how grid cells respond to conflicts between self-motion and landmark cues. Although this paper did not address the issues of path integration gain recalibration as in the current study, its results may provide a causal explanation for the asymmetric responses of place cells to the landmark manipulations seen in the present study.

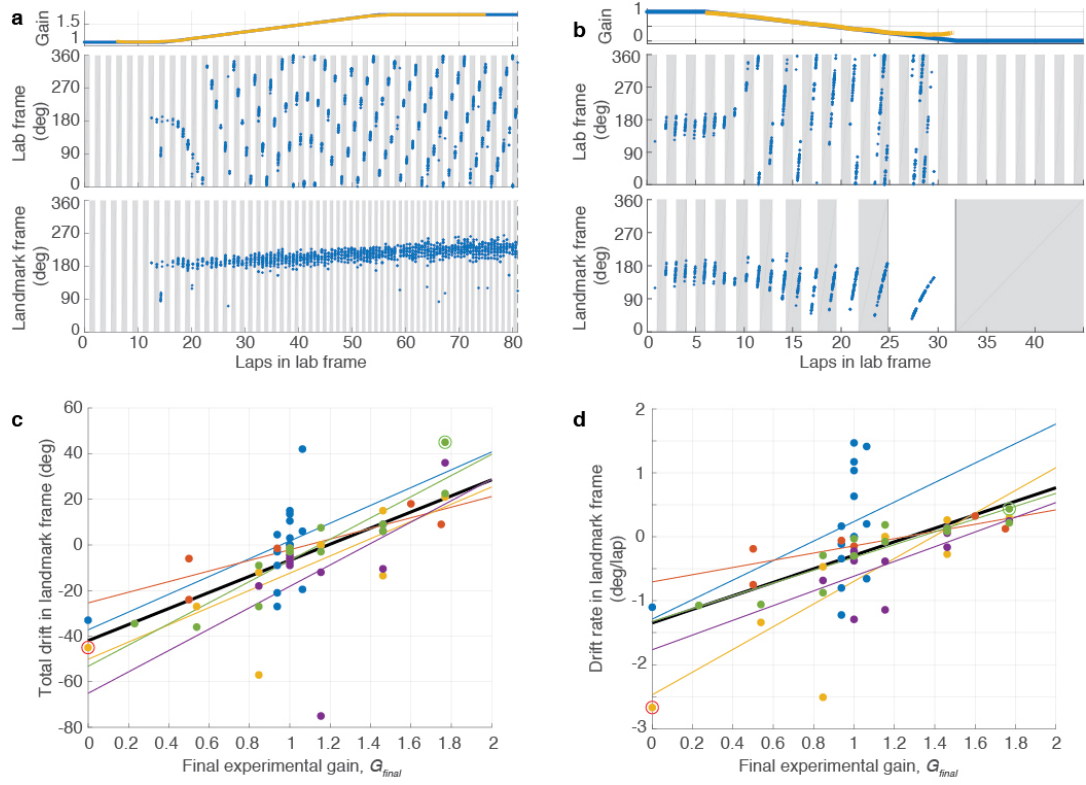


Figure 4.9

Figure 4.9 (previous page): Slow drift of place fields against landmarks. (a) Example of positive drift. (top) Experimental gain, G (blue), and hippocampal gain, H (yellow), for Epochs 1-3 of a session in which G_{final} was 1.769. There is no H (yellow) in the first or last 6 laps due to the 12-lap sliding window. (middle) Spikes from one putative pyramidal cell (blue dots) in the lab frame. Figure format is the same as in Figure 2. (bottom) The same spikes in the landmark frame. The unit was silent for the first 12 laps but developed a strong place field in the landmark frame that slowly drifted in the same direction as the animal's movement over the course of the session. (b) Example of negative drift from a session in which the G_{final} was 0. In the landmark frame, the slow drift was in the direction opposite to the animal's movement direction. Note that the unit was completely silent in Epoch 3, because the rat was not in the place field of the unit as G reached 0. (c) Drift over the entire session vs. G_{final} . Each point represents an experimental session. Linear fits are shown for each individual rat (colored lines) and for the combined data (black line; $n = 55$ sessions, Pearson's $r_{53} = 0.64$, $p = 1.5 \times 10^{-7}$). The two example sessions of (a) and (b) are shown with the circled markers. (d) Drift rate vs. G_{final} . Although the magnitude of drift is correlated with the final experimental gain (G_{final}), as shown in (c), a confound is present because the ramp duration in Epoch 2 depends on the value of G_{final} (e.g., for $G > 1$, the larger G_{final} is, the more laps required to ramp G up to that value). It is thus possible that the correlation between the total drift and G_{final} is due to the differences in Epoch 2 duration (and, in some experiments, Epoch 3 duration) rather than due to different rates of drift that depend on G . To control for the effect of trial duration, we calculated drift rate by dividing the total drift by the total number of laps in the landmark frame over which the drift was computed. Linear fits are shown for each individual rat (colored lines) and for the combined data (black line; $n = 55$ sessions, Pearson's $r_{53} = 0.54$, $p = 1.9 \times 10^{-5}$). The two example sessions of (a) and (b) are shown with the circled markers. These results show that the drift rate was related to the value of G_{final} .

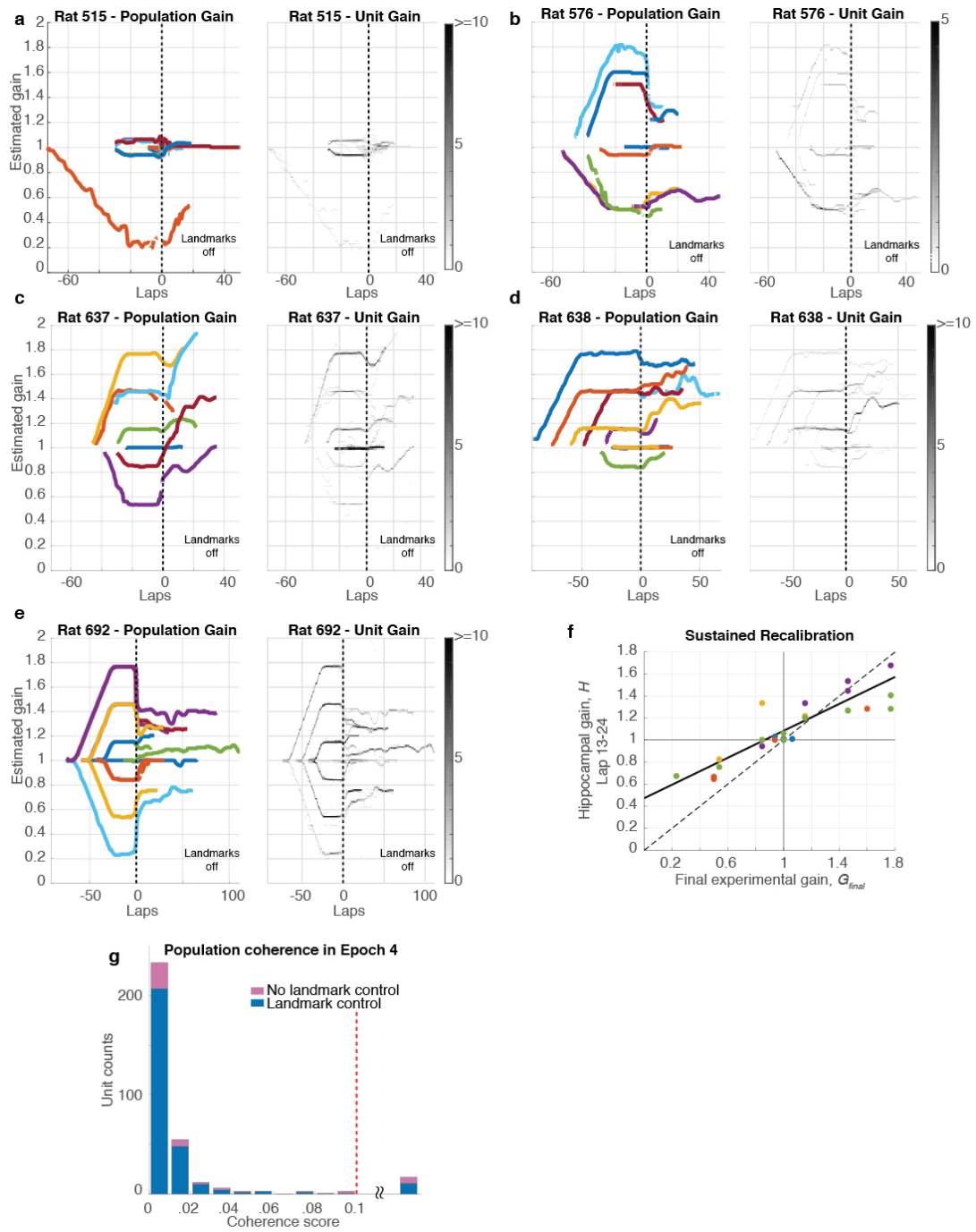


Figure 4.10

Figure 4.10 (previous page): Dynamics of recalibration. (a-e) The complete hippocampal gain (H) dynamics for all 5 rats for trials that exhibited landmark control. (The gain dynamics for Rat 692 is also shown in the main text, Fig. 4.3 e.) In the left panels for each rat (color), H is plotted as a function of laps run in the lab frame. Sessions are aligned to the instant when the landmarks were turned off (denoted as lap 0). In the presence of landmarks, (before lap 0), the hippocampal gain tracked the experimental gain profiles during a given session (not shown). After the landmarks turned off, the traces largely maintained their recalibrated gain, while also showing some variable drift across experiments. Note that for each rat, for experiments in which $G = 1$ (i.e., the landmarks did not move), the value of H was close to 1 when the landmarks were extinguished. The right panels for each rat show the gain trajectories of all the units in the dataset. The gray scale represents the number of active cells with gains falling in a given bin (bin size is 5° for laps axis and 0.01 for gain axis). These graphs demonstrate the high degree of coherence of the hippocampal population, as almost all cells shared the same gain with minimal deviation. The light-colored lines that occasionally deviate from the main trajectories arise from the small number of cells with poor spatial tuning or from cells that remapped. In the latter case, because our spectral gain analysis used a window of 12 laps, these remapped cells continued to show artefactual values for the limited number of laps that fall in this window but during which the cell was silent. As can be seen, these exceptions had negligible influence on the median population gain values. (f) Sustained recalibration. Comparison of G_{final} (x-axis) and H computed using laps 13-24 (i.e., the value of H at lap 18) after the landmarks were turned off (y-axis). Sessions for each rat are plotted in different colors, along with the perfect recalibration line (dashed line, black) and a linear fit (solid line, black; $n = 27$ sessions, Pearson's $r_{25} = 0.85$, $p = 2.04 \times 10^{-8}$). The number of data points is lower than in Fig. 4.3 c because some experiments ended prior to lap 24. (g) Histogram of coherence scores (same format as Fig. 4.2 g) for units firing during Epoch 4 (landmarks off). The shape of the histogram is very similar to Fig. 4.2g. Almost all units had a coherence score below 0.1, indicating that the place fields acted as a coherent population in sessions with (blue) and without (pink) landmark control in Epochs 1-3, even after landmarks were turned off. Units with coherence score above 0.1 (range 0.11 - 0.41) were combined in a single bin (17/336 units).

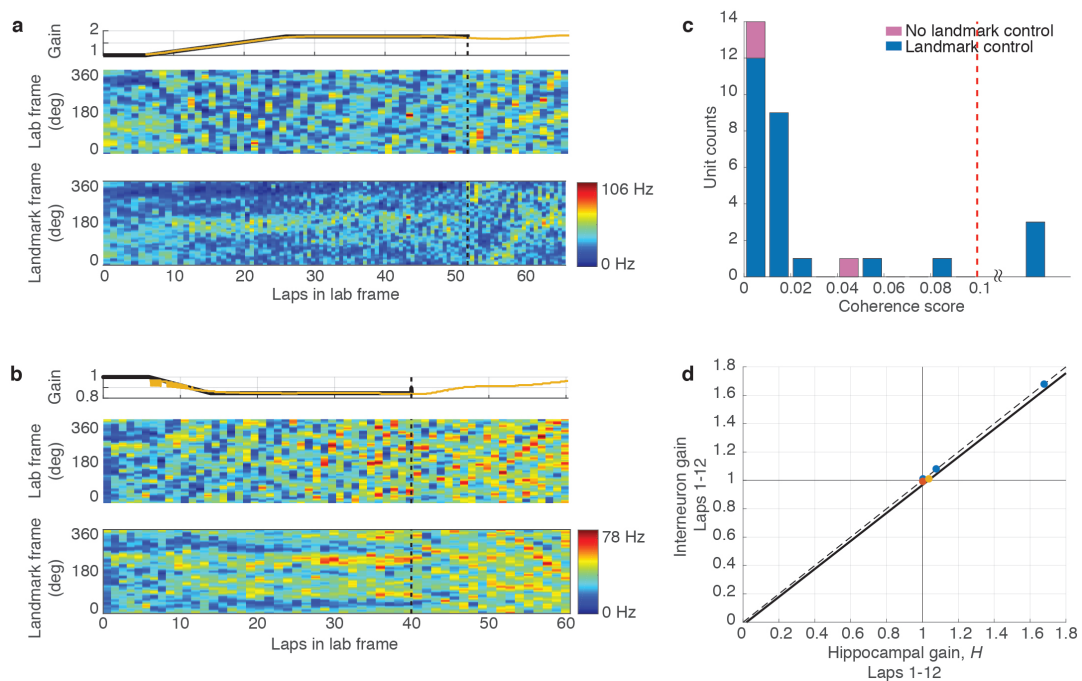


Figure 4.11: Path integration gain recalibration is also demonstrated by hippocampal interneurons. (a) (top) Experimental gain, G (black) and hippocampal gain, H (yellow) for Epochs 1-4 of a session where the G_{final} was 1.769. H was computed as usual from putative pyramidal cells (Methods, Estimation of Hippocampal Gain). In Epoch 4, landmarks are off and hence there is no G . (middle) Spatiotemporal rate map of one putative interneuron in the lab frame. Due to the high firing rate of interneurons, rate maps are more illustrative than the spike plots used in place cell examples. Each horizontal bin represents a lap in the lab frame, similar to the alternating gray and white vertical bands in the place cell examples (e.g. Fig. 4.2 a,c,e). Each vertical bin spans 3° in the lab frame. (bottom) Rate map of the same unit in the landmark frame. Each horizontal bin represents a lap in landmark frame, and each vertical band spans 3° in landmark frame. Note that the firing pattern is preserved across laps until Epoch 4, when the landmarks turn off. (b) Example of putative interneuron in a session where G_{final} was 0.846. Same format as (a). (c) Histogram of coherence score between interneurons and putative pyramidal cells, as in Fig. 4.2g. The score for each putative interneuron is computed as the mean value of $|1 - I/H|$ over the entire session, where I is the spectral gain estimated from the interneuron, and H is the hippocampal gain computed as usual from putative pyramidal cells. Units with coherence score above 0.1 (range 0.15-0.24) were combined in a single bin. (d) H estimated using the first 12 laps after landmarks were turned off, using the median of estimates from putative pyramidal cells compared to the median of estimates from putative interneurons. There are only 5 data points since these are the subset of sessions in Fig. 4.3 c with simultaneously recorded putative interneurons and place cells.

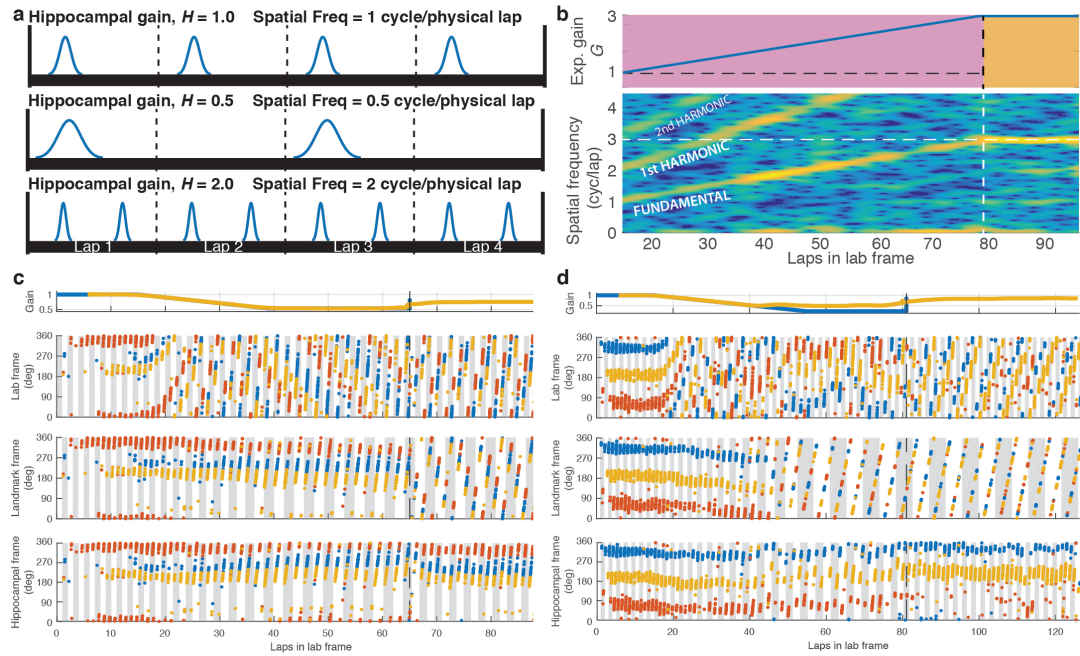


Figure 4.12: Illustration of spectral decoding scheme. In the dome, as visual landmarks are presented and moved at an experimental gain G , the rat encounters a particular landmark every $1/G$ laps (the spatial period). If the place fields fire at the same location in the landmark reference frame, the cell's firing rate exhibits a spatial frequency of G fields/lap. (a) Illustration of place field firing for three values of hippocampal gain, H . (b) Data from a session in which G was gradually increased from 1 to 3 (top) as in Epoch 2 of our experiments. The spectrogram of one unit is shown at the bottom, with the color denoting the power at a given position and frequency. A clear set of peaks in the spectrogram emerges at spatial frequencies corresponding to the experimental gain and at its harmonics. We use a custom algorithm to trace these peaks (Methods, Estimation of Hippocampal gain) and estimate the gain for each unit. The hippocampal gain, H , is estimated by taking the median spatial frequency across all isolated units (H_i for the i^{th} unit) for a given session. Note that this method does not require that cells display single, sharply tuned place fields, as it works for cells with multiple fields as well as for interneurons (Extended Data Fig. 4.11). (c) Reproduction of Fig. 4.3 b, along with addition panel at the bottom that represents the same spikes in the "hippocampal frame;" that is, the spikes were plotted in the frame of the landmarks as if they were rotating at the calculated gain of the place cell map (the hippocampal gain, H). The shaded vertical bars denote each lap in the hippocampal frame. Fields from all three units are horizontally aligned in this panel during all epochs, indicating that the spectral decoding technique was successful and that the place fields acted as a coherent spatial representation within the hippocampal frame. (d) Reproduction of Extended Data Fig. 4.2a, along with additional hippocampal gain panel at bottom. In this dataset, it can be seen that even after 'failure' of landmark control of place fields, the fields are still coherently firing at the same hippocampal gain, which we are able to estimate using spectral decoding.

	Mean vel (°/sec)	Pauses/lap	Pause Duration (s)	Interpause Interval (s)	Interpause Distance (°)	G_{final}
<i>Mean (S.E.M.)</i>						
Epoch 1	24.6 (0.7)	0.9 (0.2)	8.8 (1.0)	55.8 (8.2)	887 (136)	--
Epoch 2	25.2 (0.9)	1.0 (0.1)	6.5 (0.5)	61.8 (18.0)	1119 (399)	--
Epoch 3	25.0 (1.0)	1.5 (0.2)	8.8 (1.0)	26.3 (3.5)	461 (79)	--
Epoch 4	24.2 (1.0)	1.5 (0.3)	9.2 (0.8)	34.9 (9.4)	531 (125)	--
Epochs 3-1	0.4 (0.5)	*0.5 (0.2)	0 (1.5)	*-29.6 (7.9)	*-426 (121)	--
Epochs 4-3	-0.8 (0.4)	0.1 (0.2)	0.3 (1.3)	8.6 (9.8)	69 (134)	--
<i>Multiple regression</i>						
<u>Epoch 4 – Epoch 3</u>						
β	-0.01	0	0	0	0	0.65
S.E.	0.01	0.02	0	0	0	0.05
<u>Epoch 3 – Epoch 1</u>						
β	0.01	-0.01	0.01	0	0	0.66
S.E.	0.01	0.03	0	0	0	0.05

Table 4.1: Results of behavioral analyses Two-sided Wilcoxon Signed Rank tests were performed on the differences between values in Epochs 3 and 1 and Epochs 4 and 3 with null hypothesis that the difference = 0. Pauses/lap (n = 37 sessions; p = 0.035); Interpause Interval (n = 37 sessions; p = 0.001); Interpause Distance (n = 37 sessions; p = 0.003). All other tests for Epochs 3-1 and Epochs 4-3 were not significant

4.4 Contributions

The contributors are Ravikrishnan P. Jayakumar (R.P.J), Manu S. Madhav (M.S.M), Francesco Savelli (F.S.), Hugh T. Blair (H.T.B.), Noah J. Cowan N.J.C.), James J. Knierim (J.J.K.).

These authors contributed equally: Ravikrishnan P. Jayakumar, Manu S. Madhav.

These authors jointly supervised this work: Noah J. Cowan, James J. Knierim.

J.J.K., N.J.C. and H.T.B. conceived and all authors designed the study. J.J.K. and N.J.C. advised on all aspects of the experiments and analysis. F.S. made key contributions to the analysis and interpretation of the data and provided supervision over data acquisition and analysis. R.P.J. and M.S.M. designed and constructed the apparatus with R.P.Js majority contribution being towards the hardware design and construction and M.S.Ms being towards the experiment control software design. R.P.J built the hyperdrives. M.S.M performed the surgeries with R.P.J assisting. R.P.J and M.S.M collaboratively trained the animals and performed the experiments. M.S.M did the cluster cutting of spikes. R.P.J. designed the spectral gain estimation algorithm. R.P.J and M.S.M analysed the data.

Chapter 5

Further developments to spectral gain estimator

For this chapter, I performed the majority of the analysis and generation of figures in this chapter. I wrote the text and the work has not yet been published elsewhere. External contributions are detailed at the end of this chapter

The spectral gain decoding algorithm is a robust and versatile method that allows one to get an output of the rat's internal perception of velocity (or dilation of space, from a different point of view) and, in conjunction with the Dome experiment apparatus, enables the pursuit of many new avenues of research and data analyses. The decoding can be done on a cell by cell basis, being highly insensitive to rate and position remapping. Getting an estimate from each cell allows subsequent analysis on the homogeneity or heterogeneity of the population response, if any.

This chapter is a record of subsequent developments with this algorithm. Sections [5.1.1](#) and [5.1.2](#) describe improvements to the gain estimation itself while [5.2.1](#) and [5.2.2](#) talks about two new applications of this algorithm beyond

its use on clustered spike data.

5.1 Improvements to the algorithm

5.1.1 Adaptive windowing

The version of the decoder used in the analysis of the results presented in Chapter 4 had opportunities for improvement. This can be seen in Figure 4.12 c,d where the spikes are plotted in the hippocampal frame of reference. While the estimate is able to correct the field movement, almost completely putting it into a stable frame of reference, there are still slow oscillations and drift in the place fields from lap to lap. Because the hippocampal frame is defined by estimating spike position by integrating the "internal velocity" signal as read in by the decoder, slight errors would accumulate leading to drift of the fields.

One of the factors contributing to inaccuracies in estimation was that the size of the sliding lap window was set to be a constant size regardless of the actual spatial frequency content. Thus, if the sliding spatial window does not encompass a natural number of cycles of the spatially periodic spike firing rate signal, spectral leakage can occur due to the signal getting cut off. The algorithm of the spectral gain decoder was modified to reduce this leakage. The modified algorithm works in two stages. The first stage is the same as that described in Section 4.2.11 where estimation is done with a constant sliding spatial window size and an estimate of the spatial frequency is obtained. In the second stage, this spatial frequency estimate is used to adaptively change the window size at every step to one that minimizes the spectral leakage.

This is done by first defining the position of the spikes in the estimated

hippocampal frame of reference as defined by the spatial frequency trajectory obtained from the first step. As shown in Figure 4.12 c,d bottom panels, this brings the place fields to a frame of reference in which they are almost completely stable. The fields of a place cell with a single place field fire at the same location lap after lap. Thus the spatial frequency of the spikes in this frame of reference would be close to 1.

The occupancy-corrected spatial firing rate is computed for the spikes in this estimated hippocampal frame of reference. The spatial frequency of this firing rate curve is estimated using the same spectral gain decoder algorithm used in the first step with a constant window size of a natural number lap width. While the window size is constant in the estimated hippocampal frame, it is effectively resizing as a function of the estimated spatial frequency in the lab frame. As an example, if the spatial frequency estimated in lab frame at a spatial step is h , then the sliding spatial window used in step 2 be of constant width c laps will effectively be of width $\frac{c}{h}$ in the lab frame. While it is not perfect, this method of adaptive windowing can yield improvements in the frequency estimation especially in the lower frequency range where the spectral leakage issue is more severe. This is because, for a given window size, the number of cycles of a periodic signal goes down with the frequency and the clipped cycle of the signal will cause relatively more distortion and spectral leakage.

5.1.2 Enhancing gain estimation using place field detection

Setting the size of the sliding window for a spectrogram inherently has trade-offs between gaining frequency resolution for larger window sizes and gaining temporal resolution – or spatial resolution in this particular application – for smaller window sizes. But in a lot of cases, depending on the specifics of the problem at hand, there are ways to circumvent these limitations. One such step discussed in Section 4.2.11 was the use of the method of reassignment, which assumes that in a local frequency-space window of a spectrogram, there is only one frequency source that is contributing to the power in that window, allowing the concentration of power to the center of gravity as determined by the phase information. This allows compensation of blurring of the spectral content to an extent. A two stage process was described in the Adaptive windowing section above. I describe a third stage below which will give as its output a close-to-perfect estimate of the underlying spatial frequency/gain.

The third stage assumes that there is a hippocampal frame of reference where the place fields are in a stable position every instance that the rat visits it and the spatial frequency is ~ 1 . The enhanced two stage gain estimation from the two stage process described is able to plot the spikes in a frame of reference that is a small “delta” away from the actual hippocampal frame, with the discrepancy being due to slow oscillations and the drift. The third stage involves detecting the individual place fields in the hippocampal frame of reference as defined by the previous step of the decoder and then aligning them such that fields are in a stable position. The amount by which the individual fields needs to be shifted to do this is almost exactly the “delta”

difference between decoder gain estimate and the actual hippocampal frame. This field correction signal can be used to further refine the gain estimate signal resulting in it reflecting the actual gain dynamics almost perfectly.

The process by which this is done is to first plot the spikes in the hippocampal frame of reference as estimated by the decoder. Next, assuming that place cell spikes are basically samples from an underlying firing probability density function reflecting its spatial tuning, a kernel function is used to estimate the firing rate curve in this estimated hippocampal space in unwrapped angle. The peaks in this spike firing curve are detected. If two peaks are too close together ($< 10^\circ$), then the higher peak is kept and the smaller one is removed from the list of peaks. Then, using this list of peaks as being the point of maximum firing rate of a field, individual passes of place fields are defined as contiguous segments around each peak where the firing rate is above 10% (heuristically determined) of the maximum firing rate. Minimum and maximum field size limits for individual passes of the place field are set to filter these merged fields.

If we had place cells with a single stable firing field without positional remapping over the course of the experiment, the field passes detected at this stage would be sufficient to find the "delta" gain difference. However, place cells can have more than one field and undergo position remapping. And exacerbating this is the fact that the process of manipulating the experiment gain seems to increase the probability of remapping. So the final step in this stage is to cluster together the detected field passes i.e. the times the animal passes through a place field to separate out remapped fields or multiple fields

which is done as follows. For a given field pass, field passes in the adjacent 4 laps are defined to be in proximity to it if 1) the centers (defined as the geometric midpoint of the field pass; this is not the point of peak firing rate of the field pass) of the adjacent field passes are within the field limits of the selected field pass in wrapped hippocampal angle space and 2) if the centers of the adjacent field passes are within 15 degrees of the selected field pass in wrapped hippocampal angle space. If, for a selected field pass, the number of adjacent field passes are less than 3 or if the number of spikes in the selected pass is less than 4, this field pass is deleted as it is most likely spurious spikes that do not maintain a stable spatial tuning for a significant amount of time. The clustered field passes that pass the above criteria is defined to be a field. These clustered field passes within a field can then be aligned to correct for any slow oscillations or drift and the amount by which they are aligned provides the correction curve for the estimated gain curve.

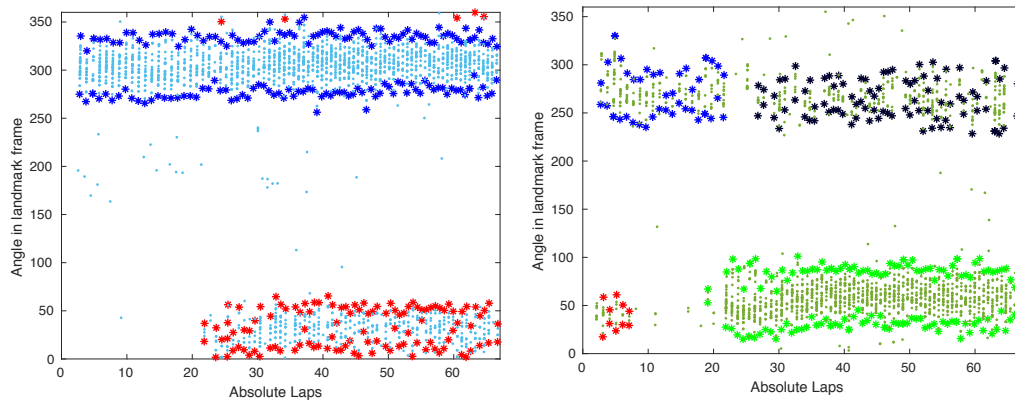


Figure 5.1: Two examples of place field detection in the presence of multiple place fields and remapping. The data is from sessions with landmark control. Laps in lab frame are shown on the x axis and the animal’s angle in landmark frame is shown on the y-axis. Each dot is a spike and dots of a particular color represent spikes from a putative neuron. Asterisks show the limits of the detected fields. Asterisks defining the place fields of a place cell maintain a particular color until a remapping event.

5.2 New applications of the algorithm

5.2.1 Decoding on unsorted spikes

The decoder was originally used to estimate the gain of a sorted cluster of spikes which putatively belong to an individual neuron. If these cells were place cells, the spatial tuning would be fairly sharp and well-defined. However, as was shown in Figure 4.11, the decoder is able to estimate the spatial frequency from cells with much more diffuse spatial tuning like those of an interneuron. This result, supported by the fact that a coherent population response was observed in every gain manipulation experiment, motivated a look at decoding gain from unsorted spikes from a tetrode. Presumably, for hippocampus, a large majority of the recorded cells would be place cells. The spatial tuning of the superposition of the spatial firing of all of these cells with

more or less well defined spatial tuning would result in a more diffuse spatial tuning but nevertheless, one which still has the same spatial frequency as the constituent spatially tuned cells. The spectral decoder will fail if the spatial tuning gets diffuse enough to fall below the noise threshold or if the spatial tuning is too flat. The latter case is unlikely even if the cells being recorded on a tetrode had a uniform distribution of place fields over the track – the spatial distribution of all the (velocity filtered) spikes would also need to have an uniform distribution. The spectral gain decoder was run on velocity filtered unsorted spikes from a tetrode and the hippocampal gain was estimated as the median of the gain estimates from individual tetrodes rather than as the median from individual sorted clusters. As evident from the error measures shown in Fig. 5.2 c , the gain estimation from unsorted spikes is almost as good as the gain estimation from sorted spikes.

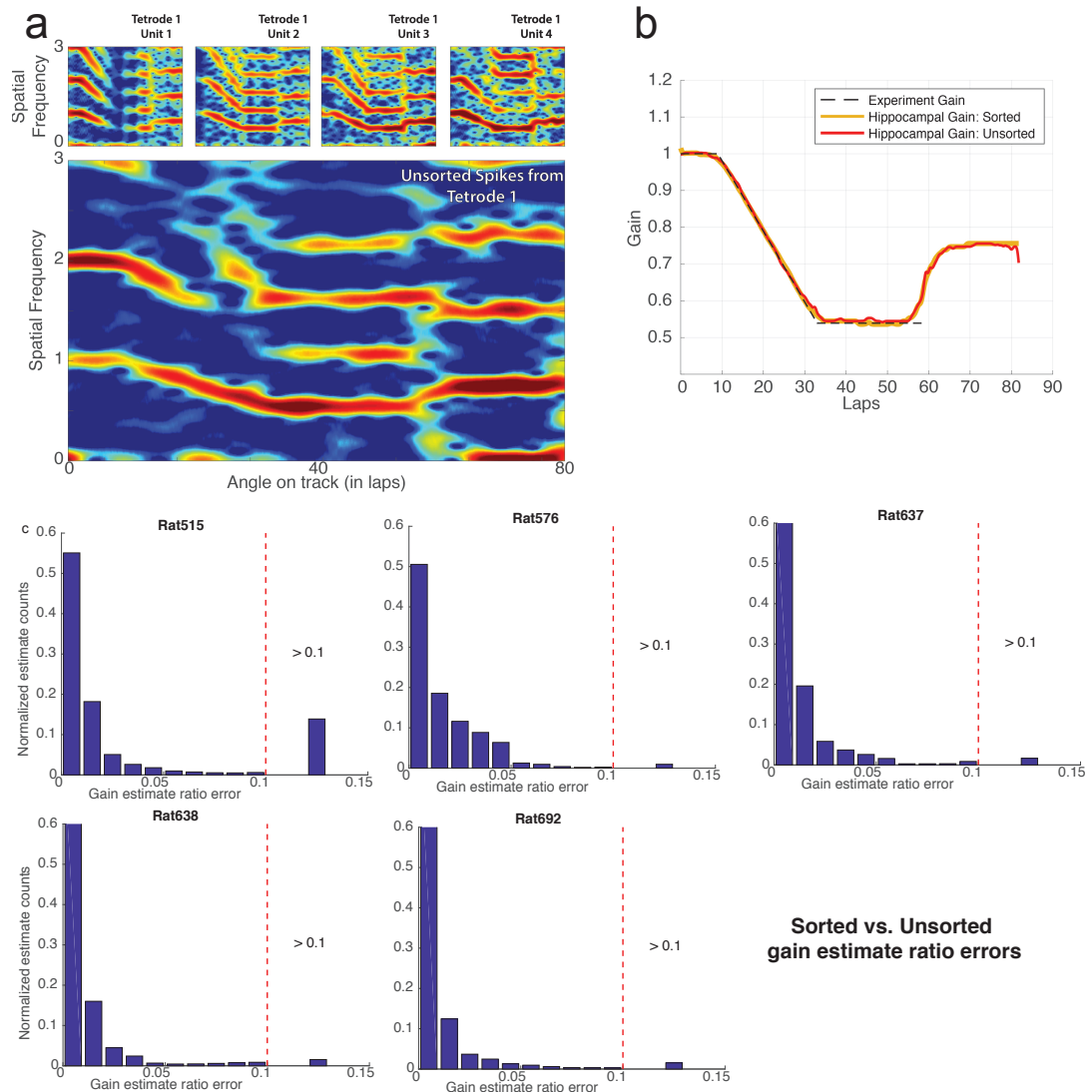


Figure 5.2: Unsorted decoding. The top left panel shows the spatial frequency spectrogram from a gain manipulation experiment being very similar when using sorted clusters or when using unsorted spikes from a tetrode. The right panel shows that an example of hippocampal gain estimation using unsorted spikes performs at the same level as that from sorted spikes. The histograms in the bottom row show the error between the gain as estimated when using sorted spikes versus unsorted spikes. Each panel uses data from a single rat.

While these error measures are very good, there are potential failure points to this approach. First would be the case where we have the "fortunate" situation of getting a large number of cells on a tetrode that happen to tile the space and have firing rates such that the superposed tuning curve is too diffuse and close to a flat line. In this case, the spectral power at the spatial frequency of this spatial tuning curve will be low and can be drowned out by spectral noise introduced by stochastic firing of neurons. The second would be a failure of the assumption that the population response is coherent. If there were sub-populations with different responses, it might yield a noisy gain estimate signal. Or worse, if spatial firing rate curve of one of the sub-populations dominates the rest, the output of the spectral decoder would be the gain of this dominant sub-population, masking out the existence of sub-populations.

5.2.2 Online gain estimation from unsorted spikes

The previous section discussed gain decoding from unsorted spikes from a tetrode. This is exactly the format of the incoming data while an experiment is running allowing for gain decoding from the data as soon as it comes in during an experiment.

The gain decoding step itself was trivial as it was a straightforward plugin of the unsorted spike based gain decoding algorithm. The hurdle in the implementation of online gain decoding lay in the preparation of the incoming data for use by the decoder with the primary challenge being that of timestamp synchronization. Previously, there were two computers involved in collecting

experiment data. In one, neural data was collected and timestamped according to the clock on the Neuralynx system. In the other, experiment data such as the animal's angular position, visual scene definition and manipulation, feeding, video refresh, etc were recorded and timestamped by the ROS master using the clock of that computer. The neural data would be synchronized with the rest of the data using the process described in Chapter 3, where a pseudo-random signal, sent from the ROS computer to the Neuralynx's Digital Lynx box, would be used to estimate the offsets and relative drifts between the clocks and bring the timestamps of all the data to a common frame of reference.

For online decoding, this step of synchronizing the neural data to the ROS data still holds true. But the process of online decoding now uses ROS nodes running on three different computers. There is now a ROS node on the computer (PC1) which does the neural data collection that converts the Neuralynx's timestamp to the ROS timestamp as determined by the local instance of the ROS Master node using PC1's clock. PC2, which also does the experiment control, collects data on the animal's position and the local instance of the ROS Master node timestamps it using PC2's clock. PC1 and PC2 pass their neural and position data respectively to PC3 at frequent and regular time intervals. PC3 interpolates the position and velocity data of the animal to the time of each spike and uses this to calculate the velocity filtered and occupancy corrected spatial firing rate curve. This firing rate curve is the input to a MATLAB instance that is running the spectral gain estimation that estimates the gain as soon as it comes in.

The complication in synchronization arises due to the fact that the ROS

Masters running on each of these computers timestamps data according to the local clocks. These clocks could be offset and drifting relative to each other and spikes could be assigned the wrong position and velocity. This can lead to spurious spikes being included or good spikes being rejected at the point of velocity thresholding. This cause of error and also the potential misassignment of position to a spike can cause distortions in the occupancy corrected spatial firing rate curve which in turn could lead to erroneous estimates of the hippocampal gain. To avoid this, a Network Time Protocol (NTP) was setup on all three computers and setup such that the clocks of PC1 and PC3 synchronizes with the clock of PC2 every 15 minutes.

There are certain steps in the spectral gain estimation that require filtering the data, such as the velocity measurements or the computed firing rate. Filtering can introduce edge effects at the very beginning and end of the stream of data. When the gain is decoded offline, the edges of the data are at the beginning and end of the experiment session, thus minimizing the edge effects to just a few instances. When decoding online, more care has to be taken. A buffer of data is built up to span a spatial window size that's bigger than the sliding window used by the gain estimator. The data within this buffer window is filtered and the gain estimation is done on a window that is centered in the buffer window such that it is unlikely that the data distorted by edge effects would be included.

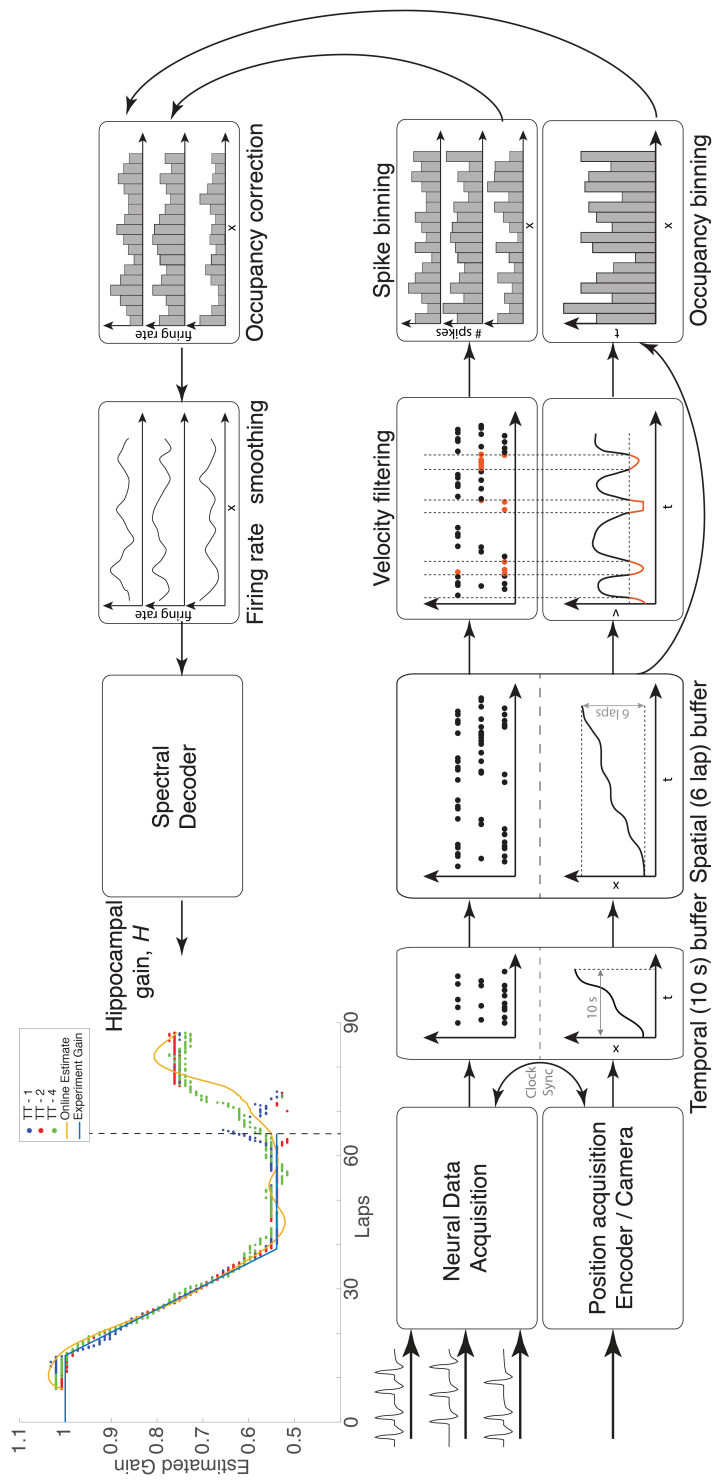


Figure 5.3

Figure 5.3 (previous page): (A) Example of online gain estimation. The data is from a session with landmark control over the place cells. The black trace is the experiment gain. The dots are gain estimated in real time using unsorted spikes from a tetrode. Colors of the dots represent different tetrodes. The yellow trace is the median of the gain estimates from all the tetrodes and is defined as the online gain estimate. (B) - (I) is the flowchart showing the steps of the online implementation of the spectral gain estimator. (B) Neural data and experiment related data (such as angular position of the rat) is being collected by two different computers. The clocks of the two computers are synchronized using a pseudo-random signal sent between the computers and the timestamps of the data collected on both computers is brought to a common time frame. (C) The data is collected in 10s buffers and sent to a third computer which does the rest of the steps. (D) Data within a sliding spatial window, from the current location to 6 laps prior, is considered. (E) The velocity of the animal is calculated from the angular position data and filtered with the same parameters used for the analysis in Chapter 4. This is used to filter out spikes that fired at velocities less than 50/sec. (F) The spikes are spatially binned and the occupancy time of each bin is computed. (E) The occupancy corrected firing rate is calculated and (F) smoothed. (G) The spatial frequency of this segment of spike firing is calculated using the same spectral decoding algorithm as described in Chapter 4.

5.3 Contributions

The work in this chapter was primarily my contribution with external contributions listed below.

Enhancing gain estimation using place field detection: The decision to use kernel density estimation as the foundation for field detection builds off work previously done by Manu S Madhav and Macauley Breault.

Online gain estimation from unsorted spikes: Manu S Madhav contributed equally in all aspects of the development of the online implementation of the gain estimation. This was a highly collaborative effort that needed a lot of combined effort, brainstorming, debugging, and testing. Manu S Madhav made the flowchart portion of Figure 5.3 while I made the subplot with

the example dataset of online gain decoding. I wrote up the collaborative implementation independently for this thesis.

Chapter 6

Looking beyond place cells: investigation of the head direction cell network and potential role of gamma oscillations

For this chapter, I performed the majority of the analysis and generation of figures in this chapter. I wrote the text and the work has not yet been published elsewhere. External contributions are detailed at the end of this chapter

6.1 Investigation of the head direction (HD) cell network

We have data from one rat where we recorded simultaneously from place cells in CA1 and from head direction (HD) cells under the same gain manipulation protocol used in the datasets in Chapter 4 The head direction of the animal

was tracked using the 3D head tracking system described in Appendix A. Figure 6.1 shows one representative experiment from this dataset. The first 4 panels show a replication of the results shown previously where CA1 place cells behave as a coherent population, showing landmark control under gain manipulation and recalibration of the path integration gain (as read out from CA1 place cells) once the landmarks are extinguished. The last set of sub-figures describe the behavior of a simultaneously recorded head direction cell as polar plots where the angle is the direction of tuning and the radius is the head direction occupancy corrected firing rate. The first row shows the head direction tuning when the animal is stationary and looking around. The second row shows the tuning when the rat is running. The plots are split up into blocks with data from Epochs 1 (gain 1), Epoch 3 (plateau gain), and Epoch 4 (landmarks off). The title of each of the columns of plots shows the frame of reference.

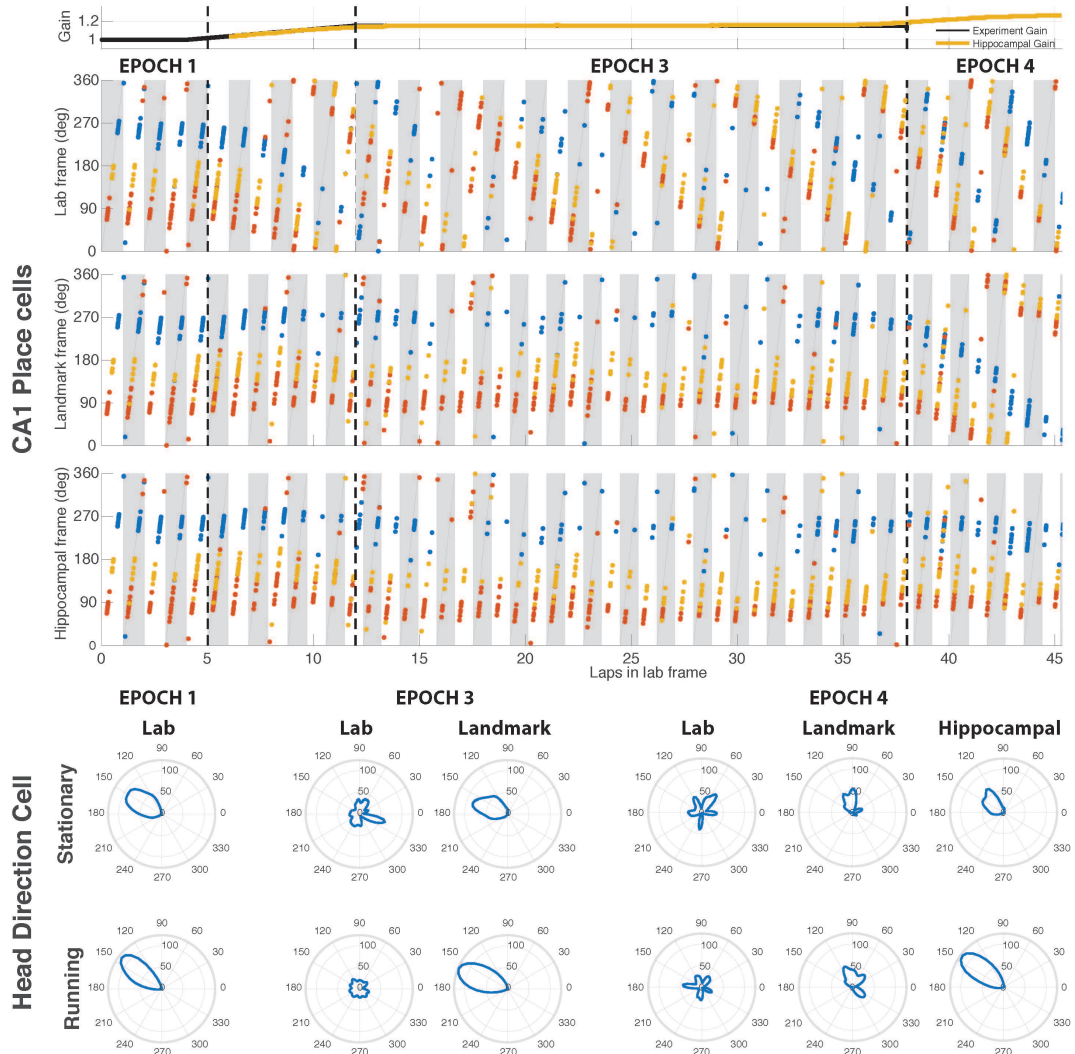


Figure 6.1: Preliminary data from simultaneously recorded place cells and head direction cells in a gain manipulation experiment

In general the tuning curves appear to be a bit wide when the rat is stationary versus when the rat is running. In Epoch 1, the HD tuning direction is the same when the animal is stationary and running. In Epoch 3, the cell shows little to no tuning in the lab frame while the tuning is still preserved in the landmark frame, which means that the internal frame of reference is locked

to the landmark frame. In Epoch 4, the tuning is degraded for both the lab and landmark frame (had the landmark frame still continued rotating at the same gain). However, when plotted in the hippocampal frame of reference (as determined by the hippocampal gain estimated from CA1 cells, the HD cell show a well defined tuning. This implies that the internal frame of reference of the HD cells is in sync with the recalibrated hippocampal frame of reference.

This cannot be taken as evidence of recalibration of the inputs to the head direction cells. The rotation of the frame of reference of head direction cells may be driven by hippocampal feedback when the animal is running. Chapter 7 includes discussion of ways in which this may be happening. The way to ascertain if the HD cells have recalibrated is to check the head direction tuning of these cells when the animal is stationary and looking around. In this behavioral epoch, the head direction cells gets inputs from motor efference and sensory re-afference. Sensory re-afference can include vestibular, proprioceptive, and external inputs from landmark (spatial and non-spatial) and optic flow cues. These inputs drive the bump of activity around the closed ring of HD neurons mapping the angular space. If the HD cell network has recalibrated, then the gain manipulation would have modulated how fast this bump of activity traverses this ring in the absence of external inputs. This would in Epoch 4 of the gain manipulation experiments where the projected visual cues have been extinguished and due to the design of the dome apparatus, other landmark cues have been minimized. Local optic flow is present to an extent. When recording from HD cells (in a stationary animal), evidence of recalibration can manifest itself in two ways. One, compared to the control

epoch 1, the width of head direction tuning of each HD cell is modulated by the recalibration amount - gains less than 1 will manifest itself as wider tuning width and gains greater than 1 will be narrower. The second is to compare the angular distances between the the tuning direction between two HD cells as compared to their distance in control epoch 1. If the distance gets larger, the HD gain has recalibrated to values less than 1 and vice versa for if the distance gets shorter.

The caveat here is that even if recalibration of the HD cells is not observed in this analysis, it does not rule out context dependent recalibration where the recalibration is only engaged during animal locomotion.

Preliminary evidence suggests that the HD cells do recalibrate but to a different extent than what is seen in the place cells. Figures 6.2, 6.3, and 6.1 show data from a session where the experiment gain was taken to 1.77. Figure 6.2 shows spikes from a CA1 place cell plotted in the lab frame with laps on the x axis and track angle on the y axis. The place cell starts off with one field at the start of the experiment. The dashed line shows when the landmarks were turned off. At this point, there are two repetitions of the field indicating that the hippocampal gain was approximately 2 once the landmarks were turned off.

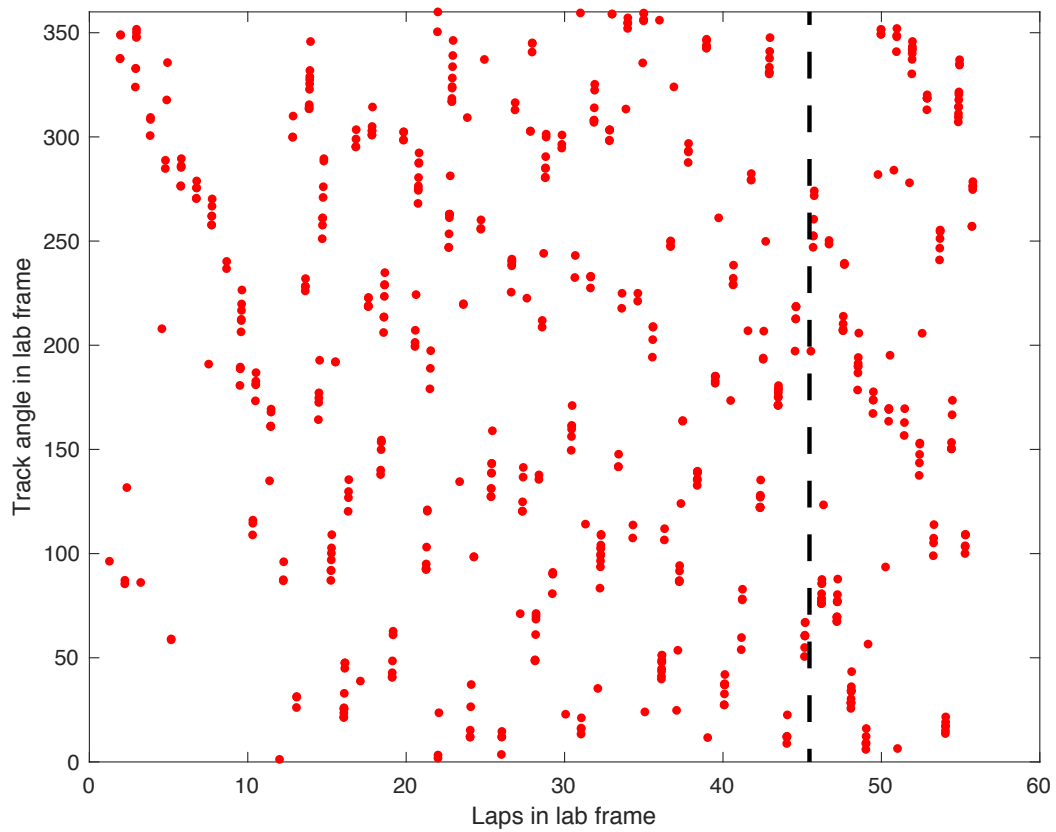


Figure 6.2: Simultaneous place and head direction cell recalibration experiment: Place cell spike plot

Figure 6.3 shows the head direction tuning of two simultaneously recorded HD cells with the animal's head angle on the angular axis and head occupancy corrected firing rate on the radial axis. The data is from Epoch 1 when the landmarks were visible and stationary. The left panel shows the data when the animal was stationary (body velocity < 5 cm/s) and the right panel is with the animal running (body velocity > 5 cm/s).

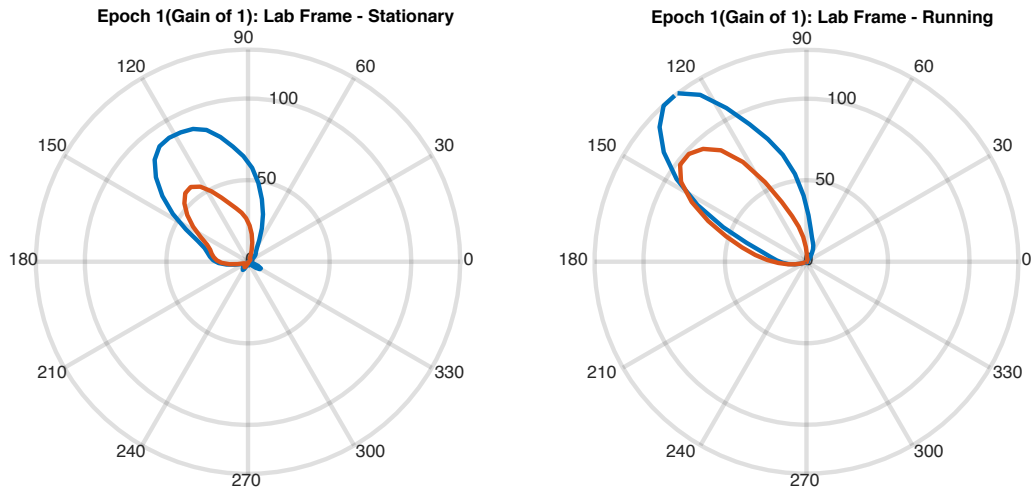


Figure 6.3: Simultaneous place and head direction cell recalibration experiment: HD cell tuning.

Table 6.1 shows data from these two cells where the start and ends of individual passes through the tuning field of each cell in Epoch 1 and Epoch 4, with the animal stationary and running, was manually found. The field widths in Epoch 1 establishes the baseline width of the field in each of the movement conditions. The recalibrated gain in each of the movement condition is defined as the ratio between the average field width in Epoch 1 versus Epoch 4. For both cells, the recalibrated gain under the running condition is approximately the same as that seen in the place cell. However, the recalibrated gain under the stationary condition is significantly lower. This indicates that the HD cells do recalibrate but not to the same extent as the place cells.

HD cell 1 (cell id 5):	Epoch 1: Stationary			Epoch 4: Stationary		
	Field Start	Field End	Field Width	Field Start	Field End	Field Width
	77	220	143	78	205	127
	37	204	167	90	208	118
	25	192	167	100	209	109
	29	173	144	84	200	116
38	185	147				

HD cell 2 (cell id 10):	Epoch 1: Stationary			Epoch 4: Stationary		
	Field Start	Field End	Field Width	Field Start	Field End	Field Width
	78	221	143	79	183	104
	73	204	131	91	208	117
	89	211	122	100	207	107
	43	189	146	91	199	108
	38	176	138			
29	167	138				

HD cell 1 (cell id 5):	Epoch 1: Running			Epoch 4: Running		
	Field Start	Field End	Field Width	Field Start	Field End	Field Width
	61	158	97	138	176	38
	42	146	104	133	176	43
	78	166	88	98	152	54
	77	166	89	320	375	55
	73	174	101	309	350	41
83	178	95			46.2	

HD cell 2 (cell id 10):	Epoch 1: Stationary			Epoch 4: Stationary		
	Field Start	Field End	Field Width	Field Start	Field End	Field Width
	118	197	79	141	181	40
	97	179	82	121	155	34
	93	172	79	108	138	30
	97	167	70	319	350	31
	98	175	77	295	325	30
	97	165	68	330	374	44
91	159	68	327	378	51	

HD cell 1 (cell id 5):	Mean Field Width	Epoch 1	Epoch 4	Recalibrated Gain
	Stationary	153.6	117.5	1.307234043
	Running	95.66666667	46.2	2.070707071

HD cell 2 (cell id 10):	Mean Field Width	Epoch 1	Epoch 4	Recalibrated Gain
	Stationary	136.3333333	109	1.250764526
	Running	74.71428571	37.14285714	2.011538462

Table 6.1: Simultaneous place and head direction cell recalibration experiment: HD cell tuning width and recalibration gain.

6.2 Potential role of gamma oscillations on the asymmetry of neural response to gain manipulation

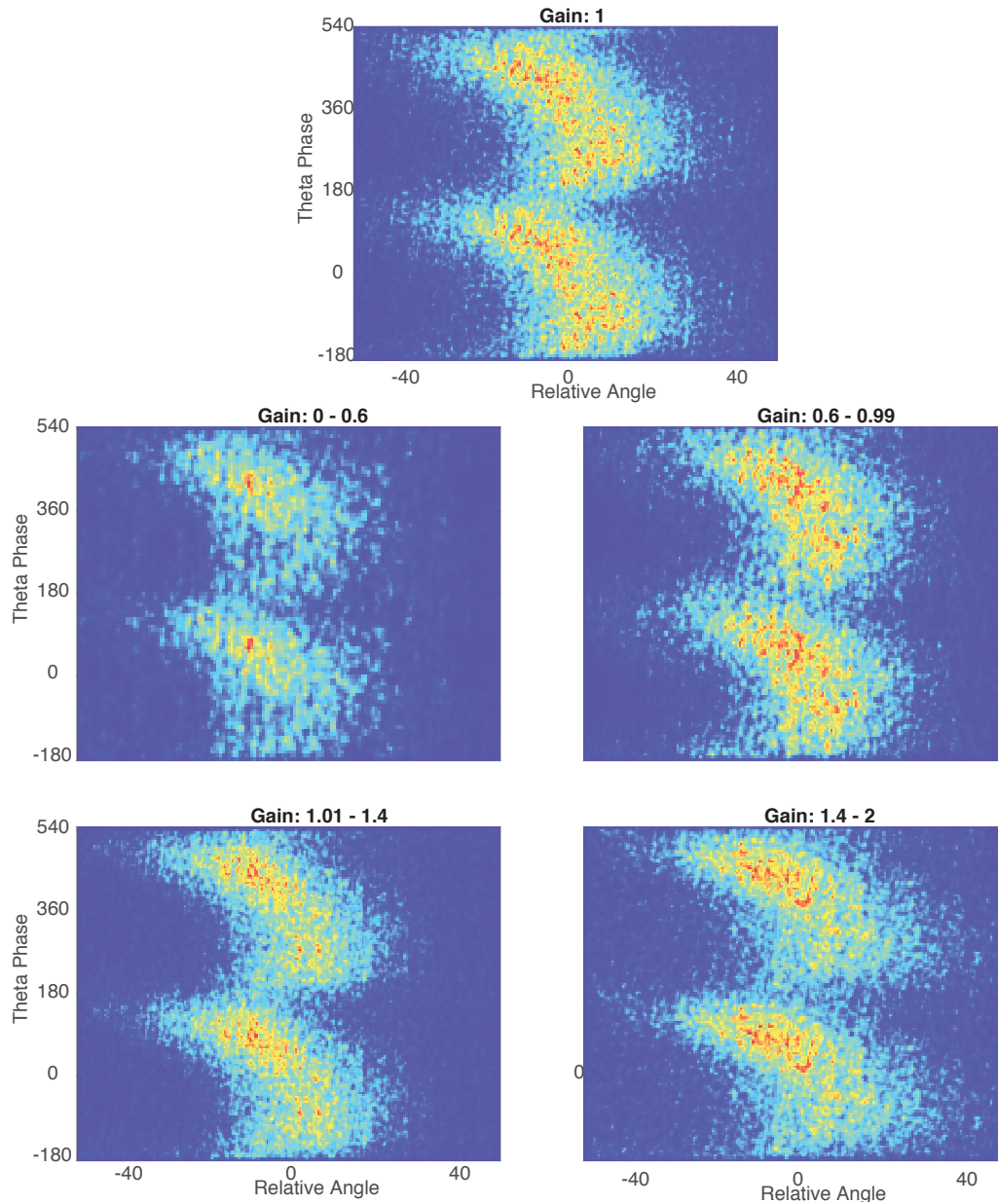


Figure 6.4: Gain modulation of average theta precession of place cells (from the dataset used for drift calculation in Chapter 4)

Theta precession is the phenomenon in which, as the animal runs through a place field of a place cell, the cell fires spikes in time with the underlying theta oscillation in the local field potential such that the spikes are at a later phase at the start of the place field and gradually shift to earlier phases as the animal progresses through the field. The precession usually has a stereotypical banana shape with two parts to the precession, one showing slow precession in the late phases of theta and the second showing faster, more random firing across a range of early phases of theta. Figure 6.4 shows the mean theta precession of spikes fired between Epochs 1-3 by stable place cells with a single place field. The theta precession phenomenon is still preserved on average at all ranges of gain with perhaps the exception of the averaged theta precession between gains 0-0.6 where the second half of the precession appears a bit sparse, indicating that a relatively lower number of spikes appear to be firing locked to the earlier phases of theta at those gain values.

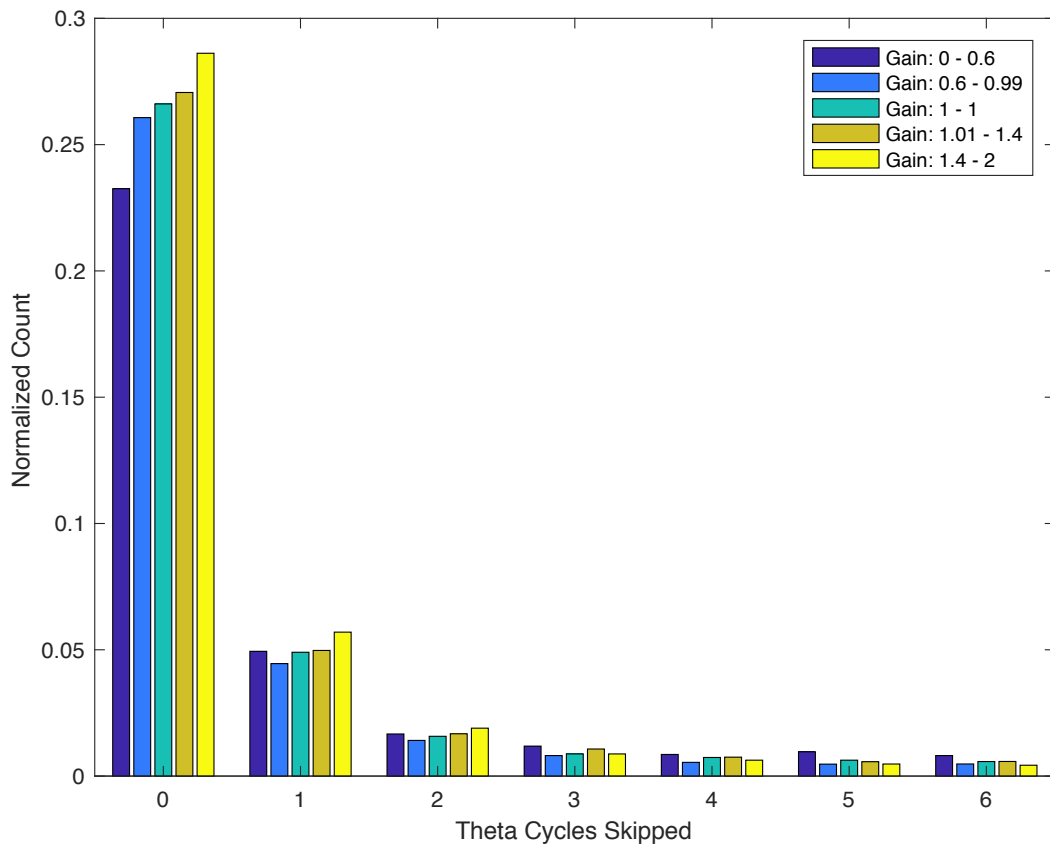
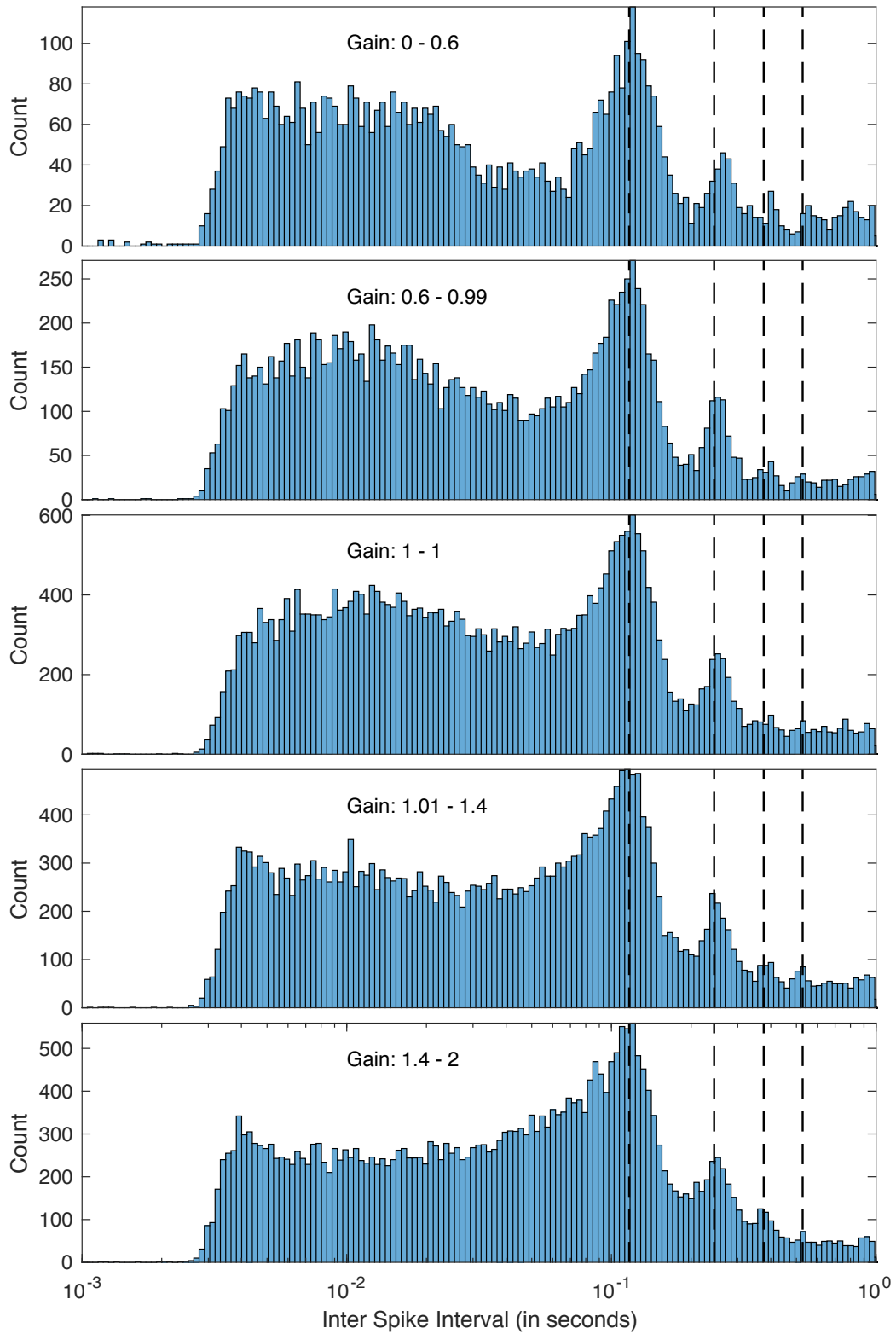


Figure 6.5: Histogram of theta cycles skipped by spikes in place cells from the dataset used for drift calculation in Figure 4.9.

Figure 6.5 shows further supporting evidence. The plot shows the relative number of instances of number of theta cycles skipped (normalized to the total count in a gain range) for place cells used in the dataset for place field drift calculation in Figure 4.9. There is a clear trend of there being more skipped theta cycles with decreasing gain. This theta skipping could explain the sparsity observed in the second half of the precession for the range of gain 0-0.6 in Figure 6.4.



131
Figure 6.6: Histogram of inter-spike interval (ISI) histogram of spikes in place cells from the dataset used for drift calculation in Figure 4.9.

Figure 6.6 shows the histogram of interspike interval of spikes of a place cell at different ranges of gain when landmarks were visible. The dataset of place cells used were the same as that used for drift calculation in Figure 4.9 i.e. place cells that had a single stable place field from Epochs 1-3. The firing locked to theta frequency (and its sub-harmonics) stays about the same for a gain of 1 and above, but increases its ISI (or in other words, decreases its frequency of firing) for gains less than 1. The peak height at theta decreases relative to the rest of the histogram with lower gains. This corresponds well with the valley developing with lower gain in the ISI histogram to the left of the peak at theta. One of the reasons for the formation of this valley might correspond to the firing locked to the higher harmonics of theta as Figure 6.7 shows that the power in the higher harmonics of theta are lower for gains less than 1 relative to the control condition and gains greater than 1.

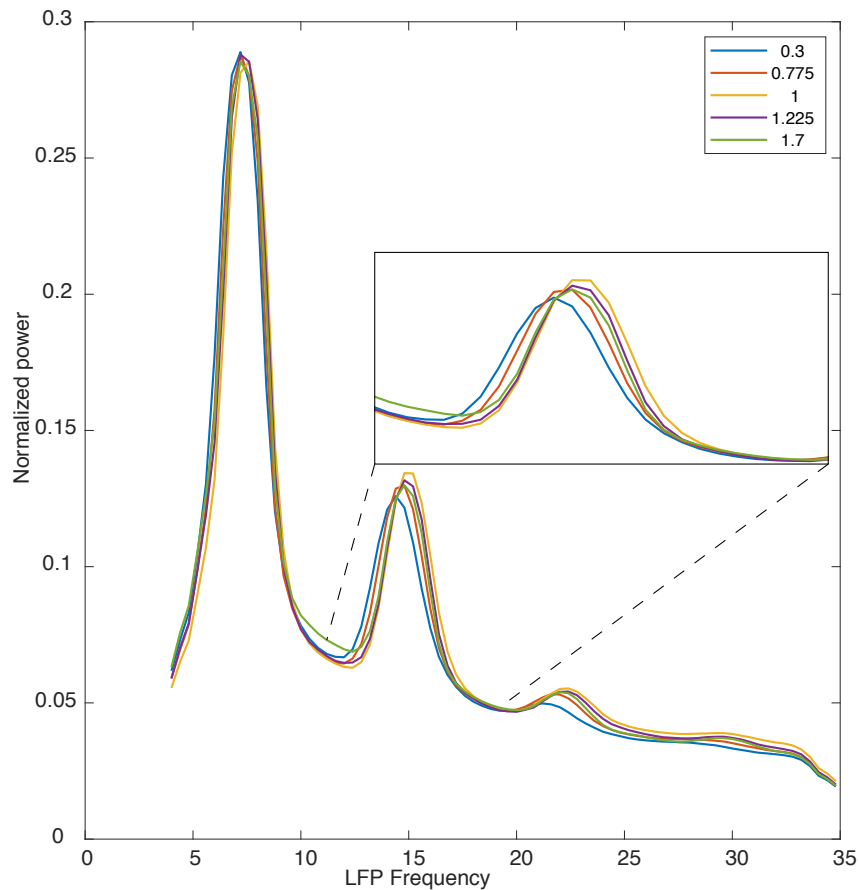


Figure 6.7: Average frequency content in the local field potential in the theta and higher harmonic range of frequencies at instances when the animal is moving.

Figure 6.6 also shows a possible but not so clear modulation of the ISI distribution in the gamma range of frequencies. Plotting the histogram of spike ISI versus theta phase (Figure 6.8) allows a closer, albeit rough, study of how the spikes are locked to different frequencies as the animal progresses through a place field. Two cycles of theta are plotted to better disambiguate circular wraparound.

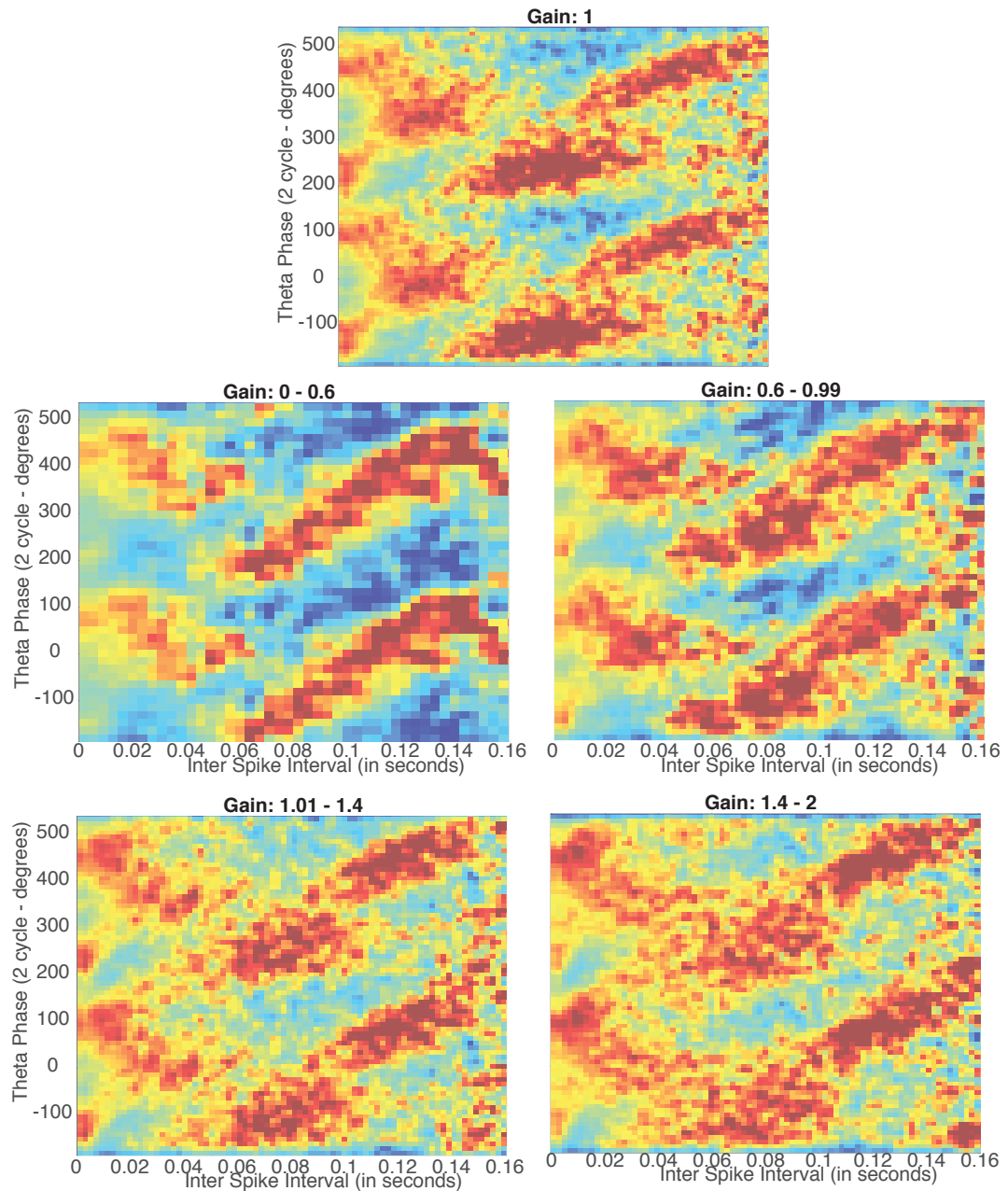


Figure 6.8: 2D histogram of inter-spike interval versus theta phase of spikes in place cells from the dataset used for drift calculation in Figure 4.9.

Let's first characterize the plot in the standard condition at a gain of 1. There appears to be three main components to this plot with each component

showing its own dynamics.

The first component is the progression of the theta precession seen in the hot zone starting at a later phase with a larger ISI. As the spikes fire at earlier phases, the ISI also goes down leading to theta precession due to the changing difference in frequencies between the LFP theta and the spike firing frequency. A relatively clean almost-linear decrease is seen in ISI with decreasing phase until at one point, this trend breaks with a high count blob forming at an earlier phase of theta and between ISIs in the frequency equivalent range of 10 - 25Hz. This most likely corresponds to the second half of theta precession, with the blob like nature corresponding well to the sporadic firing in this half. The linear section would correspond to the initial slow half of theta precession.

The second component is on the left third of the figure with ISIs in the gamma range of frequencies (0.007 - 0.025s). The gamma range of oscillations can be further subdivided into three parts - slow gamma(40 - 70Hz or 0.025 - 0.014s), medium gamma (70 - 100Hz or 0.014 - 0.01s) and fast gamma (100 - 140 Hz or 0.01 - 0.007s).

It is hard to disambiguate between what's happening in fast gamma and the spike burst frequency range (0.001 - 0.005s), the third component of this plot, at this resolution and will need more refined analysis. However, the two things to note at this stage is (1) the conspicuous concentration of ISIs in the combined spike burst-fast gamma range happening at the start and end of theta precession and (2) the nature of the change of this concentration at different ranges of gains.

We'll take a look at what's happening in the slow and medium gamma

range and discuss its implications. As the theta precession starts at the start of a field at a later phase, there is a high concentration at the medium gamma range. This concentration moves towards the low gamma range and reaches a peak roughly at the end of the slow half of theta precession. Then the concentration moves back into the medium gamma range as the second half of theta precession starts firing. This movement from medium to slow back to medium gamma shows an almost symmetric distribution of concentration.

All of the above observations are consistent with previously published results (Colgin et al., 2009). This concludes the characterization of the components of this plot at a gain of 1. The following effects are seen at other ranges of gain:

- For all ranges of gain, the slow half of theta precession remains roughly the same. The hotspot corresponding to the second half starts becoming larger and more diffuse for gain > 1. For gain < 1, the hotspot starts disappearing with lower gains till it looks like a continuous progression of the linear slow precession all the way through the field at the gain range 0 - 0.6.
- At all gains, there is a concentration at medium gamma at the start of the field which is more prominent for larger gains and almost nonexistent at the lowest gain range. This concentration moves towards the slow gamma range as in the control condition and then moves back to medium gamma towards the end of theta precession. There is a shift from the symmetric distribution of concentration in this back and forth movement at a gain of 1 to an asymmetry biased towards later theta phase – so

much so that the movement from slow gamma back to medium gamma is almost nonexistent. The hotspot of concentration at slow gamma at the schism between the two halves of theta precession shows a similar effect as the fast theta precession hotspot at different gain ranges.

Figure 6.9 shows the average frequency content in the slow and medium gamma range at instances when the animal is moving. The left panel shows normalized local field potential power and the right panel shows mean subtracted LFP power. Compared to a baseline at gain 1, slow gamma power increases and fast gamma power decreases with further deviations from 1. In both cases, the deviations are more exacerbated for gain ranges below 1 as compared to equivalent gain ranges above 1.

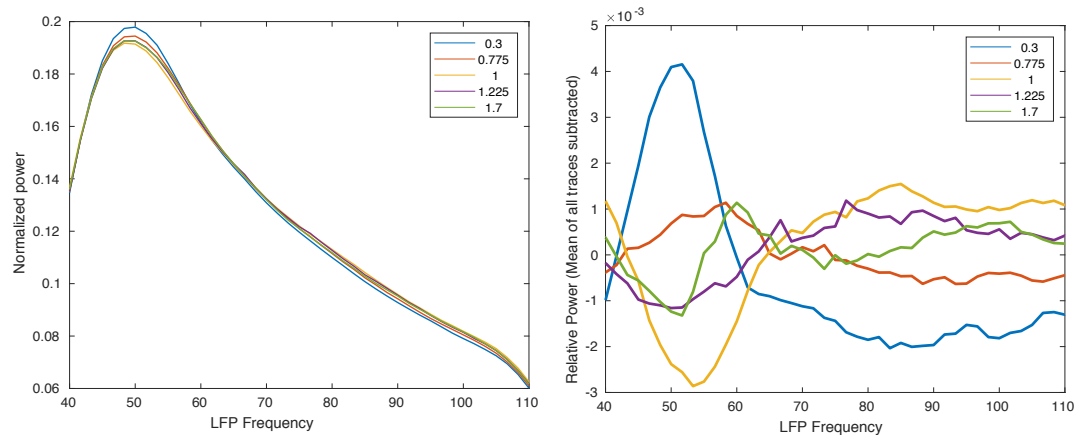


Figure 6.9: Average frequency content in the slow and medium gamma range at instances when the animal is moving. The left panel shows normalized local field potential power and the right panel shows mean subtracted LFP power.

This seems to be congruent with the findings of Kemere et al., 2013. An excerpt from the abstract of this paper: “*found evidence suggestive of a smooth transition from strong CA3 drive of CA1 activity at low speeds to entorhinal cortical*

drive of CA1 activity at higher speeds. These changes occurred with changes in behavior on a timescale of less than a second, suggesting a continuous modulation of information processing in the hippocampal circuit as a function of behavioral state."

The next question is if this speed modulated transition from CA3 to MEC drive is based on speed in lab frame or landmark/hippocampal frame. Figure 6.10 shows data from Rat 692, which had landmark control over a large range of gains. Landmarks were on. The peak gamma frequency for low and medium gamma at a range of velocities is shown. The left panel only includes data from when the experiment gain was 1. The relationship between peak gamma frequency and animal velocity is very similar to that described in Zheng et al., 2015.

The right panel includes data from when the experiment gain was away from 1. The top right panel has velocities in lab frame. The bottom right panel has velocities in landmark frame. The relationship between peak gamma frequency and velocity is preserved in landmark frame.

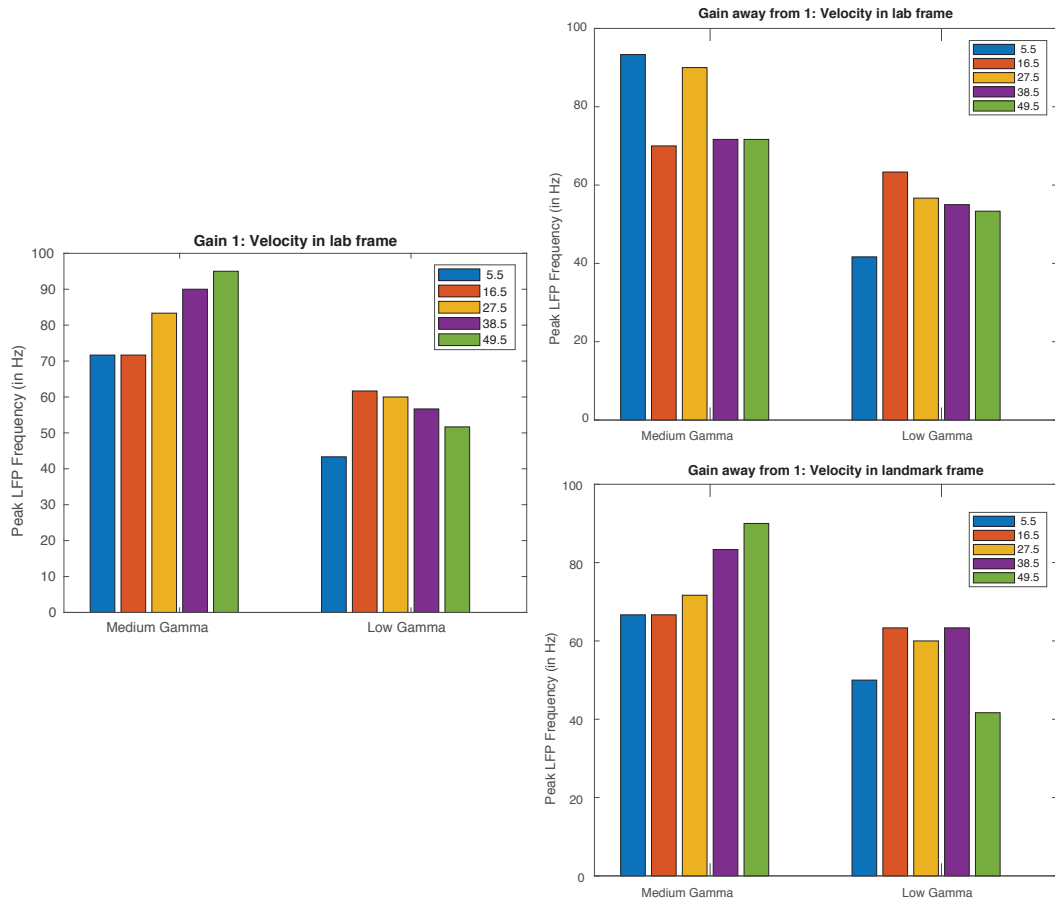


Figure 6.10: Relationship between peak gamma frequency and velocity in lab and landmark frames. The bar graph shows the frequency with the maximum power in the slow and fast gamma ranges for a range of velocities (in cm/s) of the animal in different frames of reference. The left panel has data with animal velocity in lab frame and experiment gain at 1. The top right panel data with animal velocity in lab frame and experiment gain away from 1. Bottom right panel shows the same data except in landmark frame.

Thus, for a given value of running speed of the animal in lab frame, values of gain less than 1 would cause the animal to experience a perceptually lower speed, potentially inducing more CA3 drive as compared to a gain of unity condition. Gain values greater than 1 would cause the animal to experience a perceptually higher speed, potentially inducing more MEC drive to CA1 as

compared to a gain of unity condition. The data in the figures described thus far support this.

A similar asymmetry also shows up when looking at sharp wave ripples (SWRs). Figure 6.11 shows the number of cells recruited in SWRs as a function of gain. This is data from one rat. SWRs were detected using code made publicly available by the Buzsaki lab. The number of cells recruited is relatively constant for gains greater than 1. For gain less than 1, it increases with lower gain.

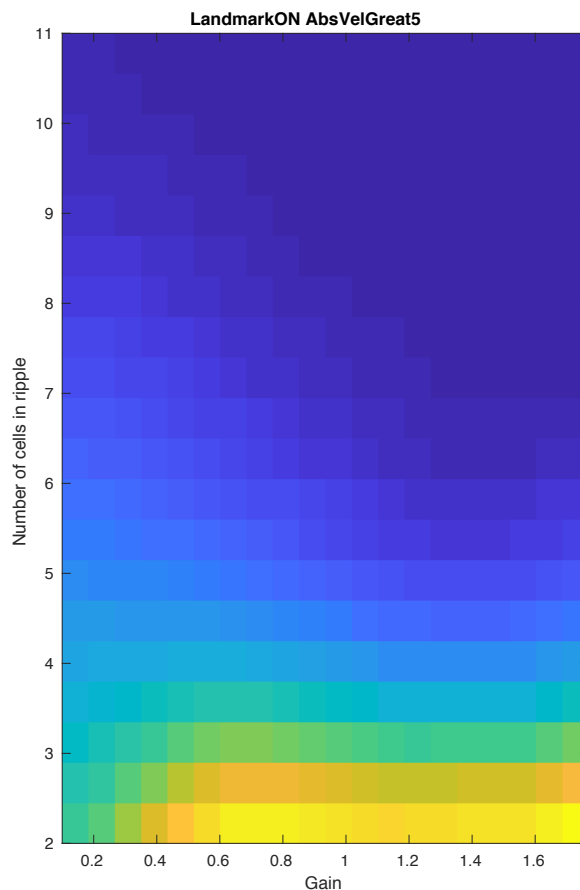


Figure 6.11: 2D histogram of experiment gain versus number of cells recruited in sharp-wave ripples (SWRs).

This matches with the results from Amemiya and Redish, 2018. An excerpt from page 8 of this paper: *“Our data reveal that intrinsic asymmetry of theta cycles reflects the gamma states: more asymmetric theta with a relatively longer HG phase reflects preference for current location representations, and more symmetric theta with a relatively longer LG phase reflects farther search processes. Associated with these different theta wave shapes, ensemble activity of cells in asymmetric theta cycles preferentially represents the current location, and ensemble activity of cells in symmetric theta cycles preferentially represents future locations.”*

The reason that these observations may be critically important is its implications in the asymmetry observed in gain manipulation experiments detailed in Chapter 4. Landmarks were able to establish control over the place cell map in a majority of sessions. But the rare cases where it did lose control, the gain was always less than 1. Other asymmetries were observed even in the presence of landmark control. The first row of Figure 6.12 shows examples of typical theta precession in individual passes through a field at different gains. The third example covers almost 2 meters. However, this isn't always the case. In the following example that looks at fields from a place cell on an experiment day when the gain was driven to 0, examples are shown of theta precession being preserved at gains close to 1 but as the gain starts getting lower, some instances of fields show fractured theta precession, breaking down into multiple precessions. Anecdotally, there also appears to be some methods to this madness of fractured theta precession that when taken on average, still shows a typical theta precession. For example, we would see a typical theta precession when taking the average of fractured theta precessions

where the peak spike density within each of the multiple precessions goes from a later to an earlier phase.

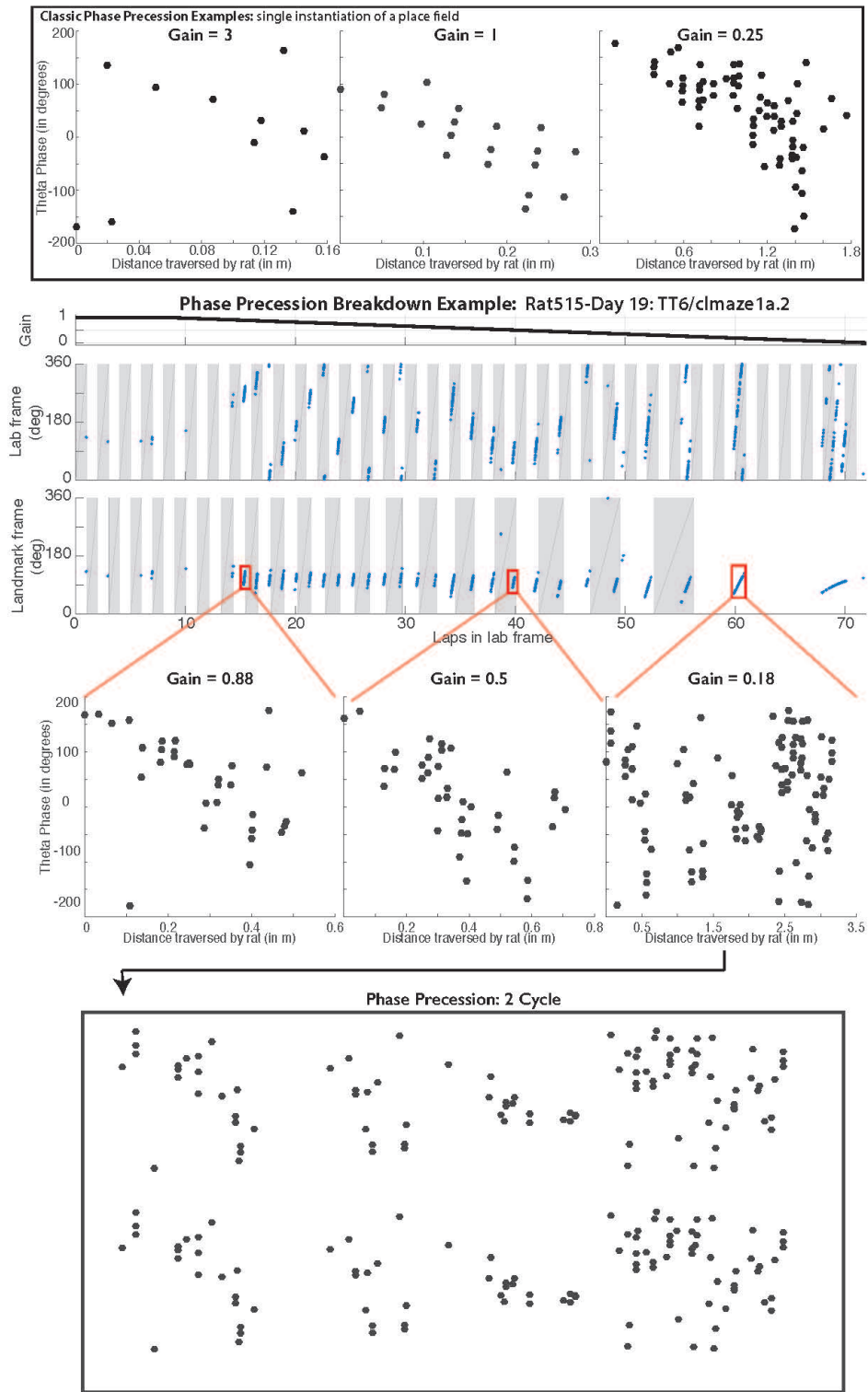


Figure 6.12: Examples of theta precession: stereotypical and during breakdown.

This manner of theta precession, where spurts of the early phase of precession interjects in between breakdown only seemed to happen for gains less than 1 and more frequent the lower the gain got.

It is known that theta precession of CA1 place cells, CA1 medium gamma, driven by direct inputs from the MEC, peaks at the beginning and end of the theta precession cycle and that CA1 slow gamma has the most influence mid theta precession cycle (Colgin et al., 2009). CA1 pyramidal cells firing gets phase modulated by inhibitory control by CA1 interneurons, which in turn receive driving input from CA3 slow gamma (Csicsvari, Jamieson, et al., 2003).

It has been known previously that LTP in CA1 is most easily induced at a particular phase of theta, corresponding to when EC drive was high (from Colgin et al., 2009: linked sources: Huerta and Lisman, 1995, Hasselmo, Bodelón, and Wyble, 2002). The phase corresponding to maximal CA3 input was thought to be linked to memory retrieval. However, recent results have implicated phase locked firing to slow gamma in being involved in modulating synaptic plasticity during novelty learning. An excerpt from the abstract of Kitanishi et al., 2015

“By devising a virus-mediated approach to perform multi-tetrode recording from genetically manipulated neurons, we demonstrated that synaptic plasticity dependent on the GluR1 subunit of AMPA (Îs-amino-3-hydroxy-5-methyl-4-isoxazole propionate) receptor mediates two dynamic changes in neuronal firing in the hippocampal CA1 area during novel experiences: the establishment of phase-locked firing to slow gamma oscillations and the rapid formation of the spatial firing pattern of place cells. The results suggest a series of events potentially underlying the acquisition of new

spatial information: slow gamma oscillations, originating from the CA3 area, induce the two GluR1-dependent changes of CA1 neuronal firing, which in turn determine information flow in the hippocampal-entorhinal system. ”

6.3 Contributions

The work in this chapter was primarily my contribution with external contributions listed below.

Investigation of the head direction cell network: Marissa Ferreyros and Nick Lukish trained the animals used in the experiments and assisted with surgery, turning tetrodes, and running experiments. They also built the hyperdrives used for these experiments. Marissa did the brunt of the analysis of the head direction data thus far. Manu did the surgeries. Manu and I ran the experiments on the first animal and worked to get 3D head tracking working in an experiment setup. I ran subsequent experiments and oversaw training, tetrode turning, hyperdrive building, and analysis.

Potential role of gamma oscillations on the asymmetry of neural response to gain manipulation: Manu Madhav wrote the code computing the theta phases of the spikes. Figures 6.4 and 6.12 looking at average theta precession and instances of breakdown of theta precession was a collaborative effort by Manu and me.

Chapter 7

Discussion

7.1 Recalibration of path integration in hippocampal place cells

The material from the discussion section of Jayakumar et al., 2019, of which I was the co-first author, has been used verbatim for this section

Using a novel augmented reality dome apparatus, we show here that the path integration system employs a modifiable gain factor that can be recalibrated to a new value that can remain stable for at least several minutes in the absence of salient landmarks. Recalibration of this nature has been described extensively in other systems. The cerebellum plays a key role in recalibration of feedforward motor commands (Bastian, 2006). Similarly, the gain of the vestibulo-ocular reflex adapts to changes in the magnitude of retinal slip caused by magnifying glasses, an effect that persists even after the glasses are removed (Miles and Lisberger, 1981). As with our own results, the recalibration is not perfect in these motor adaptation tasks; i.e., the gain measured after the training trials are biased towards, but not precisely the same as, the

experimental gain implemented during the training trials. To our knowledge, such gain recalibration has not been demonstrated physiologically in cognitive phenomena such as spatial representation and path integration (but see Tcheang, Bulthoff, and Burgess, 2011b). The lack of complete recalibration may be due to an insufficient number of training laps during Epoch 3, or may reflect inherent limits on the plasticity of the path integrator gain variable.

It is widely accepted that visual landmarks provide a signal to correct error that accumulates during path integration (Terrazas et al., 2005b). The results in this paper demonstrate physiological evidence for a role of vision in the path integration computation itself by providing an error signal analogous to retinal slip in the VOR (Miles and Lisberger, 1981). Specifically, this error signal fine-tunes the gain of the path integrator (Tcheang, Bulthoff, and Burgess, 2011b), minimizing the accumulation of error in the first place. Although recalibration of the path integrator gain may be expected over developmental time scales, these results indicate that the path integration gain is fine-tuned even at behavioral time scales. This fine-tuning may be required to (a) maintain accuracy of the path integration signal under different behavioral conditions (e.g., locomotion on different surfaces that provide varying degrees of slip and cause alterations in the self-motion inputs to the path integrator); (b) synchronize the different types of self-motion signals (e.g., vestibular, optic flow, motor copy, or proprioception) thought to underlie path integration; and (c) coordinate the discrete set of different path integration gains thought to underlie the expansion of grid scales along the dorsal-ventral axis of the medial entorhinal cortex (Hasselmo, Giocomo, and Zilli, 2007, Terrazas et al., 2005b,

A. P. Maurer et al., 2005). The recalibration might be implemented by changes to the head direction (citeCullenSense2017) or speed (Kropff et al., 2015b, Hinman et al., 2016) signals that provide input to a path integration circuit. Alternatively, these representations may be unaltered and the gain changes are implemented by changing the synaptic weights between the inputs and putative attractor networks that perform the path integration (Samsonovich and McNaughton, 1997, Fuhs and Touretzky, 2006, McNaughton, Battaglia, et al., 2006, Blair, Gupta, and Zhang, 2008). The augmented reality system described here will allow the investigation of mechanisms underlying the interaction between external sensory input and the internal neural dynamics at the core of the path integration system.

We also show that in the majority of cases, visual landmarks reliably control the location of place fields, even under severe landmark manipulation. Removing the landmarks revealed that the path integrator is recalibrated to a gain lower in magnitude (but always consistent in direction) than the final experiment gain. Thus it is extremely likely that the path integrator gain is not the same as the experiment gain even in the presence of the landmarks. Indeed, a slow drift of the place fields against the landmarks was measured even under conditions of (preponderant) landmark control, possibly as a result of an inherent, continuous conflict between the position as informed by the landmarks and the position as computed by path integration. We observed drifts of place fields in both positive and negative directions, as a linear function of experimental gain. In our control (no landmark manipulation) trials, the drift had a slightly negative bias ($-X \pm Y$ degrees). This is similar to

the backward expansion / drift of place fields on a track that has previously been observed (Mehta, Barnes, and McNaughton, 1997). If this drift is due to path integration, these results might suggest that path integration tends to overestimate distance even in the normal condition.

7.2 Further developments to spectral gain estimator

7.2.1 Enhancing gain estimation using place field detection

Beyond getting a refined gain estimate, the field detection process is also vital for implementing the standard suite of place field analysis in the field. Studies into place fields, in general, do not look at individual passes of the place field but rather the combined average of neuronal firing in all passes through a stable field. Some of the characteristics studied are place field size, mean and peak firing rate, theta modulation and average theta precession, burstiness, interspike intervals etc.

A place field is stable in the hippocampal frame of reference by definition. The decoder as described in Chapter 4 could approximate this to an extent but uncompensated effects such as field drift and slow oscillation would cause the averaged place field to be larger and more diffuse. This would cause distortion in many of the standard place field measures such as its size, mean and peak firing rate, shallower average theta precession. Not accounting for this drift/oscillations can also blur the precise timing of spikes relative to position in field for theta precession causing what might be a precise mechanism to appear more stochastic.

In addition to the standard averaged place field analyses, which deal with a static picture that does not take into account the dynamics in the neuronal response either due to internal dynamics or due to response to the dynamic stimulus enforced by the experiment, we can also start extending these analyses to see the time varying responses of these standard measures. This is of particular import to the study of the dynamic change in theta precession, interspike intervals and its interplay with the underlying local field potential. Preliminary evidence discussed in Chapter 6—such as interesting and complex interactions between the spike firing and local field potentials, putative influence of other brain regions and the role of optic flow in this system—is hinting at fundamental insights into the mechanisms that define the hippocampal spatial map.

7.2.2 Decoding on unsorted spikes

The utility of decoding the gain from unsorted spikes is many-fold. First, it can potentially yield a more robust decoding of the gain estimate. This is due to two factors. One is that remapping of a small subset of a large population of neurons recorded in a tetrode, which is generally what tends to happen in these experiments, may not significantly change the shape of the spatial tuning curve formed by the superposition of the firing of the entire population of neurons. This will result in a more continuous gain estimate. Second, the experimenter can start analysis of the data almost immediately after the

experiment without going through the intermediate step of manual cluster cutting. While many analyses will still require sorted spikes, there are also a significant number of analyses that can be done just using the gain estimate assuming that the coherent population response still holds true. This is also especially useful as the experimenter can get immediate feedback about the outcome of an experiment and potentially use this information to close the loop in determining the parameters of subsequent experiments.

7.2.3 Online gain estimation from unsorted spikes

While real-time estimation of gain is a useful feature for monitoring the neural response during an experiment, the real power of this lies in the fact that the experimenter can now close the loop by having the experiment parameters such as the applied visual gain now be modulated by the neural feedback. This makes possible a number of previously infeasible experiments. One such experiment is testing if gain manipulation of optic flow can result in recalibration of the path integrator gain.

Optic flow has experimentally investigated to a relatively lesser degree (Sharp et al., 1995; Arleo et al., 2013) in spite of its theoretically (Raudies, Mingolla, and Hasselmo, 2012; Raudies, Hinman, and Hasselmo, 2016) and empirically motivated (Sherrill et al., 2015; Tcheang, Bulthoff, and Burgess, 2011b) role in spatial processing in the hippocampal formation. A single study shows preliminary, but convincing, evidence that optic flow can bias the preferred direction of HD cells to rotate in the same direction (clockwise or counter-clockwise) as a drifting pattern of random dots in the periphery

(Arleo et al., 2013).

The necessity of implementing neural closed loop feedback for optic flow based recalibration experiments is due to the nature of spatial information provided by optic flow, or indeed any other form of self-motion input. Salient landmarks directly give the animal an indication of its position in its environment. This allows the animal's internal map to instantly correct any drift with respect to the external world by triangulating its location with respect to the landmarks. Thus, in a gain manipulation experiment with landmarks, this influence by salient landmarks makes driving the internal hippocampal gain to the experiment gain relatively easy

For optic flow however, the input is a velocity signal which has to be integrated to get a position estimate. This is prone to accumulating error introduced by noisy measurements or inherent neural stochasticity. Thus, when applying a gain to the optic flow, the internal map may indeed update its position estimate based on the integrated velocity cues but the accumulating error means that the effective hippocampal gain will most likely not follow the applied experiment gain. However, if the experimenter is able to determine the hippocampal gain in real time, a control law can be applied to the experiment gain as a function of the current and desired hippocampal gain to drive the hippocampal gain to the desired gain. This allows the experimenter to perform recalibration experiments using optic flow and maintain the place cell map at gains that they choose rather than have it drift in a random and uncontrolled fashion in the open loop case.

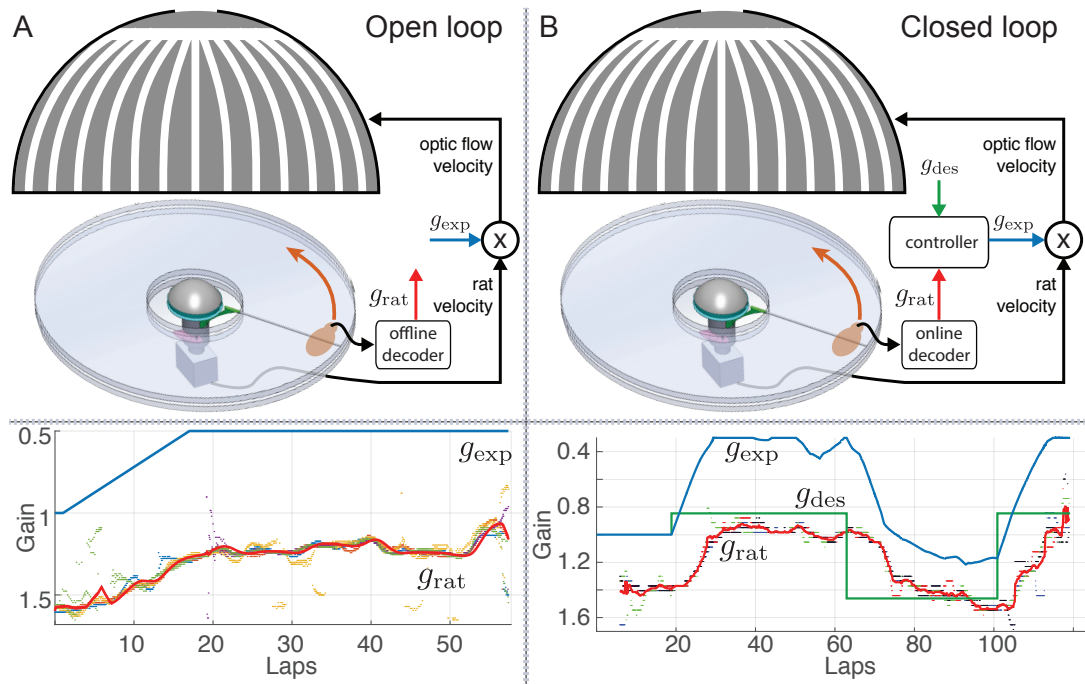


Figure 7.1: Open- and closed-loop control of place fields by optic flow. (A) In the Open-loop experiment, the rat's velocity is measured through the optical encoder at the center of the table, and multiplied by the pre-determined experimental gain (g_{exp}) value in order to determine optic flow velocity. Using the neural recordings, we spectrally decoded an estimate of the rat's internal gain (g_{rat}) post-hoc. Data from a single trial (bottom) indicates that the rate of change of the rat's internal gain tracks that of the experimental gain. (B) In the closed-loop experiment, the internal gain is estimated online, and its error with respect to the pre-determined desired gain (g_{des}) is used to determine the instantaneous value of g_{exp} . The data from a closed-loop trial shows g_{rat} coarsely tracking g_{des} .

7.3 Looking beyond place cells: investigation of the head direction cell network and potential role of gamma oscillations

7.3.1 Investigation of the head direction cell network

Although the CA1 population shows evidence of recalibration of the path integrator, we do not yet know where and how recalibration is implemented

neurally. Since the rat is running in a circle of a fairly large diameter, its locomotion is a combination of linear and angular movement. There are multiple sensory modalities that could be used for path integration, such as optic flow, vestibular and proprioceptive. Each of these modalities could be integrated with its own gain and then incorporated into a combined path-integrative estimate. On the other hand, the path integrator gain may be an abstract quantity independent of sensory modalities. We also do not yet know the loci of the functional implementation of this recalibration in the rodent brain. Given the angular-linear nature of the animal's locomotion, head direction cells in the anterior dorsal thalamic nucleus and grid cells and speed cells in the medial entorhinal cortex were potential suspects for further investigation.

When the animal is running around the track, there is a linear and an angular component to the movement. This engages both the place cell and HD cell network. One cause for the HD cells maintaining their tuning in the hippocampal frame of reference in the absence of landmarks could be that the frame of reference of the HD cells is being driven by the rotation of the place cell map. How does the place cell map rotate when not driven by HD cells? One possibility, suggested by Prof James Knierim, is by the use of step counting. During the epochs when the landmarks are on, as the animal runs laps, it progresses sequentially through a series of place cells, each one being a certain linear and angular distance away from the previous one and eventually closes back on the first in the sequence. Continuous exposure to this sequence lap after lap could cause the recurrent collateral system of CA3 cells

to increase the strength of connection of this circular sequence of cells forming a pseudo 1-D "map". The connection strength between two consecutive cells can be equivalent to the integrated driving input by step counting needed for travel from one to the other. Gain manipulation can cause the step counter to recalibrate resulting in a modulation of driving input to CA3 place cells for a given step. This could appear externally as the recalibration phenomenon seen in Chapter 4. In the absence of landmarks, the path integration input from step counting can drive the sequential activation of this 1D circular network of cells in CA3—and subsequently in CA1 which receives CA3 inputs and purportedly would not have its own attractor dynamics owing to its parallel organization in terms of connectivity (Amaral and Witter, 1989)—in this recalibrated state which when seen from the lab frame of reference could appear as if the hippocampal map is rotating with respect to the external world. The hippocampal map may in turn be dominant over the HD cell map when running and cause the HD cell map to stay locked to it, causing it to "rotate" its frame of reference as well.

Another potential implementation of this same result is where a 2D map with place cells tiling the environment exists but now there is an interaction between the self-motion inputs. As the animal continually runs laps in the presence of landmarks, if a mechanism exists for the network to learn that a step taken along this circular trajectory corresponds to both a linear and angular distance traveled, then once the landmarks are extinguished, the driving input from step counting could cause the trajectory to move forward by both a linear and angular amount with each step. Then, if the drive from

step counting input experiences recalibration in the previously described manner, this can cause the hippocampal map to rotate with respect to the lab frame. Thus, when locomoting, the animal could still traverse a circular trajectory that has an 'angular' component without an explicit directional input from the HD cells.

7.3.1.1 Possible mechanism for higher frequency of place field remapping in gain manipulation compared to gain of unity condition

As mentioned in Chapter 4, the recorded place cell map undergoes more frequently in the gain manipulation experiments as compared to the normal gain of unity condition. The remapping is also observed to varying degrees in the population of cells being recorded. Some may be stable, some may be dynamically undergoing rate remapping, some cells may turn on or off entirely, or even change position. Global remapping of all cells is rarely observed. I suggest below a mechanism and an accompanying simulation by which these experiments could be inducing this level of remapping with Figure 7.2.

As described in Chapter 4, even in epochs with landmark control, place fields drift in a direction consistent with a small but ever present influence of path integration. This drift means that the effective hippocampal gain even during landmark control is slightly away from the experiment gain. A simple model for representing this might be one where the hippocampal gain G_{hipp} is a weighted mean of the experiment gain G_{exp} and the path integrator gain,

G_{pi} with weights w_{exp} and w_{pi} respectively.

$$G_{hipp} = w_{exp}G_{exp} + w_{pi}G_{pi} \quad (7.1)$$

where $0 \leq w_{exp}, w_{pi} \leq 1$ and $w_{exp} + w_{pi} = 1$

As the animal runs around the track, its movement has a linear and angular component. The above equation would represent a path integrator gain being applied to the combined path integrator signal. If separate gains were being applied to the subsystems involved in each component, then it might be represented as,

$$G_{hipp:linear} = w_{exp:linear}G_{exp} + w_{pi:linear}G_{pi:linear}$$

$$G_{hipp:angular} = w_{exp:angular}G_{exp} + w_{pi:angular}G_{pi:angular} \quad (7.2)$$

When the landmarks are stationary, one may assume that the gains are tuned such that the error between the estimates from path integration and the external landmarks is minimal. In this case, as the rat runs laps on the track, its trajectory through its internal map may look like the top left panel in Figure 7.2 where the internal trajectory almost exactly reflects the circular path that the rat is running.

The results from Chapter 4 shows that the path integrator gain is indeed getting recalibrated during gain manipulation. If the underlying mechanism is as in Eq 7.1, with one path integrator gain G_{pi} applied to a combined path integrator signal as in Eq 7.1, the trajectory in its internal map would continue to be a tight circular trajectory. If there was a 2D place cell map tiling the

environment and the animal's trajectory were to cause it to traverse across the fields of three place cells shown in red, green, and blue shaded regions, the resulting spike firing from these cells will result in a stable firing as shown in the bottom left panel of the figure. Fluctuations in w_{pi} would yield the same outcome.

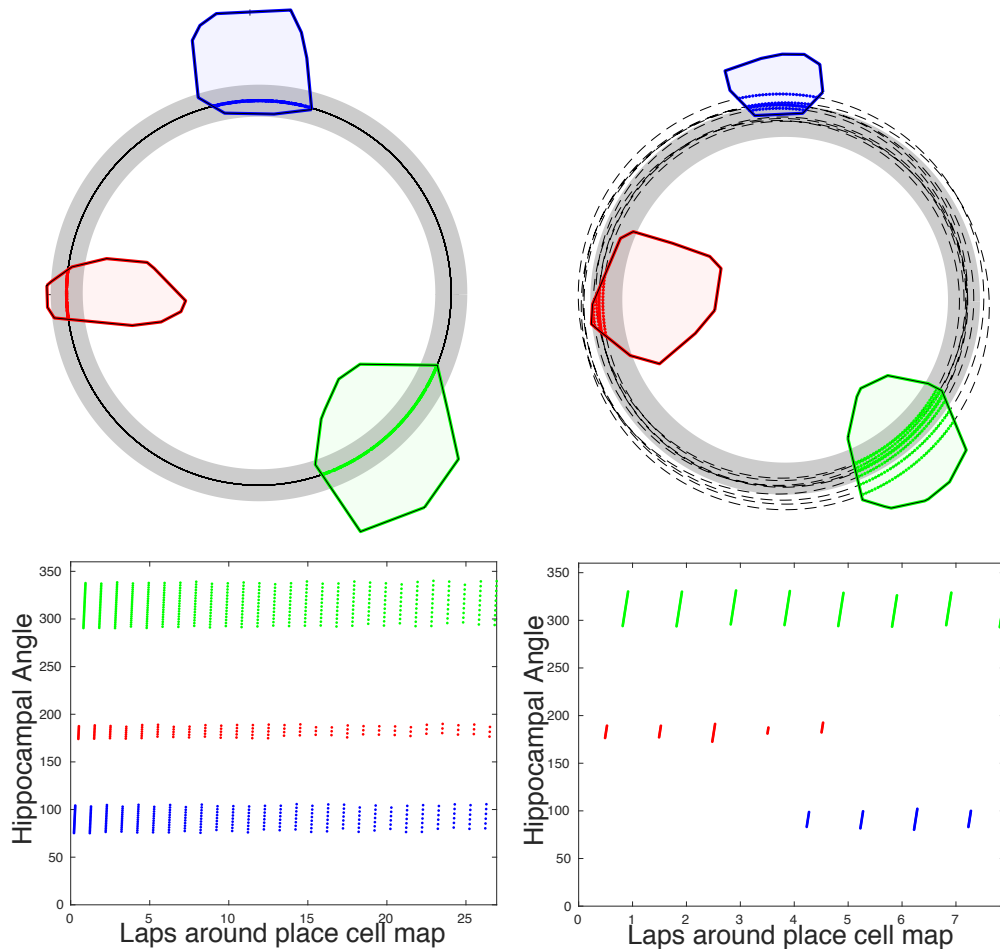


Figure 7.2

Figure 7.2 (previous page): Simulation of remapping mechanism. The top row is the overhead view of the animal's internal representation of the track that it is running on. The place fields of three place cells are shown as the red, green, and blue shaded regions. The black dashed line (appears as a solid line in the left panel due to overlap of multiple dashed lines) represents the trajectory of the animal through its internal place cell map. The bottom row shows a spike plot in the same format as used in Chapter 4. The laps run around the hippocampal map is shown on the horizontal axis. The angle on the track in hippocampal space is shown on the vertical axis. The spikes fired by each place cell as the animal's trajectory intersects with the place fields are shown in the corresponding color coded dots

However, if the underlying mechanism is as in Eq 7.2 with the linear and angular components having independent gains, ignoring fluctuations in the weights, $w_{exp:linear}$, $w_{exp:angular}$, $w_{pi:angular}$ and $w_{pi:linear}$ for the moment, two scenarios can happen:

- The linear and angular components of movement get recalibrated at about the same rate. The trajectory in its internal map would continue to be a tight circular trajectory and will result in a stable firing as shown in the bottom left panel of the figure.
- If the linear and angular component gains recalibrate at even slightly different rates, the trajectory in its internal map would deviate from the tight circular trajectory. As an example, assume noisy rates of recalibration. In Figure 7.2, the top right panel shows a case where the gains on the linear and angular components are indeed changing, due to being enforced by landmarks and recalibration but there is a small stochastic difference between the two gains in the rate at which they change. The result is that the internal trajectory is no longer a tight circle but one which meanders around the circle. The intersection of this trajectory

through the fields of three place cells would now result in spike firing as shown in the bottom right panel. This shows almost exactly the kind of remapping seen in the gain manipulation experiments. Do note that this mechanism cannot explain position remapping unless the place cell has multiple fields and the meandering trajectory happens to intersect with the other fields.

It is to be noted that, even under the first scenario with equal rates of calibration, unequal fluctuations in the weights between angular and linear components can result in the same remapping like phenomenon shown above.

Extending this mechanism to MEC recordings, one could even see what looks like remapping in the firing of grid cells - which aren't traditionally prone to remapping - due to the internal trajectory deviating from the animal's trajectory in the actual world. Head direction cells would broadly maintain their tuning but would still show the fluctuations associated with the gain/weights ($G_{hipp:angular}$) of the angular component of movement. Reconstruction of the 2D internal map and the animal's trajectory through it may allow determination of the underlying nature of the fluctuations, be it in the weights or in the rates at which the gains get recalibrated.

Another mechanism for remapping proposed by Prof. James Knierim was that the map itself is fluctuating and the fields are drifting around, possibly due to the strength of the synaptic connection between place cells being modified during the recalibration process and consequently, presumably, the spatial distance between them (Muller, Stead, and Pach, 1996, Isaac et al., 2009). If the field drift is coherent, perhaps due to a global shift of the

internal map's relationship to the gain-modulated distal cues, this would be equivalent to a fluctuating internal trajectory and the two mechanisms would yield indistinguishable place cell recordings.

However, under the fluctuating map mechanism, if the individual fields themselves were drifting relative to each other, then the resultant place cell remapping would not be consistent with a shift of the whole map and would be more random in nature.

This is all under the assumption that the dynamics of the fluctuating internal trajectory is slow, which would be supported by the fact that even the place fields which remap tend to be stable for many laps.

7.3.2 Potential role of gamma oscillations on the asymmetry of neural response to gain manipulation

I speculate a description of what could be happening in gain manipulation experiments that ties together the results in Section 6.2. The MEC and CA3 have recurrent connectivity that facilitates attractor dynamics. The internal representation of position in MEC may be a bump of activity in an attractor that's mainly path integrator driven. The internal representation of position in CA3 (in conjunction with dentate gyrus inputs) may be a bump in an attractor that's mainly driven by external landmarks (Kesner, 2007; Rolls, 2013; J. W. Lee et al., 2012; J. W. Lee et al., 2009; Yoder, B. J. Clark, and Taube, 2011).

Under normal conditions (gain = 1), the coherence of internal representation between CA3 and MEC is mediated by information transfer via CA1. CA1

cells get MEC drive mediated by medium gamma at the early and late phases of theta oscillation in CA1(essentially the same since the phase wraps around). CA3 drive to CA1 cells comes in at middle phases of theta mediated by slow gamma (Colgin et al., 2009). Synaptic plasticity may be induced in CA1 due to MEC and CA3 drive ((from Colgin et al., 2009: linked sources: Huerta and Lisman, 1995, Hasselmo, Bodelón, and Wyble, 2002), Kitanishi et al., 2015). This results in a representation of position in CA1 that is influenced by the representation of position in MEC and CA3 in an alternating fashion relative to theta phase and is weighted by the level of synaptic plasticity induced by the drive from each region. This is, in essence, a prediction (using path integration by MEC) and correction (using visual cues by CA3) process with synaptic plasticity determining the weighting. This weighted CA1 representation could then be projected back, possibly in the same medium gamma epochs, to the deep layers of MEC. The deep layers then projects back to the superficial layers as well as to other brain regions, unifying the representation across multiple brain regions. MEC may have its own correction and recalibration step where it uses the difference between its estimate of position to the weighted CA1 position to calibrate the path integrator gain.

Gain manipulation in recalibration experiments affects the animal's perception of motion. The results of Section 6.2 suggest that the gamma oscillations relationship to speed is maintained in the landmark frame, not the lab frame. This result combined with the results from Kemere et al., 2013, which shows a transition from CA3 drive of CA1 activity at low speeds to EC drive of CA1 activity at higher speeds, means that the modulation of perceived speed can

alter the level of drive provided by MEC and CA3 to CA1 compared to a gain of unity condition, with a perceived lower speed increasing CA3-driven low gamma and a perceived faster speed increasing MEC-driven medium gamma. Zheng et al., 2015 shows that CA3 slow gamma frequency has regions of high power for speeds of 0 to ~ 24 cm/s with a slow gamma frequency of peak power ramping up from 3 cm/s to 24 cm/s. MEC has high levels of medium gamma activity above 24 cm/s.

Consider a gain manipulation experiment where the experiment gain is greater than 1. The animal perceives itself as moving faster than it actually is (6.10) which bumps up epochs of movement normally slow enough to be within the range of heightened CA3-driven slow gamma, up into the range of of heightened MEC-driven medium gamma. Thus, on average, there is more of a MEC drive on CA1 as compared to a unity gain condition. However, given the nature of the task, a well-trained animal is executing repeated stop-go ballistic movements between drops of liquid reward on the track. As the animal stops to lick the liquid reward, the animal will frequently have movement epochs where the speed is slow enough for CA3 slow gamma drive to be dominant. Thus, even though the tendency is towards MEC drive due to a higher perceived velocity, the CA1 representation of position will still have influence from CA3 regularly when the animal slows down at the reward drops.

The same, however, does not hold true for experiment gains less than 1. The animal perceives itself as moving slower than it actually is (6.10) which bumps down epochs of movement normally fast enough to be within the

range of heightened MEC-driven medium gamma, down into the range of heightened CA3-driven slow gamma. Thus, on average, there is more of a CA3 drive on CA1 as compared to a unity gain condition. However, an animal cannot run infinitely fast in the lab frame. In addition, due to the frequent stop-go ballistic nature of movement and the physical restraints of the experiment setup, the animal may only be able to achieve limited top speeds. The average top speed of a rat in the gain manipulation experiments in Chapter 4 was about 50-60 cm/s. Given this range of peak velocities, the experiment gains would need to be 0.4 - 0.48 to bump the perceptual velocity down to the slow gamma range at a threshold of ~ 24 cm/s,

In a gain manipulation experiment where the gain is lower than 1, assume that the distal cues started off exerting landmark control. The experiment gain being lower than 1 causes the perceptual velocity to be lower than the velocity in lab frame. Thus, at lower values of gain, there is a lower likelihood of the perceptual velocity crossing the slow gamma to medium gamma threshold. In that case, the CA1 place cell representation will be more often driven by CA3 with intermittent synchronizations with MEC whenever medium gamma drive goes up due to higher velocity. Incidentally, the theta precession breakdown at gain less than 1 showing multiple fast precession phases may be evidence of this intermittent synchronization.

An animal may place a weight for external landmarks that reflects its belief in that object as a static reliable landmark to which it can lock its cognitive map. At each synchronization with MEC, if the error between the CA3 driven position estimate and the MEC position estimate has drifted far enough, this

may drive belief in the reliability of landmarks to gradually deteriorate. The mechanism behind this may be a form of synaptic LTD due to the place cell firing spikes that were firing out of order in the theta precession of the cell active at the moment of synchronization. If the experiment gain is maintained at this low value, the deterioration of the belief in the landmarks becomes a runaway process till landmark control finally fails. Thus, the probability of landmark failure will be a function of both the running behavior of the individual rat and the gain applied.

Predictions:

- At lower values of gain, the MEC representation of position will drift from the CA1 representations with possible intermittent weighted corrections to this drift. This may be behaviorally linked to the animal intermittently achieving a high enough running speed to cause CA1 to receive MEC driven medium gamma.
- Such drift corrections may also manifest itself in the firing of CA1 place cells as theta precession breakdowns in the form of a sudden spurt of spikes firing at early phases of theta. The early phase of theta is when MEC-driven medium gamma has preferential influence. The MEC may also show simultaneous spikes in medium gamma amplitude.
- There might be a theoretical lower limit to the value that the path integrator gain can recalibrate to. Every animal will have a limited maximum running speed. There will be a corresponding gain greater than 0 and less than 1 that will cause the perceived running speed to go into the

slow gamma range. If recalibration occurs as a result of using the error signal between MEC and CA3 mediated by the slow gamma - medium gamma epochs for transmission and coordination of this error signal, then at low enough gain values, synchronization between the regions is highly unlikely to happen except by chance and recalibration of the path integration will cease.

7.4 Conclusion

The dome experiment apparatus and estimator is designed to give the experimenter an unprecedented level of real time control in perturbing the different streams of spatial inputs received by the animal. This will enable us to pull apart at the seams of how the internal dynamics of the hippocampal formation, with its intricate feedback networks, incorporates landmark and path integrative information, adapting to and resolving conflicting information, to form and maintain a representation of the world. The phenomenon of recalibration of the path integrator gain reveals that this network is able to quickly adapt in the presence of conflicting landmark information. Experiments are ongoing to figure out the roles played by the other participating brain regions in this process and at what stages of processing this recalibration is realized. Further studies will follow up on how the different modalities of path integration (optic flow, vestibular, proprioceptive) interact with each other. The inputs to the system can be enriched by adopting system identification principles. And finally, studies will be done to investigate the real-world implications of these findings i.e how the distortion of the internal spatial map affects the decision

making processes and cost functions involved in cognitive tasks set in this distorted map.

The dome apparatus, as it is right now, does have the limitation of having the animal run in a simple circular 1D trajectory in a 2D space. But this simplicity and the circular nature of the trajectory affords dimensionality reduction and a regular sampling of the entire space. Under the assumption that the spatial map instantiated in the hippocampal formation in both 1D and 2D environments arises from a set of fundamental mechanisms, a comprehensive characterization of the dynamics in a lower dimension will provide a solid foundation towards deciphering the results of experiments that bring in more spatial - and non-spatial - dimensions, completing the picture.

Appendix A

Real time 6DoF pose estimation of animal's head for head direction cell analysis and enabling freely behaving animal

A robust high-precision single-camera system was developed for tracking the pose – position (x,y,z) and orientation (roll, pitch, yaw) – of a custom visual target attached to a test subject. The system builds upon existing monocular tracking algorithms, referred to as Perspective from n Points (PnP), that use a visual target comprising point-like fiducials (passive retroreflective markers in our implementation) arranged in known configuration (Faessler et al., 2014, Savkin et al., 2017). Such methods are constrained by the trade-off between fiducial count and range of detectable orientations. A low fiducial count

limits the range of angles from which enough fiducials are visible due to self-occlusion, leading to loss of tracking, time needed for video processing and recapture of target pose upon loss of tracking scales poorly with the number of fiducials due the combinatorial complexity of possible point correspondences. We introduce geometric constraints and multiple fiducial sizes, drastically reducing the number of possible correspondences facilitating a higher fiducial count. Our improvements enable real time operation (15-30 ms per frame at 4MP resolution using 11 fiducials) in a host of new applications where a wide range of orientations need to be tracked. The system consists of custom software, a Near-IR camera, an IR LED light source mounted near the camera, and the custom visual target (a example shown in Figure A.1) described above. The software can process a video file input, but is also capable of real time operation on live camera images with a supported camera model. Cost of implementation is a fraction of commercially available solutions. The tracker's real time mode is being used to manipulate the visual scene in the augmented reality dome described in Jayakumar et al., 2019. Previously, the dome system relied on the animal being tethered to a boom arm instrumented with an angular optical encoder that measured the position of the animal as it ran on a circular track. The new real time tracking system allows for a freely behaving, untethered animal. We also present results from an experiment where the system, post-processing a video file, was used to track the head of a rat. In the experiment, the surrounding visual scene of virtual landmarks was either static or rotated coherently as a function of the rat's running speed. Simultaneous neural recordings were taken from CA1 place cells and ADN head direction cells. We find that that the place cell and head direction cell

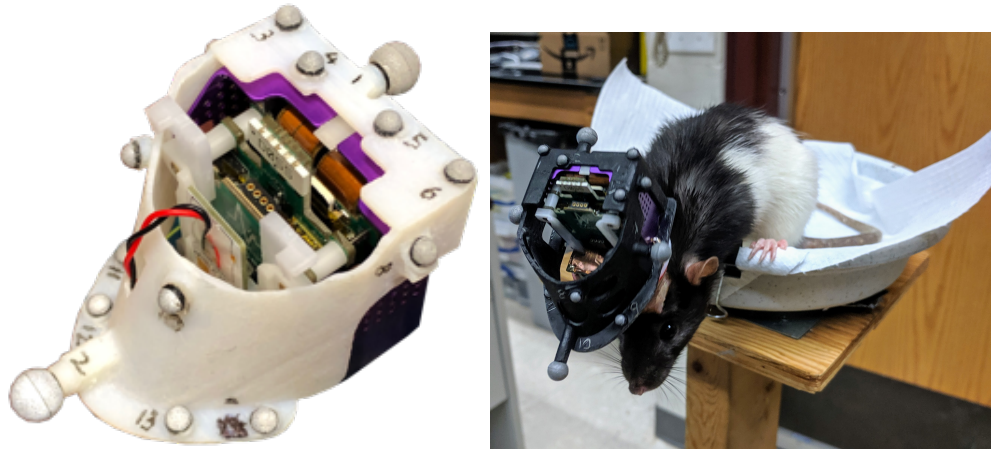


Figure A.1: 6DoF head tracking. The left panel shows a close up of a version of the physical tracker using a 3D arrangement of retroreflective markers on a Neuralynx wireless recording headstage. The right panel shows a similar version of this tracker on a rat

map respond coherently to the visual cue manipulation. This was described in more detail in Section 6.1.

Contributions: Balazs Vagvolgyi developed the software code that does the tracking. Manu Madhav implemented the tracking code into the experiment control code and gave feedback on the hardware design. I designed and built the hardware. All three of us were involved in testing, debugging, contributing of ideas for adopting Balaz's tracking algorithm to the particulars of running in an animal experiment

Appendix B

Evolution of the hyperdrive design

The neural recordings in the experiments detailed in Part II are done using tetrodes, a twisted bundle of four electrode wires, implanted in the brain. Each tetrode is attached to a microdrive that allows high-precision linear actuation of the tetrode into the brain towards to sub-region of interest. We used an design incorporating an array of 18 microdrives, called the Endodrive, which was the design by Francesco Savelli and JD Luck. This design comprised of three functional components. One is the drive core which houses a set of 18 microdrives. The next is the bottom bundle which determined the 2D distribution of how tetrodes enter the brain and is attached to the skull at the time of surgery. The third is the walls which go between the drive core and the electronic interface board(to which the the tetrodes are crimped to) and contains the tetrodes inside the drive core while providing a support for the EIB. This is a highly robust and versatile design with a well built drive of this design being easy to use in terms of microdrive actuation and

implanting during surgery. The cannulae carrying the tetrodes also had to bend through a shallower angle. There were versions of the bottom bundle with different tip geometries suited for recording in specific brain sub-regions. The design was much more compact than previous designs which meant that the impact on the animal after surgery was reduced. The tetrodes and microdrive mechanisms were enclosed and well protected. This design was also highly resistant to damage from impacts.

However, the overall level of skill required in getting a well built endodrive which has all of the above characteristics is fairly high. The skill level also determined how much time was needed to build a usable endodrive. The drive building process also has certain steps that are especially sensitive to the level of focus and fine motor skills, which can vary in a person day by day or as fatigue builds up. Thus, even for someone highly skilled at building an endodrive, there would be variability in quality across multiple builds of the drive.

While retaining the foundational principles behind the endodrive design, the retained design components was refined and a plethora of new design features added, with the following guiding principles in mind: 1) Reduce time of manufacture 2) Reduce skill of manufacture 2) Reduce variability of manufacture.

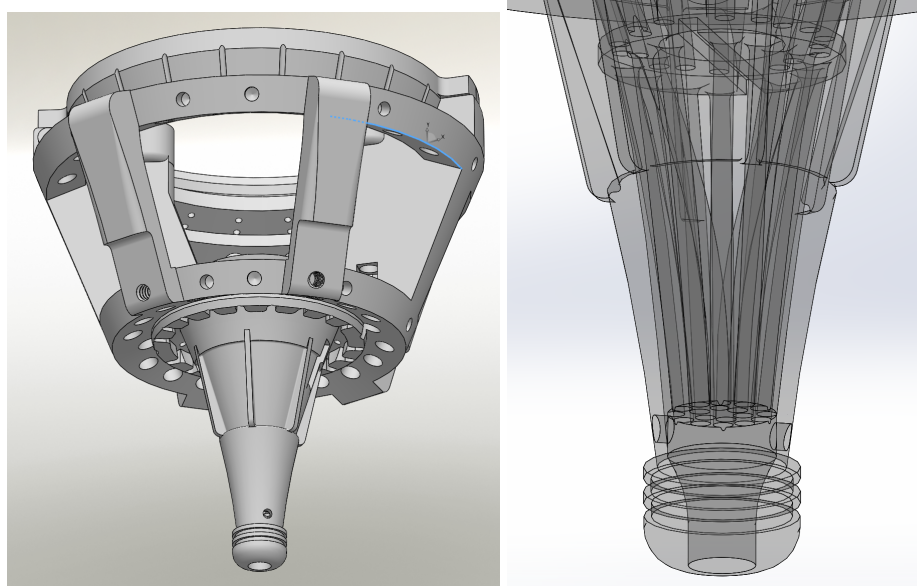


Figure B.1: Unibody hyperdrive. The left panel shows the body of the drive. The right panel has a transparent version of the drive showing the the dedicated pathways for the tetrode guide and carrier cannulae

The following are some of the more significant design modifications. The unibody design (Figure B.1) combines all the functional components of the endodrive into a single rigid 3D printable structure and predefined cannulae paths are printed as a part of the drive. This serves all three design objectives mentioned. The tetrode guide cannulae paths are printed ready-to-use and do not need to be reamed out. The paths have a shallow curvature so that the cannulae do not encounter sharp bends. This reduces the friction between walls of the tetrode carrier and guide cannulae. The distribution of the cannulae/tetrodes when they exit the drive core is predefined and distributed in close packed formation. This distribution can be customized for use in different brain regions. The process of gluing the guide cannulae to the drive body is much simpler, with dedicated glue wells that are easy to

fill at the drive tip and improvements in the center dental acrylic fill to help it grab onto the drive body better. The amount of dental acrylic needed is also significantly reduced, cutting down on the overall weight. A combined drive body also helps with an issue where a bad seal between the drive core and the bottom bundle could cause dental acrylic to leak and flow around the 0-80 nuts jamming them up. This is now almost impossible in the new design. Dedicated glue wells has been added for support posts with the gluing at the bottom of the drive being a single fill to glue in all support posts. This cuts down on time needed as well as keeps the glue away from the 0-80 washers and nuts. Dedicated pathways has been added for routing ground wire that are now removed from the central dental acrylic fill well to allow better guidance of ground wire as well as repair/replacement if needed. Use of 29 gauge Extra Thin Wall (XTW) cannulae to add enough tolerance for manufacturer variability helps reduce tetrode guide cannulae to carrier cannulae friction consequently also reducing backlash. All screw holes are printed pre-threaded. The 0-80 shuttle shuttle screw holes have been enlarged to make the process of reaming them easier. The drive core has been designed not just with the required functionality of a hyperdrive in mind but also includes design decisions to compensate for the foibles of the 3D printer used to print this, reducing the variability of quality from print to print.

External contributions: Francesco Savelli and JD Luck developed the original drive design on which the following design was based on. I received

general feedback on design changes from members of the Knierim Lab especially Francesco Savelli, Manu S Madhav, Vyash Puliyadi. In addition Francesco helped in understanding the thought behind the design of the endodrive. Manu built a drive using this design and gave feedback which was incorporated in subsequent versions. Vyash Puliyadi contributed design ideas for making the drive print more reliably on the Form2 printer.

Bibliography

- Nelson, M. E. (2011). "Electric fish". In: *Current Biology* 21.14, R528–R529.
- Hopkins, C. D. (1974). "Electric communication: functions in the social behavior of *Eigenmannia virescens*". In: *Behaviour* 50.3-4, pp. 270–304.
- Stamper, S. A., M. S. Madhav, N. J. Cowan, and E. S. Fortune (2012). "Beyond the Jamming Avoidance Response: weakly electric fish respond to the envelope of social electrosensory signals". In: *Journal of Experimental Biology* 215.23, pp. 4196–4207.
- Bullock, T. H., R. H. Hamstra, and H. Scheich (1972). "The jamming avoidance response of high frequency electric fish". In: *How do Brains Work?* Springer, pp. 509–534.
- Robie, A. A., K. M. Seagraves, S. R. Egnor, and K. Branson (2017). "Machine vision methods for analyzing social interactions". In: *J Exp Biol* 220.1, pp. 25–34.
- Egnor, S. R. and K. Branson (2016). "Computational Analysis of Behavior". In: *Annu Rev Neurosci* 39, pp. 217–236.
- Tan, E. W., J. M. Nizar, E. Carrera-G, and E. S. Fortune (2005a). "Electrosensory interference in naturally occurring aggregates of a species of weakly electric fish, *Eigenmannia virescens*". In: *Behavioural brain research* 164.1, pp. 83–92.
- Thomas, M., A. Floion, and D. Chretien (1998). "A new warning biomonitor using a weakly electric fish, *Apteronotus albifrons* (Gymnotiformes), and the effect of temperature on the bioelectric responses". In: *Environ Monit Assess* 51.3, pp. 605–620.
- Geller, W. (1984). "A toxicity warning monitor using the weakly electric fish, *Gnathonemus petersi*". In: *Water Res* 18.10, pp. 1285–1290.
- Richards, P. (1974). "Kant's Geography and Mental Maps". In: *Transactions of the Institute of British Geographers* 61, pp. 1–16. ISSN: 00202754, 14755661.
- Tolman, E. C. (1948). "Cognitive maps in rats and men." In: *Psychological review* 55.4, p. 189.

- O'Keefe, J. and L. Nadel (1978). *The Hippocampus as a Cognitive Map*. Oxford University Press. ISBN: 0198572069.
- Taube, J. S., R. U. Muller, and J. Ranck Jr (1990). "Head-direction cells recorded from the postsubiculum in freely moving rats. I. Description and quantitative analysis." eng. In: *J Neurosci* 10.2, pp. 420–435.
- Hafting, T., M. Fyhn, S. Molden, M.-B. Moser, and E. I. Moser (2005). "Microstructure of a spatial map in the entorhinal cortex." eng. In: *Nature* 436.7052, pp. 801–806.
- Manns, J. R., M. W. Howard, and H. Eichenbaum (2007). "Gradual changes in hippocampal activity support remembering the order of events". In: *Neuron* 56.3, pp. 530–540.
- Keene, C. S., J. Bladon, S. McKenzie, C. D. Liu, J. O'Keefe, and H. Eichenbaum (2016). "Complementary functional organization of neuronal activity patterns in the perirhinal, lateral entorhinal, and medial entorhinal cortices". In: *Journal of Neuroscience* 36.13, pp. 3660–3675.
- Lisman, J. E. (2007). "Role of the dual entorhinal inputs to hippocampus: a hypothesis based on cue/action (non-self/self) couplets". In: *Progress in brain research* 163, pp. 615–818.
- Knierim, J. J., J. P. Neunuebel, and S. S. Deshmukh (2014). "Functional correlates of the lateral and medial entorhinal cortex: objects, path integration and local–global reference frames". In: *Philosophical Transactions of the Royal Society B: Biological Sciences* 369.1635, p. 20130369.
- Furtak, S. C., O. J. Ahmed, and R. D. Burwell (2012). "Single neuron activity and theta modulation in postrhinal cortex during visual object discrimination". In: *Neuron* 76.5, pp. 976–988.
- Sereno, A. B. and S. R. Lehky (2011). "Population coding of visual space: comparison of spatial representations in dorsal and ventral pathways". In: *Frontiers in computational neuroscience* 4, p. 159.
- Connor, C. E. and J. J. Knierim (2017). "Integration of objects and space in perception and memory". In: *Nature neuroscience* 20.11, p. 1493.
- Manns, J. R. and H. Eichenbaum (2006). "Evolution of declarative memory." eng. In: *Hippocampus* 16.9, pp. 795–808.
- Davachi, L., J. P. Mitchell, and A. D. Wagner (2003). "Multiple routes to memory: distinct medial temporal lobe processes build item and source memories." eng. In: *Proc Natl Acad Sci U S A* 100.4, pp. 2157–2162.
- Suzuki, W. A., E. K. Miller, and R. Desimone (1997). "Object and place memory in the macaque entorhinal cortex." eng. In: *J Neurophysiol* 78.2, pp. 1062–1081.

- Knierim, J. J., I. Lee, and E. L. Hargreaves (2006). "Hippocampal place cells: parallel input streams, subregional processing, and implications for episodic memory." eng. In: *Hippocampus* 16.9, pp. 755–764.
- Eichenbaum, H., A. P. Yonelinas, and C. Ranganath (2007). "The medial temporal lobe and recognition memory." eng. In: *Annu Rev Neurosci* 30, pp. 123–152.
- Knierim, J. J., H. S. Kudrimoti, and B. L. McNaughton (1998a). "Interactions between idiothetic cues and external landmarks in the control of place cells and head direction cells." eng. In: *J Neurophysiol* 80.1, pp. 425–446.
- Hargreaves, E. L., D. Yoganarasimha, and J. J. Knierim (2007). "Cohesiveness of spatial and directional representations recorded from neural ensembles in the anterior thalamus, parasubiculum, medial entorhinal cortex, and hippocampus." eng. In: *Hippocampus* 17.9, pp. 826–841.
- Save, E., A. Cressant, C. Thinus-Blanc, and B. Poucet (1998). "Spatial firing of hippocampal place cells in blind rats." eng. In: *J Neurosci* 18.5, pp. 1818–1826.
- Stackman, R. W., A. S. Clark, and J. S. Taube (2002). "Hippocampal spatial representations require vestibular input." eng. In: *Hippocampus* 12.3, pp. 291–303.
- Sargolini, F., M. Fyhn, T. Hafting, B. L. McNaughton, M. P. Witter, M.-B. Moser, and E. I. Moser (2006). "Conjunctive representation of position, direction, and velocity in entorhinal cortex." eng. In: *Science* 312.5774, pp. 758–762.
- Vanderwolf, C. H. (1969). "Hippocampal electrical activity and voluntary movement in the rat." eng. In: *Electroencephalogr Clin Neurophysiol* 26.4, pp. 407–418.
- McNaughton, B. L., C. A. Barnes, and J. O'Keefe (1983). "The contributions of position, direction, and velocity to single unit activity in the hippocampus of freely-moving rats." eng. In: *Exp Brain Res* 52.1, pp. 41–49.
- McNaughton, B. L., C. A. Barnes, J. L. Gerrard, K. Gothard, M. W. Jung, J. J. Knierim, H. Kudrimoti, Y. Qin, W. E. Skaggs, M. Suster, and K. L. Weaver (1996). "Deciphering the hippocampal polyglot: the hippocampus as a path integration system." eng. In: *J Exp Biol* 199.Pt 1, pp. 173–185.
- Stackman, R. W. and J. S. Taube (1997). "Firing properties of head direction cells in the rat anterior thalamic nucleus: dependence on vestibular input". In: 17.11, pp. 4349–4358.
- Kropff, E., J. E. Carmichael, M.-B. Moser, and E. I. Moser (2015a). "Speed cells in the medial entorhinal cortex". In: *Nature* 523.7561, pp. 419–424. ISSN: 0028-0836.

- O'Keefe, J. and L. Nadel (1978). *The hippocampus as a cognitive map*. Oxford, United Kingdom: Clarendon Press,
- Muller, R. U. and J. L. Kubie (1987). "The effects of changes in the environment on the spatial firing of hippocampal complex-spike cells." eng. In: *J Neurosci* 7.7, pp. 1951–1968.
- Knierim, J. J. (2002). "Dynamic interactions between local surface cues, distal landmarks, and intrinsic circuitry in hippocampal place cells." eng. In: *J Neurosci* 22.14, pp. 6254–6264.
- Knierim, J. J. and D. A. Hamilton (2011). "Framing spatial cognition: neural representations of proximal and distal frames of reference and their roles in navigation." eng. In: *Physiol Rev* 91.4, pp. 1245–1279.
- O'Keefe, J. and N. Burgess (1996). "Geometric determinants of the place fields of hippocampal neurons." eng. In: *Nature* 381.6581, pp. 425–428.
- Barry, C., R. Hayman, N. Burgess, and K. J. Jeffery (2007). "Experience-dependent rescaling of entorhinal grids". In: 10.6, pp. 682–684.
- Krupic, J., M. Bauza, S. Burton, C. Barry, and J. O'Keefe (2015). "Grid cell symmetry is shaped by environmental geometry". In: *Nature* 518.7538, pp. 232–235.
- Hardcastle, K., S. Ganguli, and L. M. Giocomo (2015a). "Environmental Boundaries as an Error Correction Mechanism for Grid Cells". In: *Neuron* 86.3, pp. 827–839. ISSN: 0896-6273.
- Savelli, F., D. Yoganarasimha, and J. J. Knierim (2008). "Influence of boundary removal on the spatial representations of the medial entorhinal cortex". In: *Hippocampus* 18.12, pp. 1270–1282.
- Solstad, T., C. N. Boccara, E. Kropff, M. B. Moser, and E. I. Moser (2008). "Representation of geometric borders in the entorhinal cortex". In: *Science* 322.5909, pp. 1865–1868.
- Lever, C., S. Burton, A. Jeewajee, J. O'Keefe, and N. Burgess (2009). "Boundary vector cells in the subiculum of the hippocampal formation". In: 29.31, pp. 9771–9777.
- Deshmukh, S. S. and J. J. Knierim (2013). "Influence of local objects on hippocampal representations: Landmark vectors and memory". In: *Hippocampus* 23.4, pp. 253–267.
- Ravassard, P., A. Kees, B. Willers, D. Ho, D. Aharoni, J. Cushman, Z. M. Aghajan, and M. R. Mehta (2013a). "Multisensory Control of Hippocampal Spatiotemporal Selectivity". In: *Science* 340.6138, pp. 1342–1346. ISSN: 0036-8075.

- Saleem, A. B., A. Ayaz, K. J. Jeffery, K. D. Harris, and M. Carandini (2013). "Integration of visual motion and locomotion in mouse visual cortex." eng. In: *Nat Neurosci* 16.12, pp. 1864–1869.
- Aronov, D. and D. W. Tank (2014). "Engagement of neural circuits underlying 2D spatial navigation in a rodent virtual reality system." eng. In: *Neuron* 84.2, pp. 442–456.
- Aghajan, Z. M., L. Acharya, J. J. Moore, J. D. Cushman, C. Vuong, and M. R. Mehta (2015). "Impaired spatial selectivity and intact phase precession in two-dimensional virtual reality." eng. In: *Nat Neurosci* 18.1, pp. 121–128.
- Chen, G., J. A. King, N. Burgess, and J. O'Keefe (2013). "How vision and movement combine in the hippocampal place code." eng. In: *Proc Natl Acad Sci U S A* 110.1, pp. 378–383.
- Terrazas, A., M. Krause, P. Lipa, K. M. Gothard, C. A. Barnes, and B. L. McNaughton (2005a). "Self-motion and the hippocampal spatial metric." eng. In: *J Neurosci* 25.35, pp. 8085–8096.
- Madhav, M. S., R. P. Jayakumar, A. Demir, S. A. Stamper, E. S. Fortune, and N. J. Cowan (2018). "High-resolution behavioral mapping of electric fishes in Amazonian habitats". In: *Scientific reports* 8.1, p. 5830.
- Fortune, E., N. Andanar, M. Madhav, R. Jayakumar, N. J. Cowan, M. E. Bichuette, and D. Soares (2019). "Spooky interaction at a distance in cave and surface dwelling electric fishes". In: *bioRxiv*, p. 747154.
- Cheng, B., X. Deng, and T. L. Hedrick (2011). "The mechanics and control of pitching manoeuvres in a freely flying hawkmoth (*Manduca sexta*)". In: *Journal of Experimental Biology* 214.24, pp. 4092–4106. ISSN: 0022-0949.
- Noldus, L. P. J. J., A. J. Spink, and R. A. J. Tegelenbosch (2001). "EthoVision: A versatile video tracking system for automation of behavioral experiments". In: *Behavior Research Methods, Instruments, & Computers* 33.3, pp. 398–414. ISSN: 1532-5970.
- Chaumont, F. de, R. D.-S. Coura, P. Serreau, A. Cressant, J. Chabout, S. Grannon, and J.-C. Olivo-Marin (2012). "Computerized video analysis of social interactions in mice". In: *Nature methods* 9.4, pp. 410–417.
- Kohlhoff, K. J., T. R. Jahn, D. A. Lomas, C. M. Dobson, D. C. Crowther, and M. Vendruscolo (2011). "The iFly tracking system for an automated locomotor and behavioural analysis of *Drosophila melanogaster*". In: *Integrative Biology* 3.7, pp. 755–760.
- Branson, K., A. A. Robie, J. Bender, P. Perona, and M. H. Dickinson (2009). "High-throughput ethomics in large groups of *Drosophila*". In: *Nature methods* 6.6, pp. 451–457.

- Dankert, H., L. Wang, E. D. Hoopfer, D. J. Anderson, and P. Perona (2009). "Automated monitoring and analysis of social behavior in *Drosophila*". In: *Nature methods* 6.4, pp. 297–303.
- Fontaine, E. I., F. Zabala, M. H. Dickinson, and J. W. Burdick (2009). "Wing and body motion during flight initiation in *Drosophila* revealed by automated visual tracking". In: *Journal of Experimental Biology* 212.9, pp. 1307–1323.
- Gomez-Marin, A., N. Partoune, G. J. Stephens, and M. Louis (2012). "Automated tracking of animal posture and movement during exploration and sensory orientation behaviors". In: *PloS one* 7.8, e41642.
- Kabra, M., A. A. Robie, M. Rivera-Alba, S. Branson, and K. Branson (2013). "JAABA: interactive machine learning for automatic annotation of animal behavior". In: *nature methods* 10.1, pp. 64–67.
- Pérez-Escudero, A., J. Vicente-Page, R. C. Hinz, S. Arganda, and G. G. de Polavieja (2014). "idTracker: tracking individuals in a group by automatic identification of unmarked animals". In: *Nature methods* 11.7, pp. 743–748.
- Weimerskirch, H., F. Bonadonna, F. Bailleul, G. Mabile, G. Dell’Omo, and H.-P. Lipp (2002). "GPS Tracking of Foraging Albatrosses". In: *Science* 295.5558, pp. 1259–1259. ISSN: 0036-8075.
- Tsoar, A., R. Nathan, Y. Bartan, A. Vysotski, G. Dell’Omo, and N. Ulanovsky (2011). "Large-scale navigational map in a mammal". In: *Proceedings of the National Academy of Sciences* 108.37, E718–E724.
- Tomkiewicz, S. M., M. R. Fuller, J. G. Kie, and K. K. Bates (2010). "Global positioning system and associated technologies in animal behaviour and ecological research". In: *Philosophical Transactions of the Royal Society B: Biological Sciences* 365.1550, pp. 2163–2176. ISSN: 0962-8436.
- Ghose, K., D. Zotkin, R. Duraiswami, and C. F. Moss (2001). "Multimodal localization of a flying bat". In: *Acoustics, Speech, and Signal Processing, 2001. Proceedings. (ICASSP '01). 2001 IEEE International Conference on*. Vol. 5, 3057–3060 vol.5.
- Blumstein, D. T., D. J. Mennill, P. Clemens, L. Girod, K. Yao, G. Patricelli, J. L. Deppe, A. H. Krakauer, C. Clark, K. A. Cortopassi, S. F. Hanser, B. McCowan, A. M. Ali, and A. N. G. Kirschel (2011). "Acoustic monitoring in terrestrial environments using microphone arrays: applications, technological considerations and prospectus". In: *Journal of Applied Ecology* 48.3, pp. 758–767. ISSN: 1365-2664.
- Ali, A. M., S. Asgari, T. C. Collier, M. Allen, L. Girod, R. E. Hudson, K. Yao, C. E. Taylor, and D. T. Blumstein (2009). "An Empirical Study of Collaborative

- Acoustic Source Localization". In: *Journal of Signal Processing Systems* 57.3, pp. 415–436. ISSN: 1939-8115.
- Giraudet, P. and H. Glotin (2006). "Real-time 3D tracking of whales by echo-robust precise TDOA estimates with a widely-spaced hydrophone array". In: *Applied Acoustics* 67.11–12, pp. 1106–1117. ISSN: 0003-682X.
- Watkins, W. A. and W. E. Schevill (1972). "Sound source location by arrival-times on a non-rigid three-dimensional hydrophone array". In: *Deep Sea Research and Oceanographic Abstracts* 19.10, pp. 691–706. ISSN: 0011-7471.
- Heiligenberg (1991). *Neural nets in electric fish*. Cambridge, MA: MIT Press.
- Fortune, E. S. (2006). "The decoding of electrosensory systems." In: *Curr Opin Neurobiol* 16.4, pp. 474–480.
- Middleton, J., E. Harvey-Girard, L. Maler, and a. Longtin (2007). "Envelope gating and noise shaping in populations of noisy neurons". In: 75.2, p. 021918. ISSN: 1539-3755.
- Chacron, M. J., B. Doiron, L. Maler, A. Longtin, and J. Bastian (2003). "Non-classical receptive field mediates switch in a sensory neuron's frequency tuning". In: *Nature* 423.6935, pp. 77–81.
- Tan, E. W., J. M. Nizar, E. Carrera-G, and E. S. Fortune (2005b). "Electrosensory interference in naturally occurring aggregates of a species of weakly electric fish, *Eigenmannia virescens*." In: *Behav Brain Res* 164.1, pp. 83–92.
- Hitschfeld, É., S. Stamper, K. Vonderschen, E. Fortune, and M. Chacron (2009). "Effects of restraint and immobilization on electrosensory behaviors of weakly electric fish". In: *ILAR J* 50, pp. 361–372.
- Assad, C., B. Rasnow, P. Stoddard, and J. Bower (1998). "The electric organ discharges of the gymnotiform fishes: II. *Eigenmannia*". In: *Journal of Comparative Physiology A* 183.4, pp. 419–432.
- Assad, C., B. Rasnow, and P. K. Stoddard (1999). "Electric organ discharges and electric images during electrolocation." In: *J Exp Biol* 202.Pt 10, pp. 1185–1193.
- Kuhn, H. W. (1955). "The Hungarian method for the assignment problem". In: *Nav Res Logist Q* 2.1-2, pp. 83–97.
- Arulampalam, M. S., S. Maskell, N. Gordon, and T. Clapp (2002). "A tutorial on particle filters for online nonlinear/non-Gaussian Bayesian tracking". In: *IEEE Transactions on signal processing* 50.2, pp. 174–188.
- Bichuette, M. E. and E. Trajano (2015). "Population density and habitat of an endangered cave fish *Eigenmannia vicentespelaea* Triques, 1996 (Ostariophysi: Gymnotiformes) from a karst area in central Brazil". In: *Neotrop Ichthyol* 13.1, pp. 113–122.

- Snyder, J., Y. Silverman, Y. Bai, and M. A. MacIver (2012). "Underwater object tracking using electrical impedance tomography". In: *2012 IEEE/RSJ International Conference on Intelligent Robots and Systems*, pp. 520–525.
- Boyer, F., P. B. Gossiaux, B. Jawad, V. Lebastard, and M. Porez (2012). "Model for a sensor inspired by electric fish". In: *IEEE Trans Robot* 28.2, pp. 492–505.
- Jun, J. J., A. Longtin, and L. Maler (2013). "Real-Time Localization of Moving Dipole Sources for Tracking Multiple Free-Swimming Weakly Electric Fish". In: *PLoS ONE* 8.6. Ed. by Y. Wang, e66596. ISSN: 1932-6203.
- Stamper, S., E. Carrera-G, E. Tan, and E. Fortune (2010). "Species differences in group size and electrosensory interference in weakly electric fishes: implications for electrosensory processing". In: *Behav Brain Res* 207.2, pp. 368–376.
- Oestreich, J. and H. H. Zakon (2005). "Species-specific differences in sensorimotor adaptation are correlated with differences in social structure". In: *Journal of Comparative Physiology A* 191.9, pp. 845–856. ISSN: 1432-1351.
- Henninger, J., F. Kirschbaum, J. Grewe, R. Krahe, and J. Benda (2017). "Sensory tuning does not match behavioral relevance of communication signals in free-living weakly electric fish". In: *bioRxiv*.
- Hupé, G. and J. Lewis (2008). "Electrocommunication signals in free swimming brown ghost knifefish, *Apteronotus leptorhynchus*". In: *J Exp Biol* 211.10, pp. 1657–1667.
- Jayakumar, R. P., M. S. Madhav, F. Savelli, H. T. Blair, N. J. Cowan, and J. J. Knierim (2019). "Recalibration of path integration in hippocampal place cells". In: *Nature* 566.7745, p. 533.
- Acharya, L., Z. M. Aghajan, C. Vuong, J. J. Moore, and M. R. Mehta (2016). "Causal Influence of Visual Cues on Hippocampal Directional Selectivity". In: *Cell* 164.1, pp. 197–207. ISSN: 0092-8674.
- Chen, G., J. A. King, N. Burgess, and J. O'Keefe (2013). "How vision and movement combine in the hippocampal place code". In: *Proceedings of the National Academy of Sciences* 110.1, pp. 378–383. ISSN: 0027-8424.
- Etienne, A. S. and K. J. Jeffery (2004). "Path integration in mammals". In: *Hippocampus* 14.2, pp. 180–192.
- Wehner, R. and R. Menzel (1990). "Do Insects Have Cognitive Maps?" In: *Annual Review of Neuroscience* 13.1, pp. 403–414.
- Wittlinger, M., R. Wehner, and H. Wolf (2006). "The Ant Odometer: Stepping on Stilts and Stumps". In: *Science* 312.5782, pp. 1965–1967. ISSN: 0036-8075.
- Mittelstaedt, M. -.L. and H. Mittelstaedt (1980). "Homing by path integration in a mammal". In: *Naturwissenschaften* 67.11, pp. 566–567. ISSN: 1432-1904.

- Gallistel, C. R. (1990). *The organization of learning*. ISBN: 9780262570985.
- Samsonovich, A. and B. L. McNaughton (1997). "Path Integration and Cognitive Mapping in a Continuous Attractor Neural Network Model". In: *Journal of Neuroscience* 17.15, pp. 5900–5920. ISSN: 0270-6474.
- Fuhs, M. C. and D. S. Touretzky (2006). "A Spin Glass Model of Path Integration in Rat Medial Entorhinal Cortex". In: *Journal of Neuroscience* 26.16, pp. 4266–4276. ISSN: 0270-6474.
- McNaughton, B. L., F. P. Battaglia, O. Jensen, E. I. Moser, and M. B. Moser (2006). "Path integration and the neural basis of the cognitive map". In: *Nat Rev Neurosci* 7.8, pp. 663–78. ISSN: 1471-003X (Print).
- Hasselmo, M. E., L. M. Giocomo, and E. A. Zilli (2007). "Grid cell firing may arise from interference of theta frequency membrane potential oscillations in single neurons". In: *Hippocampus* 17.12, pp. 1252–1271.
- Blair, H. T., K. Gupta, and K. Zhang (2008). "Conversion of a phase- to a rate-coded position signal by a three-stage model of theta cells, grid cells, and place cells". In: *Hippocampus* 18.12, pp. 1239–1255.
- Burgess, N., C. Barry, and J. O'Keefe (2007). "An oscillatory interference model of grid cell firing". In: *Hippocampus* 17.9, pp. 801–812.
- Tcheang, L., H. H. Bulthoff, and N. Burgess (2011a). "Visual influence on path integration in darkness indicates a multimodal representation of large-scale space". In: *Proceedings of the National Academy of Sciences* 108.3, pp. 1152–1157. ISSN: 0027-8424.
- Knierim, J. J., H. S. Kudrimoti, and B. L. McNaughton (1998b). "Interactions Between Idiothetic Cues and External Landmarks in the Control of Place Cells and Head Direction Cells". In: *Journal of Neurophysiology* 80.1, pp. 425–446.
- Zugaro, M. B., A. Arleo, A. Berthoz, and S. I. Wiener (2003). "Rapid Spatial Reorientation and Head Direction Cells". In: *Journal of Neuroscience* 23.8, pp. 3478–3482. ISSN: 0270-6474.
- Hardcastle, K., S. Ganguli, and L. M. Giocomo (2015b). "Environmental Boundaries as an Error Correction Mechanism for Grid Cells". In: *Neuron* 86.3, pp. 827–839. ISSN: 0896-6273.
- Etienne, A. S., R. Maurer, and V. Séguinot (1996). "Path integration in mammals and its interaction with visual landmarks." In: *Journal of Experimental Biology* 199.1, pp. 201–209. ISSN: 0022-0949.
- Moser, E. I., M.-B. Moser, and B. L. McNaughton (2017). "Spatial representation in the hippocampal formation: a history". In: *Nature Neuroscience* 20.11, pp. 1448–1464. ISSN: 1097-6256.

- Gil, M., M. Ancau, M. I. Schlesiger, A. Neitz, K. Allen, R. J. De Marco, and H. Monyer (2018). "Impaired path integration in mice with disrupted grid cell firing". In: *Nature Neuroscience* 21.1, p. 8193. ISSN: 15461726.
- Tennant, S. A., L. Fischer, D. L. Garden, K. Z. Gerlei, C. Martinez-Gonzalez, C. McClure, E. R. Wood, and M. F. Nolan (2018). "Stellate Cells in the Medial Entorhinal Cortex Are Required for Spatial Learning". In: *Cell Reports* 22.5, pp. 1313–1324. ISSN: 2211-1247.
- Hölscher, C., A. Schnee, H. Dahmen, L. Setia, and H. A. Mallot (2005). "Rats are able to navigate in virtual environments". In: *Journal of Experimental Biology* 208.3, pp. 561–569. ISSN: 0022-0949.
- Harvey, C. D., F. Collman, D. A. Dombeck, and D. W. Tank (2009). "Intracellular dynamics of hippocampal place cells during virtual navigation". In: *Nature* 461.7266, p. 941946. ISSN: 00280836.
- Ravassard, P., A. Kees, B. Willers, D. Ho, D. Aharoni, J. Cushman, Z. M. Aghajan, and M. R. Mehta (2013b). "Multisensory Control of Hippocampal Spatiotemporal Selectivity". In: *Science* 340.6138, pp. 1342–1346. ISSN: 0036-8075.
- Quigley, M., K. Conley, B. Gerkey, J. Faust, T. Foote, J. Leibs, E. Berger, R. Wheeler, and A. Mg (2009). "ROS: an open-source Robot Operating System". In: *Icra* 3. Figure 1, p. 5. ISSN: 0165-022X.
- Csicsvari, J., H. Hirase, A. Czurkó, A. Mamiya, and G. Buzsáki (1999). "Oscillatory Coupling of Hippocampal Pyramidal Cells and Interneurons in the Behaving Rat". In: *Journal of Neuroscience* 19.1, pp. 274–287. ISSN: 0270-6474.
- Skaggs, W. E., B. L. McNaughton, K. M. Gothard, and E. J. Markus (1993). "An Information-Theoretic Approach to Deciphering the Hippocampal Code". In: *Proceedings of the IEEE* 1990, pp. 1030–1037. ISSN: 00189219.
- Zhang, K., I. Ginzburg, B. L. McNaughton, and T. J. Sejnowski (1998). "Interpreting Neuronal Population Activity by Reconstruction: Unified Framework With Application to Hippocampal Place Cells". In: *Journal of Neurophysiology* 79.2, pp. 1017–1044.
- Kloosterman, F., S. P. Layton, Z. Chen, and M. A. Wilson (2014). "Bayesian decoding using unsorted spikes in the rat hippocampus". In: *Journal of Neurophysiology* 111.1, pp. 217–227.
- Brown, E. N., L. M. Frank, D. Tang, M. C. Quirk, and M. A. Wilson (1998). "A Statistical Paradigm for Neural Spike Train Decoding Applied to Position Prediction from Ensemble Firing Patterns of Rat Hippocampal Place Cells". In: *Journal of Neuroscience* 18.18, pp. 7411–7425. ISSN: 0270-6474.

- Flandrin, P., A. Francois, and E. Chassande-Mottin (2002). "Time-Frequency Reassignment: From Principles to Algorithms". In: *Applications in Time-Frequency Signal Processing*, pp. 179–204. ISSN: 1053587X.
- Campbell, M. G., S. A. Ocko, C. S. Mallory, I. I. Low, S. Ganguli, and L. M. Giocomo (2018). "Principles governing the integration of landmark and self-motion cues in entorhinal cortical codes for navigation". In: *Nature Neuroscience* 21.August. ISSN: 15461726.
- Colgin, L. L., T. Denninger, M. Fyhn, T. Hafting, T. Bonnevie, O. Jensen, M.-B. Moser, and E. I. Moser (2009). "Frequency of gamma oscillations routes flow of information in the hippocampus". In: *Nature* 462.7271, p. 353.
- Kemere, C., M. F. Carr, M. P. Karlsson, and L. M. Frank (2013). "Rapid and continuous modulation of hippocampal network state during exploration of new places". In: *PloS one* 8.9, e73114.
- Zheng, C., K. W. Bieri, S. G. Trettel, and L. L. Colgin (2015). "The relationship between gamma frequency and running speed differs for slow and fast gamma rhythms in freely behaving rats". In: *Hippocampus* 25.8, pp. 924–938.
- Amemiya, S. and A. D. Redish (2018). "Hippocampal theta-gamma coupling reflects state-dependent information processing in decision making". In: *Cell reports* 22.12, pp. 3328–3338.
- Csicsvari, J., B. Jamieson, K. D. Wise, and G. Buzsáki (2003). "Mechanisms of gamma oscillations in the hippocampus of the behaving rat". In: *Neuron* 37.2, pp. 311–322.
- Huerta, P. T. and J. E. Lisman (1995). "Bidirectional synaptic plasticity induced by a single burst during cholinergic theta oscillation in CA1 in vitro". In: *Neuron* 15.5, pp. 1053–1063.
- Hasselmo, M. E., C. Bodelón, and B. P. Wyble (2002). "A proposed function for hippocampal theta rhythm: separate phases of encoding and retrieval enhance reversal of prior learning". In: *Neural computation* 14.4, pp. 793–817.
- Kitanishi, T., S. Ujita, M. Fallahnezhad, N. Kitanishi, Y. Ikegaya, and A. Tashiro (2015). "Novelty-induced phase-locked firing to slow gamma oscillations in the hippocampus: requirement of synaptic plasticity". In: *Neuron* 86.5, pp. 1265–1276.
- Bastian, A. J. (2006). "Learning to predict the future: the cerebellum adapts feedforward movement control". In: *Current Opinion in Neurobiology* 16.6, pp. 645–649. ISSN: 0959-4388.

- Miles, F. A. and S. G. Lisberger (1981). "Plasticity in the Vestibulo-Ocular Reflex: A New Hypothesis". In: *Annual Review of Neuroscience* 4.1, pp. 273–299.
- Tcheang, L., H. H. Bulthoff, and N. Burgess (2011b). "Visual influence on path integration in darkness indicates a multimodal representation of large-scale space". In: *Proceedings of the National Academy of Sciences* 108.3, pp. 1152–1157. ISSN: 0027-8424.
- Terrazas, A., M. Krause, P. Lipa, K. M. Gothard, C. A. Barnes, and B. L. McNaughton (2005b). "Self-Motion and the Hippocampal Spatial Metric". In: *Journal of Neuroscience* 25.35, pp. 8085–8096. ISSN: 0270-6474.
- Maurer, A. P., S. R. VanRhoads, G. R. Sutherland, P. Lipa, and B. L. McNaughton (2005). "Self-motion and the origin of differential spatial scaling along the septo-temporal axis of the hippocampus". In: *Hippocampus* 15.7, pp. 841–852.
- Kropff, E., J. E. Carmichael, M.-B. Moser, and E. I. Moser (2015b). "Speed cells in the medial entorhinal cortex". In: *Nature* 523.7561, pp. 419–424. ISSN: 0028-0836.
- Hinman, J. R., M. P. Brandon, J. R. Climer, G. W. Chapman, and M. E. Hasselmo (2016). "Multiple Running Speed Signals in Medial Entorhinal Cortex". In: *Neuron* 91.3, pp. 666–679. ISSN: 0896-6273.
- Mehta, M. R., C. A. Barnes, and B. L. McNaughton (1997). "Experience-dependent, asymmetric expansion of hippocampal place fields". In: *Proceedings of the National Academy of Sciences* 94.16, pp. 8918–8921.
- Sharp, P. E., H. T. Blair, D. Etkin, and D. B. Tzanetos (1995). "Influences of vestibular and visual motion information on the spatial firing patterns of hippocampal place cells". In: *Journal of Neuroscience* 15.1, pp. 173–189.
- Arleo, A., C. Déjean, P. Allegraud, M. Khamassi, M. B. Zugaro, and S. I. Wiener (2013). "Optic flow stimuli update anterodorsal thalamus head direction neuronal activity in rats". In: *Journal of Neuroscience* 33.42, pp. 16790–16795.
- Raudies, F., E. Mingolla, and M. E. Hasselmo (2012). "Modeling the influence of optic flow on grid cell firing in the absence of other cues". In: *Journal of computational neuroscience* 33.3, pp. 475–493.
- Raudies, F., J. R. Hinman, and M. E. Hasselmo (2016). "Modelling effects on grid cells of sensory input during self-motion". In: *The Journal of physiology* 594.22, pp. 6513–6526.
- Sherrill, K. R., E. R. Chrastil, R. S. Ross, U. M. Erdem, M. E. Hasselmo, and C. E. Stern (2015). "Functional connections between optic flow areas and

- navigationally responsive brain regions during goal-directed navigation". In: *Neuroimage* 118, pp. 386–396.
- Amaral, D. G. and M. P. Witter (1989). "The three-dimensional organization of the hippocampal formation: a review of anatomical data". In: *Neuroscience* 31.3, pp. 571–591.
- Muller, R. U., M. Stead, and J. Pach (1996). "The hippocampus as a cognitive graph." In: *The Journal of general physiology* 107.6, pp. 663–694.
- Isaac, J. T., K. A. Buchanan, R. U. Muller, and J. R. Mellor (2009). "Hippocampal place cell firing patterns can induce long-term synaptic plasticity in vitro". In: *Journal of Neuroscience* 29.21, pp. 6840–6850.
- Kesner, R. P. (2007). "Behavioral functions of the CA3 subregion of the hippocampus". In: *Learning & memory* 14.11, pp. 771–781.
- Rolls, E. (2013). "A quantitative theory of the functions of the hippocampal CA3 network in memory". In: *Frontiers in cellular neuroscience* 7, p. 98.
- Lee, J. W., W. R. Kim, W. Sun, and M. W. Jung (2012). "Disruption of dentate gyrus blocks effect of visual input on spatial firing of CA1 neurons". In: *Journal of Neuroscience* 32.38, pp. 12999–13003.
- Lee, J. W., W. R. Kim, W. Sun, and M. W. Jung (2009). "Role of dentate gyrus in aligning internal spatial map to external landmark". In: *Learning & Memory* 16.9, pp. 530–536.
- Yoder, R. M., B. J. Clark, and J. S. Taube (2011). "Origins of landmark encoding in the brain". In: *Trends in neurosciences* 34.11, pp. 561–571.
- Faessler, M., E. Mueggler, K. Schwabe, and D. Scaramuzza (2014). "A monocular pose estimation system based on infrared leds". In: *2014 IEEE International Conference on Robotics and Automation (ICRA)*. IEEE, pp. 907–913.
- Savkin, P. A., S. Saito, J. Vansteenberge, T. Fukusato, L. Wilson, and S. Morishima (2017). "Outside-in monocular IR camera based HMD pose estimation via geometric optimization". In: *Proceedings of the 23rd ACM Symposium on Virtual Reality Software and Technology*. ACM, p. 7.

Vitae

Ravikrishnan Perur Jayakumar, born on 24th of February 1986 in Trivandrum, India, received his Bachelor of Technology degree in Mechanical Engineering from National Institute of Technology - Calicut, India in 2008. He then did a 2 year stint at automobile manufacturing MNC, Tata Motors Ltd as an assistant manager of Manufacturing before joining the Master of Science program, with a focus in Robotics, at the Mechanical Engineering department at Johns Hopkins University in 2010 till 2012. He worked as a Research Engineer in Prof. Iulian Iordachita's Advanced Medical Instrumentation and Robotics Research Lab and Prof. Noah Cowan's Locomotion in Mechanical and Biological Systems (LIMBS) Laboratory in 2013. In the Spring 2014, he joined the Ph.D program at the Mechanical Engineering department at Johns Hopkins University and became a member of Prof. Noah Cowan's LIMBS lab from whom he received training in the mathematical methods of system identification in complex biological systems. Ravi worked on two close collaborative projects between Prof. Noah Cowan and Prof. James Knierim, a Professor in Neuroscience at Johns Hopkins University. Over the course of these projects, Prof. James Knierim was for all intents and purposes Ravi's co-advisor providing mentorship to Ravi in his training as a neuroscientist.

